UNIVERSITY OF CALIFORNIA,
IRVINE

The effects of Arctic sea-ice thickness loss and stratospheric variability on mid-latitude cold spells

DISSERTATION

submitted in partial satisfaction of the requirements
for the degree of

DOCTOR OF PHILOSOPHY

in Earth System Science

by

Zachary M. Labe

Dissertation Committee:
Professor Gudrun Magnusdottir, Chair
Chancellor's Professor Hal S. Stern
Associate Professor Michael S. Pritchard

2020

DEDICATION

Whether the weather be fine,
Or whether the weather be not,
Whether the weather be cold,
Or whether the weather be hot,
We'll weather the weather
Whatever the weather,
Whether we like it or not!
-*Anonymous*

To my parents for their unconditional support in all of my life's passions and dreams.

TABLE OF CONTENTS

LIST OF FIGURES

LIST OF TABLES

LIST OF ACRONYMS

A summary of selected acronyms used throughout the dissertation.

Acronym	Full Name
AA	Arctic amplification
(A)GCM	Atmospheric General Circulation Model
AMIP	Atmospheric Model Intercomparison Project II
CDI	cold days index
CESM	Community Earth System Model
CMIP5(6)	Coupled Model Inter-comparison Project, Phase 5 & 6
E3SM	Energy Exascale Earth System Model
EOF	empirical orthogonal function
LENS	Community Earth System Model Large Ensemble Project
MHF	meridional heat flux
NAM	Northern Annular Mode
(N)AO	North Atlantic Oscillation/Arctic Oscillation
PAMIP	Polar Amplification Model Intercomparison Project
PIOMAS	Pan-Arctic Ice Ocean Modeling and Assimilation System
PDF	probability density function
QBO	Quasi-biennial Oscillation
RCP	Representative Concentration Pathway
RNET	net surface energy flux
SHI	Siberian High Index
SIC	sea-ice concentration
SIE	sea-ice extent
SIT	sea-ice thickness
SIV	sea-ice volume
SLP	sea level pressure
SST	sea surface temperature
SSW	sudden stratospheric warming
T	temperature
U	zonal wind
WACCM	Whole Atmosphere Community Climate Model
WAF	wave activity flux
Z	geopotential height

ACKNOWLEDGMENTS

First and foremost, I would like to thank my advisor, Professor Gudrun Magnusdottir, for her unwavering support of my growth as a scientist and as a person. I am eternally grateful for her guidance, mentorship, and enthusiasm in better understanding the complexities of the climate system. Her encouragement allowed me to pursue my interests in improving accessibility in science communication and outreach. I am thankful for all of these opportunities.

I would like to thank my dissertation committee members, Professor Mike Pritchard and Professor Hal Stern, and my advancement committee members, Professor Francois Primeau and Professor Jin-Yi Yu, for their advice and input on my research projects over the last five years. I would like to thank Professor Padhraic Smyth for his support during my time in UCI's Data Science Initiative program. And thank you to Professor Julie Ferguson for her mentoring and inspiration to countless generations of students at UCI.

I would also like to thank Professor Toby Ault and Professor Mark Wysocki for their advice, friendship, and dedication to a lifetime of learning; I am forever thankful for my experiences at Cornell University.

This PhD would not have been possible without the support of my brilliant friends and colleagues within the Department of Earth System Science. I have learned more about the intricacies of our planet than I ever thought possible; it has been an amazing five years. Thank you to the past and present Magnusdottir Research Group members, Dillon Elsbury, Tien-Yiao Hsu, Dr. Yuna Lim, Dr. Ashley Payne, Ana Cláudia Thomé Sena, Dr. Graham Simpkins, Dr. Wenchang Yang, for their continued support and patience. I also owe a big thank you to Dr. Yannick Peings for his extensive knowledge on climate modeling. A special thanks to the department administrative staff for holding together this daunting PhD process and answering all of my questions.

Most of all, I would like to thank my parents, Mike and Kami Labe, for their unconditional love and push for me to achieve my highest of goals and dreams. I would not be here without those summertime workbooks, late-night weather journaling, endless repairs of my backyard weather station, and the science kits from The Learning Source. I owe many thanks to my loving grandparents, Russ and Elaine King, for riding in the backseat of aimless drives around Pennsylvania that helped to spark my interest in understanding all of the curiosities of the physical world. Thank you to my grandparents, Ron and Carole Labe, for their love and continuous support.

I am grateful for the opportunity to have participated in the International Partnerships for Excellence in Education and Research (INTPART) project: "Arctic Field Summer Schools: Norway-Canada-USA collaboration" (NFR project 261786/H30). I have a new appreciation for all of the people who make science possible at the top of the world. A special thanks to the captain and crew of the R/V *Lance*, which was chartered from 18-24 May 2017 out

of Longyearbyen, Svalbard. I will always remember the moment I saw my first glimpse of Arctic sea ice.

Funding for this research was partially provided by a National Science Foundation Research Traineeship graduate fellowship (NRT-DESE 1633631) and a Data Science Initiative Fellowship in UCI's Department of Statistics. Additional funding for this work was provided by the Department of Energy (DE-SC0019407), National Oceanic and Atmospheric Administration (NA15OAR4310164), National Science Foundation (AGS-1407360, AGS-1624038), and the Department of Earth System Science at the University of California, Irvine. Lastly, I would like to acknowledge high-performance computing support from Cheyenne (doi:10.5065/D6RX99HX) and Yellowstone (ark:/85065/d7wd3xhc) provided by NCAR's Computational and Information Systems Laboratory (CISL), sponsored by the National Science Foundation. Additional computing resources were provided by the National Energy Research Scientific Computing Center (NERSC), sponsored by the Department of Energy.

Lastly, I would like to thank the American Meteorological Society for their permission to include work published in Chapter 2 and the American Geophysical Union for their permission to include work published in Chapters 3, 4, and 5.

VITA

Zachary M. Labe

EDUCATION

Ph.D. in Earth System Science — **June 2020**
University of California, Irvine — *Irvine, CA*

M.Sc. in Earth System Science — **September 2017**
University of California, Irvine — *Irvine, CA*

B.Sc. in Atmospheric Science — **May 2015**
Cornell University, *Distinction in Research* — *Ithaca, NY*
Thesis: Anomalously Early Onset of Spring in the CESM Large
Minor: Dyson Business Minor for Life Sciences

SCIENTIFIC RESEARCH EXPERIENCE

• large-scale climate dynamics • climate variability • sea ice • stratospheric dynamics • atmospheric teleconnections • extreme events • science communication • data visualization

2015-2020 **Graduate Research Assistant**
Assessing influences of Arctic amplification and sea ice variability on the stratosphere and extreme weather in the mid-latitudes through global climate model experiments and historical observations
Advisor: Dr. Gudrun Magnusdottir, Earth System Science,
University of California Irvine

Su. 2015 **Research Assistant**
Evaluated the magnitude, frequency, and dynamics of spring onset in the CESM Large Ensemble Project (LENS) through the implementation of the Extended Spring Indices Model
Advisor: Dr. Toby Ault, Earth and Atmospheric Science,
Cornell University

2014-2015 **Undergraduate Research Assistant**
Analyzed Extended Spring Indices model forced by Berkley Earth System Temperature (BEST) reanalysis to understand early spring onset
Advisor: Dr. Toby Ault, Earth and Atmospheric Science,
Cornell University

PUBLICATIONS

Refereed/Peer-Reviewed

[7] **Labe, Z.M.**, Y. Peings, and G. Magnusdottir (2020), Warm Arctic, cold Siberia pattern: role of full Arctic amplification versus sea-ice loss alone, (*in review*)

[6] Timmermans, M.-L., **Z.M. Labe**, and C. Ladd (2020), [The Arctic] Sea surface temperature [in "State of the Climate in 2019"]. Bull. Amer. Meteor. Soc. (*in review*)

[5] Thoman, R.L., U. Bhatt, P. Bieniek, B. Brettschneider, M. Brubaker, S. Danielson, **Z.M. Labe**, R. Lader, W. Meier, G. Sheffield, and J. Walsh (2020), The record low Bering Sea ice extent in 2018: Context, impacts and an assessment of the role of anthropogenic climate change [in "Explaining Extreme Events of 2018 from a Climate Perspective"]. Bull. Amer. Meteor. Soc., DOI:10.1175/BAMS-D-19-0175.1

[4] **Labe, Z.M.**, Y. Peings, and G. Magnusdottir (2019), The effect of QBO phase on the atmospheric response to projected Arctic sea ice loss in early winter, Geophysical Research Letters, DOI:10.1029/2019GL083095.

[3] **Labe, Z.M.**, Y. Peings, and G. Magnusdottir (2018), Contributions of ice thickness to the atmospheric response from projected Arctic sea ice loss, Geophysical Research Letters, DOI:10.1029/2018GL078158.

[2] **Labe, Z.M.**, G. Magnusdottir, and H.S. Stern (2018), Variability of Arctic sea ice thickness using PIOMAS and the CESM Large Ensemble, Journal of Climate, DOI:10.1175/JCLI-D-17-0436.1.

[1] **Labe, Z.M.**, T.R. Ault, and R. Zurita-Milla (2016), Identifying Anomalously Early Spring Onsets in the CESM Large Ensemble Project, Climate Dynamics, DOI:10.10 07/s00382-016-3313-2.

Non-refereed/Other

[2] **Labe, Z.M.**, November 2019: Understanding Our Changing Arctic. Polar Bears International. Annual Magazine.

[1] **Labe, Z.M.**, April 2015: Anomalously Early Onset of Spring in the CESM Large Ensemble. Cornell University. Undergraduate Honors Thesis.

FELLOWSHIPS & AWARDS

Sep. 2019	Kavli Fellow, National Academy of Sciences
Jan. 2019	Outstanding Student Presentation Award - AMS Conference on Middle Atmosphere
Nov. 2018	Travel Award - AMS Conference on Middle Atmosphere
2016-2018	NSF NRT-DESE in Data Science and Physical Science Fellowship
Su. 2016	Data Science Initiative Fellowship, Department of Statistics, University of California, Irvine
Wi. 2016	Jenkins Family Graduate Fellowship in Earth System Science, Department of Earth System Science, University of California, Irvine

ORAL PRESENTATIONS

[**13**] **Labe, Z.M.** Observations and climate model projections of Arctic climate change. Geography Department, Irvine Valley College, CA (May 2020). (**Invited-Remote**)
[**12**] **Labe, Z.M.**,Y. Peings, and G. Magnusdottir. Detection of Signal in the Large-Scale Circulation Response to Arctic Sea-Ice Decline. *33rd Conference on Climate Variability and Change*, Boston, MA (Jan 2020).
[**11**] Magnusdottir, G., Y. Peings, and **Z.M. Labe**. Response to sea-ice loss under the Polar Amplification MIP protocol in extended ensembles of simulations. *2019 American Geophysical Union Annual Meeting*, San Francisco, CA (Dec 2019).
[**10**] **Labe, Z.M.** Melting Ice: Context, Causes, and Consequences of Polar Amplification. *Kavli Frontiers of Science, National Academy of Science*, Jerusalem, Israel (Sep 2019). (**Invited**)
[**9**] **Labe, Z.M.** Projections of a future Arctic climate. Geography Department, Irvine Valley College, CA (May 2019). (**Invited**)
[**8**] **Labe, Z.M.**, G. Magnusdottir, and Y. Peings. Linking the Quasi-Biennial Oscillation and projected Arctic sea-ice loss to stratospheric variability in early winter.
20th Conference on Middle Atmosphere, Phoenix, AZ (Jan 2019).
[**7**] Magnusdottir, G., **Z.M. Labe**, and Y. Peings. The role of the stratosphere, including the QBO, in Arctic to mid-latitude teleconnections associated with sea-ice forcing. *2018 American Geophysical Union Annual Meeting*, Washington, DC (Dec 2018).
[**6**] **Labe, Z.M.,** Y. Peings, H.S. Stern, and G. Magnusdottir. Arctic sea ice thickness variability and its influence on the atmospheric response to projected sea ice loss. *Machine Learning and Physical Sciences (MAPS) Symposium*, University of California, Irvine (May 2018).
[**5**] **Labe, Z.M.** Disentangling Arctic climate change and variability. Geography Department, Irvine Valley College, CA (Apr 2018). (**Invited**)
[**4**] Thoman, R. and **Z.M. Labe**. 2017-18 Sea Ice in Western Alaska during the 2017-18 Season: Historical Context and Possible Drivers. *Western Alaska Interdisciplinary Science Conference and Forum*, Nome, AK (Mar 2018).
[**3**] **Labe, Z.M.,** G. Magnusdottir, and H.S. Stern. Variability and future projections of Arctic sea ice thickness. *Understanding the Causes and Consequences of Polar Amplification Workshop*, Aspen Global Change Institute, Aspen, CO (Jun 2017).
[**2**] **Labe, Z.M.** Communicating the future of Arctic climate change. Natural Sciences Division, Fullerton College, CA (Nov 2016). (**Invited**)
[**1**] **Labe, Z.M.** Anomalously early onset of spring in the CESM Large Ensemble Project. *Earth and Atmospheric Science Undergraduate Research Symposium*, Cornell University, NY (May 2015).

POSTER PRESENTATIONS

[**5**] Holman, A., R. Thoman, **Z.M. Labe**, and J.E. Walsh. Not Just Chance: Ocean and Atmospheric Factors in the Record Low Bering Sea Ice Winter of 2017-2018 and effects on health and safety, *2018 American Geophysical Union Annual Meeting*, Washington, DC (Dec 2018).
[**4**] **Labe, Z.M.** Loss of Arctic sea ice thickness affects the large-scale atmosphere, *Arctic System Change Workshop* at NCAR, Boulder, CO (Apr 2018).
[**3**] **Labe, Z.M.,** G. Magnusdottir, and H.S. Stern. Arctic Sea Ice Thickness Variability and the Large-scale Atmospheric Circulation Using Satellite Observations, PIOMAS, and the CESM Large Ensemble, *14th Conference on Polar Meteorology and Oceanography*, Seattle, WA (Jan 2017).
[**2**] **Labe, Z.M.,** G. Magnusdottir, and H.S. Stern. Making the most of Arctic sea ice thickness observations, *Symposium on Recent Advances in Data Science*, University of California, Irvine (Oct 2016).
[**1**] **Labe, Z.M.** and T.R. Ault. Anomalously Early Onset of Spring in the CESM Large Ensemble Project, *14th Annual AMS Student Conference*, Phoenix, AZ (Jan 2015).

TEACHING & OUTREACH

University of California, Irvine

Fa. 2019	Teaching Assistant, Terrestrial Hydrology
Sp. 2019	Teaching Assistant, Earth System Physics
Wi. 2019	Teaching Assistant, Weather Analysis
Fa. 2016	Teaching Assistant, Fundamental Processes in Earth and Environmental Studies

Cornell University

Su. 2015	Guest Lecturer, Severe Weather Phenomena
Sp. 2015	Teaching Assistant, Programming and Meteorology Software (Python)
Fa. 2014	Teaching Assistant, Basic Principles of Meteorology Lab

PROFESSIONAL ACTIVITIES

2019-2021	Student Board Member, American Meteorological Society's Board on Societal Impacts
2018 –	Journal Manuscript Referee - *Geophysical Research Letters*, *Journal of Climate*, *Journal of Geophysical Research: Atmospheres*, *Journal of Glaciology*, *Nature Climate Change*, *Polar Geography*
2017-2020	Vice President & Communications Chair, Student Chapter of the American Meteorological Society at the University of California, Irvine
2017-2021	Student Board Member, American Meteorological Society's Committee on Climate Variability and Change
2017-2018	Member, Student Communications Working Group, University of California, Irvine
Aug. 2017	Expert Contributor to the UCAR Climate Data Guide: "Sea Ice Thickness Data Sets: Overview & Comparison Table"
2014-2015	President, American Meteorological Society Student Chapter, Cornell University

Affiliations/Memberships

2020 –	American Association for the Advancement of Science (AAAS), Member
2016 –	Association of Polar Early Career Scientists (APECS), Member
2015 –	American Geophysical Union (AGU), Member
2014 –	National Weather Association (NWA), Member
2009 –	American Meteorological Society (AMS), Member

Field Work

May 2017	INTPART Arctic Field Summer Schools: Norway–Canada–USA collaboration, University of Tromsø, Norway (Workshops); Longyearbyen, Svalbard (R/V *Lance* - sea ice)

Workshops

Oct. 2019	Transdisciplinary Research on the Changing Arctic and Its Global Impacts: Enhancing Capacity for Convergence Science, Beckman Center of the NAS, Irvine, CA
Apr. 2018	Arctic System Change Workshop, Mesa Lab, National Center for Atmospheric Research (NCAR), Boulder, CO
Jun. 2017	Understanding the Causes and Consequences of Polar Amplification, Aspen Global Change Institute, Aspen, CO

TECHNICAL SKILLS

Programming: Python, `MATLAB`, `R`, Fortran, Unix, HTML, TEX, LATEX, BibTEX
Other Tools: NCL, PyNGL/PyNIO, NCO, CDO, GrADS, Git

EDUCATIONAL OUTREACH

Mar. 2020	*Climate, Literacy, Empowerment And iNquiry (CLEAN)*, The Cryosphere Outreach event, MacArthur Fundamental Intermediate School, Santa Ana, CA (**Presenter**)
Feb. 2020	*Irvine Unified School District's 39th Annual Science Fair*, Physical science project judge, Irvine, CA (**Volunteer**)
Jan. 2020	*100th American Meteorological Society Annual Meeting*: Side Panel - Using Social Media to Communicate Climate Science, Boston, MA. (**Chair**)
Nov. 2019	*Department of Earth System Science*, Improving scientific graphics of climate (change) data, University of California, Irvine, CA. (**Presenter**)
Oct. 2019	*Irvine Unified School District*, "Ask-A-Scientist/Engineer Night" at Creekside High School, Orange County, CA (**Volunteer**)
Sep. 2019	*Geological Society of America Annual Meeting*, Geoscience Communication in the Modern Age – "A Changing Arctic", Phoenix, AZ (**Contributed Art**)
Sep. 2019	*UC Irvine Graduate Orientation*, Session Title – Healthy Student Life – The Current Student Perspective, Irvine, CA (**Panelist**)
May. 2019	*College and Career Day Experience*, MacArthur Fundamental Intermediate School, Santa Ana, CA (**Presenter**)
Apr. 2019	*Vista Verde School*, Weather and climate booth at an Earth Science Day fair, Irvine, CA (**Presenter**)
Mar. 2019	*Climate, Literacy, Empowerment And iNquiry (CLEAN)*, Weather and Climate Outreach event, MacArthur Fundamental Intermediate School, Santa Ana, CA (**Presenter**)
Feb. 2019	*Orange County Regional Science Olympiad*, Climate Science-Meteorology exam writer and proctor, Irvine, CA (**Event Supervisor**)
Feb. 2019	*Climate, Literacy, Empowerment And iNquiry (CLEAN)*, The Cryosphere Outreach event, MacArthur Fundamental Intermediate School, Santa Ana, CA (**Presenter**)
Dec. 2018	*NOAA*, Arctic Report Card - Update for 2018.
Oct. 2018	*Brews and Brains: TED-Style Talk*, Our Changing Arctic, Fireside Tavern, Costa Mesa, CA. (**Invited Presenter**).
Oct. 2018	*Unified Irvine School District*, "Ask-A-Scientist/Engineer Night" at Rancho San Joaquin Middle School, Orange County, CA (**Volunteer**)
Sep 2018	*UC Irvine Graduate Orientation*, Session Title – Student Panel – Embracing Your New Graduate Life, Irvine, CA (**Panelist**)
May 2018	*Vista Verde School*, Weather and climate booth at an Earth Day fair, Irvine, CA (**Presenter**)
Feb. 2018	*Irvine Unified School District's 37th Annual Science Fair*, Physical science project judge, Irvine, CA (**Volunteer**)
Feb. 2018	*Climate, Literacy, Empowerment And iNquiry (CLEAN)*, Weather and Climate Outreach event, MacArthur Fundamental Intermediate School, Santa Ana, CA (**Presenter**)

Feb. 2018 *Orange County Regional Science Olympiad*, Climate Science-Meteorology exam writer and proctor, Irvine, CA (**Event Supervisor**)

Feb. 2018 *Climate, Literacy, Empowerment And iNquiry (CLEAN)*, The Cryosphere Outreach event, MacArthur Fundamental Intermediate School, Santa Ana, CA (**Presenter**)

Sep. 2017 *Unified Irvine School District*, "Ask-A-Scientist/Engineer Night" at Rancho San Joaquin Middle School, Orange County, CA (**Volunteer**)

Aug. 2017 *Unified Irvine School District*, "Ask-A-Scientist/Engineer Night" at Rancho San Joaquin Middle School, Orange County, CA (**Volunteer**)

Aug. 2017 *NASA DIRECT-STEM Program*, Assessing a changing Arctic (**Invited Presenter**).

Apr. 2017 *Climate Data Hackathon*, Looking for clues to changes in Arctic sea ice, University of California, Irvine. (**Invited Presenter**).

Feb. 2017 *Irvine Unified School District's 36th Annual Science Fair*, Physical science project judge, Irvine, CA (**Volunteer**)

Feb. 2017 *Orange County Regional Science Olympiad*, Severe Storms-Meteorology exam writer and proctor, Irvine, CA (**Event Supervisor**)

Wi. 2017 Seminar Course – Teaching Topics in Earth System Science (**Training**)

Oct. 2016 *Unified Irvine School District*, "Ask-A-Scientist/Engineer Night" at Rancho San Joaquin Middle School, Orange County, CA (**Volunteer**)

Aug. 2016 *NASA DIRECT-STEM Workshop*, Data and Analysis of Arctic Climate Change in CMIP5 using Python (**Instructor**).

NEWS & MEDIA OUTREACH

Selected Interviews/Quotes/Contributions

2020 Euronews, Mashable, The Journal of the Data Visualization Society, Washington Post

2019 Axios, Carbon Brief, CBS News, Earther, Euronews, Expressen, Forbes, Guardian, The Hill, Heidi.news, Mashable, Motherboard, Popular Science, TIME, Washington Post, Wunderground

2018 Arctic Today, The Atlantic, Carbon Brief, Earther, Euronews, Grist, High North News, KTUU Anchorage, KUCI Radio, O Globo, PennLive, UT Austin Geoscience Blogs, United States Senate, Val 202, Washington Post

2017 Buzzfeed News, Carbon Brief, Climate Central, KUAC Alaska, Mashable, Sydney Morning Herald, UCI News, USA Today, Verge, Washington Post, Yahoo News

2016 American Geophysical Union Blogs, Climate Central, Cornell University News, Forbes, Mashable, New York Times, National Public Radio, Sydney Morning Herald, Vox, Washington Post, The Weather Channel, Wunderground, Yahoo News

2010-2015 The Ithaca Voice, The Patriot News, Wunderground

ABSTRACT OF THE DISSERTATION

The effects of Arctic sea-ice thickness loss and stratospheric variability on mid-latitude cold spells

By

Zachary M. Labe

Doctor of Philosophy in Earth System Science

University of California, Irvine, 2020

Professor Gudrun Magnusdottir, Chair

The Arctic is a key indicator of global climate change. Annual surface temperatures are increasing at more than twice the rate of the global average, and passive microwave satellite observations of Arctic sea-ice extent show a loss of nearly 40% over the last few decades. Despite recent advances in climate models, availability of observations, and statistical analysis, our understanding of ice-ocean-atmosphere interactions, and the teleconnections between the Arctic and other regions, remains incomplete. Assessing the atmospheric response to the rapid changes in Arctic sea ice will help to determine future societal impacts from climate change, including extreme weather events in the densely populated mid-latitude regions.

The broad objective of this thesis is to improve our understanding of Arctic climate variability. To be more specific, this dissertation will explore (i) the internal variability of Arctic sea-ice thickness (SIT), (ii) the atmospheric response to thinning sea ice, and (iii) the role of stratospheric and tropospheric pathways in modulating Arctic-mid-latitude teleconnections. SIT has an important effect on the Arctic energy budget, and therefore it is critical to represent it accurately in global climate models. However, limited observations of SIT (satellite-derived and in situ) have prevented a robust analysis of the atmospheric response

to its spatial and temporal variability. Here, I use perturbation experiments in a high-top atmospheric global climate model to examine the importance of stratosphere-troposphere coupling and other causal pathways for teleconnections between Arctic sea ice and the mid-latitudes.

Internal variability contributes to an uncertainty of 10-20 years in the timing of future mean SIT falling below 0.5 m in a large ensemble of simulations of a fully-coupled global climate model. This loss of SIT is found to reinforce the large-scale tropospheric response to Arctic sea-ice concentration and contributes up to one third of the surface warming response. Using a high-top model, the Quasi-biennial Oscillation (QBO) is found to significantly modulate the response to Arctic sea-ice decline. The stratospheric polar vortex weakens in response to sea-ice forcing during easterly QBO winters. However, there is little-to-no stratospheric response to sea-ice loss during the westerly phase of the QBO. Finally, in a series of coordinated coupled and uncoupled global climate model perturbation experiments, the "warm Arctic, cold Siberia" temperature anomaly pattern is found to be closely related to the strength of the Siberian High and mid-tropospheric warming response. By comparing simulations that are directly forced with warmer temperature in the Arctic region (corresponding to projected changes), to sea-ice forced experiments (where the forcing corresponds to the same future time), it is shown that sea-ice loss alone is insufficient to bring about the entire thermal signature of Arctic amplification.

Chapter 1

Introduction

1.1 Arctic amplification

Through positive feedbacks in the climate system, the annual mean surface temperature in the Arctic is rising more than twice as fast as the globally-averaged mean – this phenomenon is known as "Arctic amplification" (AA; Manabe and Stouffer, 1980; Holland and Bitz, 2003; Alexeev et al., 2005; Winton, 2006; Serreze and Francis, 2006; Serreze et al., 2009; Serreze and Barry, 2011; Screen and Simmonds, 2010b; Cohen et al., 2014; Pithan and Mauritsen, 2014; Cohen et al., 2019). Figure 1.1 shows the zonal-mean signature of observed AA as a function of time, with amplified surface warming found in the Arctic over the last 1-2 decades relative to other latitudinal bands. Losses of total sea-ice concentration (SIC) and therefore sea-ice extent (SIE) have also been observed in all months of the year (Onarheim et al., 2018; Stroeve and Notz, 2018). Changes in sea ice and snow cover are just one of the drivers to AA through the ice-snow-albedo feedback (Screen and Simmonds, 2010b). Large areas of open water, which would otherwise be ice-covered, absorb more incoming solar radiation and increase the exchange of surface (sensible and latent) heat fluxes between the ocean and at-

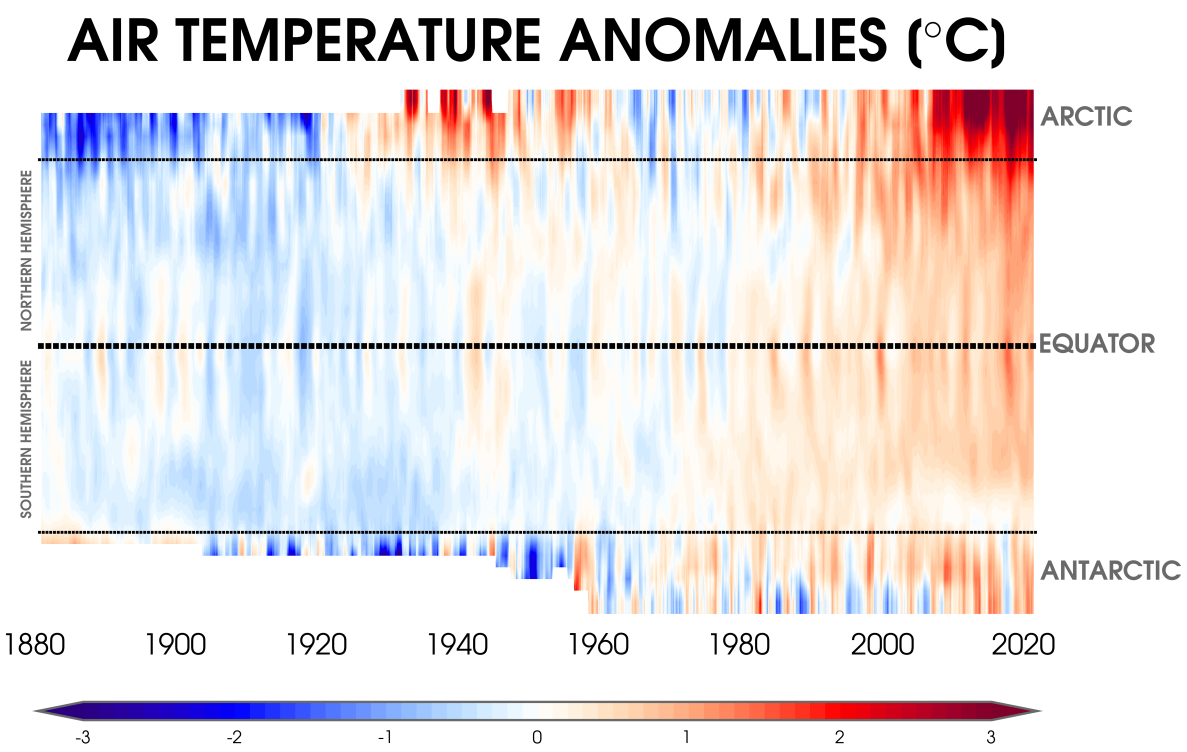

Figure 1.1: Zonal-mean surface temperature anomalies using a 12-month running mean as a function of latitude (-90°S–90°N) and time (1880-2020). Anomalies are calculated from a mean 1951-1980 climatology (GISTEMPv4; Lenssen et al., 2019; GISTEMP Team, 2020). Missing data is masked out in white.

mosphere. This heat is absorbed during summer in ice-free areas and then is released to the atmosphere as sea ice refreezes in the fall and winter. This "delayed warming" mechanism contributes to the largest Arctic surface air temperature trends during the fall and winter (Screen and Simmonds, 2010a). Both thinning sea ice and loss of SIC contribute to this larger exchange of surface heat fluxes (Screen and Simmonds, 2010a; Lee et al., 2017), which further inhibits new sea ice growth (Markus et al., 2009). This has important implications for resolving the seasonal Arctic energy budget and atmospheric/oceanic heat transport (Serreze et al., 2007).

However, the thermodynamic contributions from losses of sea ice and snow primarily contribute to only surface-based AA (Kumar et al., 2010; Perlwitz et al., 2015; Cohen et al., 2019). Accelerating warming trends are also occurring vertically-aloft into the middle-to-upper troposphere of the Arctic (Graversen et al., 2008; Screen and Simmonds, 2011; Alexeev et al., 2012). In addition to changes in surface albedo, other processes involving water vapor and cloud cover (Francis and Hunter, 2007; Graversen and Wang, 2009; Ghatak and Miller, 2013; Sedlar et al., 2011; Kay et al., 2016), mid-latitude cyclones (Higgins and Cassano, 2009), lapse-rate temperature feedbacks (Bintanja et al., 2012; Pithan and Mauritsen, 2014), extreme meridional moisture transport (Woods and Caballero, 2016; Woods et al., 2017; Yang and Magnusdottir, 2017, 2018; Messori et al., 2018), ocean heat transport (Timmermans et al., 2018), and remote sea surface temperatures (SST) (Screen et al., 2012; Perlwitz et al., 2015) have all been suggested as contributions to the recent dramatic Arctic warming and variability in sea ice. A detailed summary of the many complexities of polar climate feedbacks can be found in Goosse et al. (2018).

1.2 Arctic sea-ice variability

Passive microwave satellite observations, since 1978/1979, provide the most temporally-complete record of Arctic sea-ice variability and trends during this period of AA. Many previous studies have quantified these long-term trends (e.g., Parkinson et al., 1999; Cavalieri and Parkinson, 2012; Serreze and Stroeve, 2015; Stroeve and Notz, 2018; Serreze and Meier, 2019) with losses of SIE approaching 13% per decade during the summertime. While wintertime losses of SIE are smaller, long-term trends are statistically significant in all months of the year (Stroeve and Notz, 2018). Various reconstructions of summer Arctic SIE suggest that the current rate of decline is unprecedented in at least the last 1450 years (Kinnard

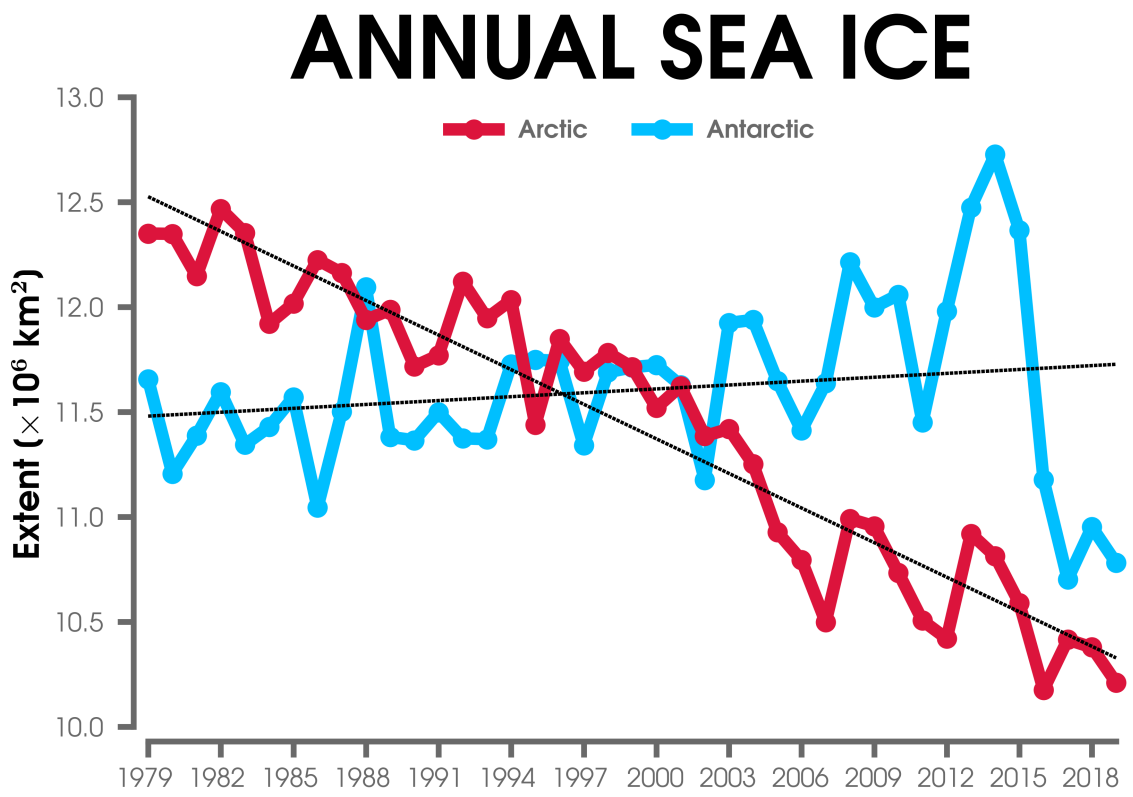

Figure 1.2: Average annual mean sea ice extent for the Arctic (red line) and Antarctic (blue line) from 1979 to 2019 (Sea Ice Index, version 3.0; Fetterer et al., 2017). The dashed black lines indicate the linear (least squares) trend.

et al., 2011; Walsh et al., 2016; Zhang et al., 2018b). Figure 1.2 shows the annual mean changes in Arctic and Antarctic SIE from 1979 to 2019. Although the rate of Arctic SIE is clearly downward, there is a small, but statistically significant increasing trend in annual Antarctic SIE during the satellite era (Parkinson, 2019). This increasing trend is not simulated by the latest generation of global climate models (Roach et al., 2020) and remains an interesting topic for scientific debate (e.g., Turner et al., 2013). Nevertheless, the focus of this dissertation will be on Northern Hemisphere climate variability.

Along with losses of SIC and SIE, Arctic sea ice is becoming younger and thinner. The average sea-ice thickness (SIT) in the central Arctic has thinned by approximately 2 m since

the 1980s (Kwok, 2018). Further, the area of multi-year sea ice has shrunk by 50% over the duration of the scatterometer record (Maslanik et al., 2011; Kwok, 2018). Simulated reconstructions of Arctic SIT show that the rate of thinning is unprecedented since at least the start of the 20th century (Schweiger et al., 2019). Increases in the length of the summer melt season have also been observed due to changes in the melt onset and freeze onset of sea ice (Stroeve et al., 2014b; Smith and Jahn, 2019). Nevertheless, it remains challenging to attribute the contributions to these trends from internal variability versus greenhouse-gas forcing. For instance, Notz and Stroeve (2016) showed a link between Arctic SIE and cumulative anthropogenic CO_2 emissions through an observed linear relationship. Yet, the contributions from natural variability to Arctic sea-ice losses are large and range up to to 50% (Stroeve et al., 2007; Kay et al., 2011a; Stroeve et al., 2012; Ding et al., 2017, 2019). Internal variability also contributes to substantial spatial variability in the trends of SIC (Onarheim et al., 2018; England et al., 2019) with the largest recent declines found in the Barents, Beaufort, Chukchi, East Siberian, and Laptev Seas (e.g., Kwok and Cunningham, 2010; Stroeve et al., 2011; Li et al., 2017; Onarheim and Årthun, 2017). In the last few years, several extreme Arctic warming events (e.g., Boisvert et al., 2016; Moore, 2016; Graham et al., 2017; Kim et al., 2017; Binder et al., 2017; Moore et al., 2018) and rapid sea-ice loss events (e.g., Holland et al., 2006; Döscher and Koenigk, 2013; Thoman et al., 2020) have coincided with larger trends in winter sea-ice decline (Petty et al., 2018; Stroeve and Notz, 2018). It is still not well understand how these anomalous synoptic-scale events may impact future AA and regional sea-ice variability (Messori et al., 2018).

Moving forward, there is a lot of interest in the timing of an "ice-free" (less than 1 million km^2) Arctic summer (Overland and Wang, 2007, 2013), especially in relation to levels of 1.5°C and 2°C of global warming above pre-industrial levels (Mahlstein and Knutti, 2012; Sigmond et al., 2018; Jahn, 2018; Screen, 2018). The recent declining trend in average Arctic SIE is generally within the multi-model ensemble spread, but lower than the multi-model

mean (Stroeve et al., 2007; Notz et al., 2020). Again, this may be due internal variability (Swart et al., 2015) or model biases (Rosenblum and Eisenman, 2017). Regardless of emission scenario, nearly all of the next generation of global climate models simulate the first "ice-free" Arctic summer before 2050 (Notz et al., 2020).

1.3 Local and remote impacts of Arctic warming

To understand the physical mechanisms between AA and the mid-latitude atmospheric circulation in the presence of a limited (spatially and temporally) observational record, we need to use general circulation model (GCM) simulations. At the same time, separating the forced response (signal) from internal variability (noise) remains a difficult challenge in evaluating climate change and variability (Hawkins and Sutton, 2012; Deser et al., 2012; Thompson et al., 2015; Barnes et al., 2019; Deser et al., 2020; Hawkins et al., 2020; Lehner et al., 2020). Moreover, uncertainties and biases in global climate models, along with their representation of atmospheric internal variability (Knutson et al., 2013; Lehner et al., 2020), create additional challenges in detecting the signal-to-noise ratio (Mahlstein et al., 2012; Hawkins et al., 2020).

Substantial variability in Arctic temperature and sea ice can be found on decadal and multi-decadal time-scales (Johannessen et al., 2004; Zhang et al., 2008; Zhang, 2015; Tokinaga et al., 2017). While further sea-ice loss and surface warming is expected to continue through the 21st century, there remains a large spread in global climate model projections (Liu et al., 2013; Barnes and Polvani, 2015) due to model uncertainties, different emission scenarios, and internal variability. As previously mentioned, global climate models have generally underestimated the rate of SIE loss over the last decade when compared with satellite observations (Stroeve et al., 2012; Wang and Overland, 2012; Notz et al., 2020). But models

that are consistent with actual observations may not even be simulating the right physical processes (Rosenblum and Eisenman, 2017). It is therefore important to address how the forced response (from greenhouse gas emissions) and atmospheric internal variability may be having a role in characterizing Arctic climate variability when using global climate models.

The first evidence of linkages between the Arctic and mid-latitudes appeared in early GCM experiments nearly 50 years ago (Newson, 1973; Warshaw and Rapp, 1972). After removing Arctic sea ice from the polar cap in a simple GCM, Newson (1973) found a weakening of the mid-latitude westerlies and dynamical cooling response over North America and Eurasia. Since then, there has been widespread scientific interest in understanding the relationships between Arctic sea-ice loss, polar warming, and the response of the mid-latitude circulation. While there have been countless review papers and perspective pieces in the last few years, there remains little-to-no agreement on how the Arctic may be linked to mid-latitude weather and climate (see within: Vihma, 2014; Cohen et al., 2014; Barnes and Screen, 2015; Overland et al., 2016; Francis, 2017; Francis et al., 2017; Screen, 2017a; Screen et al., 2018a; Cohen et al., 2018; Screen et al., 2018b; Vavrus, 2018; Coumou et al., 2018; Smith et al., 2019; Cohen et al., 2019).

Several dynamical pathways have been proposed for teleconnections propagating out of the Arctic during winter (Cohen et al., 2014, 2018), including but not limited to, a tropospheric pathway through the modulation of stationary Rossby waves excited in the vicinity of the Barents-Kara Seas region (e.g., Honda et al., 2009), a downward propagation of anomalies projecting onto the North Atlantic/Arctic Oscillation ((N)AO) due to a warming of the stratospheric polar vortex (e.g., Kim et al., 2014), a weakening and increase in amplitude of the eddy-driven jet due to a reduction in the horizontal thickness gradient (e.g., Francis and Vavrus, 2012), or a combination of all of these interactions (e.g., Peings and Magnus-

dottir, 2014). However, teleconnections between the Arctic and mid-latitudes do not occur in isolation. While the response to AA has been proposed to shift the eddy-driven jet equatorward (Blackport and Kushner, 2017), upper-troposphere tropical warming (UTW), due to greenhouse-gas forcing, has the tendency to shift the jet poleward. This dynamical "tug-of-war" (between AA and UTW) complicates projections of changes in the strength and position of the polar jet due to climate change (Harvey et al., 2014; Barnes and Polvani, 2015; Shaw et al., 2016; Peings et al., 2018; Zappa et al., 2018; Peings et al., 2019). Due to these uncertainties, global climate models continue to simulate a wide-range of extratropical circulation responses to climate change over the 21st century (Shepherd, 2014).

To first isolate the effect of Arctic climate change, many studies have performed numerical modeling experiments by prescribing changes in sea ice boundary conditions (e.g., Alexander et al., 2004; Deser et al., 2004; Magnusdottir et al., 2004; Deser et al., 2010; Petoukhov and Semenov, 2010; Blthgen et al., 2012; Porter et al., 2012; Screen et al., 2013; Mori et al., 2014; Peings and Magnusdottir, 2014; Screen et al., 2014; Semmler et al., 2016a; Screen, 2017b; England et al., 2018). Although there are a few robust similarities between these studies, such as a weakening of the mid-latitude westerlies, increases in local near-surface air temperature and precipitation, and a strengthening of the Siberian High, there are also large uncertainties in the remote response due to model structural biases, (lack of) interactive ocean coupling, and differences in surface forcing. Further, internal variability and the choice of statistical methods to examine the mid-latitude circulation response can lead to contrasting interpretations of Arctic-mid-latitude linkages (e.g., Francis and Vavrus, 2012; Barnes, 2013; Ayarzagüena and Screen, 2016; Cattiaux et al., 2016; Kretschmer et al., 2017; Mori et al., 2019; Screen and Blackport, 2019b; Blackport and Screen, 2020; Yu et al., 2020). In summary, quantifying future Arctic climate change and its remote impacts are challenging problems in the field of climate dynamics.

1.4 Scope and organization of dissertation

The purpose of this dissertation is to improve our understanding on the connections between Arctic sea-ice variability and the extratropical atmospheric circulation in boreal winter. Despite recent advances in climate models, statistical methods, and observational data sets, there is still no consensus on weather and climate linkages between the Arctic and mid-latitudes. Motivated by these contrasting results, this thesis uses a series of state-of-the-art GCM perturbation experiments to improve our understanding on the causal and physical mechanisms supporting these linkages. In particular, this evaluation provides the first comprehensive overview on the influence of Arctic SIT variability and the QBO in explaining the atmospheric response to sea-ice decline. The results of this dissertation have implications for advancing our knowledge on complex (non)linear interactions important for stratosphere-troposphere coupling, refining future climate model projections of extratropical climate variability, and improving our understanding on the effects of Arctic warming and sea-ice loss in a warming world.

The introduction (Chapter 1) is intended to provide an accessible overview with broad references on Arctic climate change and the challenges in linking the Arctic to lower-latitude weather and climate. Comparatively, the other chapters will provide more specific introductions behind the targeted climate model experiments used in each study.

In Chapter 2, I present a comprehensive overview of historical and future Arctic sea-ice thickness variability in a collection of observational and modeled data sets. I first compare the spatial variability, temporal variability, and long-term trends of Arctic sea-ice thickness in submarine data and satellites (ICESat and CryoSat-2) to a reanalysis-like product (PIOMAS). After validating PIOMAS with historical observations, I compare this reanalysis

product to the Community Earth System Large Ensemble Project (LENS) using empirical orthogonal function (EOF) analysis. This research is one of the first to make use of an initial-condition large ensemble to assess the internal variability of Arctic sea-ice thickness. Finally, I evaluate changes in the variability and mean-state of Arctic sea-ice thickness in LENS through the 21st century. Specifically, I look at the timing of a future "ice-free" Arctic summer in different marginal seas by considering both sea-ice thickness and sea-ice volume. Overall, I address the following questions in this chapter:

i How well do satellite and submarine observations of Arctic sea-ice thickness compare to a coupled ice-ocean model assimilation system (PIOMAS)?

ii Using a large ensemble conducted with a fully-coupled global climate model, how will the spatial and temporal variability of Arctic sea-ice thickness change over the 21st century?

iii What is the role of regional sea-ice thickness variability for predicting a future "ice-free" Arctic summer?

This work is published in *Journal of Climate*.

> **Labe, Z.M.**, G. Magnusdottir, and H.S. Stern (2018), Variability of Arctic sea-ice thickness using PIOMAS and the CESM Large Ensemble, *Journal of Climate*, 31(8), 3233-3247, doi: 10.1175/JCLI-D-17-0436.1.

Building off of the results in Chapter 2, in Chapter 3, I analyze the effect of including sea-ice thickness variability in global climate model perturbation experiments. Specifically, I conduct a series of perturbation experiments using a high-top model to quantify the relative contributions from sea-ice concentration and sea-ice thickness anomalies on the total atmospheric response to Arctic sea-ice decline. The relative contributions are evaluated using pattern correlations for both the surface and free troposphere/stratosphere responses. The

effects of sea-ice thickness anomalies on linear wave interference and stratosphere-troposphere coupling are also considered. Overall, I address the following questions in this chapter:

i Is knowledge of Arctic sea-ice thickness variability important for resolving the large-scale atmospheric response to Arctic sea-ice decline in climate models?

ii Does the effect of Arctic sea-ice thickness loss reinforce the response to sea-ice concentration anomalies?

iii What is the relationship between regional Arctic sea-ice thickness anomalies and the response of the stratospheric polar vortex?

This work is published in *Geophysical Research Letters*.

> **Labe, Z.M.**, Y. Peings, and G. Magnusdottir (2018), Contributions of ice thickness to the atmospheric response from projected Arctic sea-ice loss, *Geophysical Research Letters*, 45(11), 5635-5642, doi :10.1029/2018GL078158.

To better understand the role of the stratosphere in Arctic-mid-latitude linkages, in Chapter 4, I examine the influence of the Quasi-biennial Oscillation (QBO) in modulating the atmospheric response to Arctic sea-ice loss in boreal winter. Specifically, I conduct a series of large ensemble experiments using a high-top model with a prescribed repeating cycle of the QBO and then composite the responses to sea-ice anomalies by the easterly and westerly phases of the QBO. I propose a chain of physical mechanisms that explain how the QBO modulates the surface response and discuss the importance of the background state in sea ice perturbation experiments. This study is the first to investigate a connection between the phase of the QBO and the large-scale atmospheric response to Arctic sea-ice melt. Overall, I address the following questions in this chapter:

i What is the role of the Quasi-biennial Oscillation (QBO) in modulating teleconnections related to Arctic sea-ice forcing in perturbation experiments?

ii How does the QBO affect the "warm Arctic, cold Siberia" temperature anomaly pattern in response to sea-ice decline?

iii Are the effects of the QBO sensitive to the magnitude of surface forcing?

This work is published in *Geophysical Research Letters*.

> **Labe, Z.M.**, Y. Peings, and G. Magnusdottir (2019), The effect of QBO phase on the atmospheric response to projected Arctic sea-ice loss in early winter, *Geophysical Research Letters*, 46(13), 7663-7671, doi :10.1029/2019GL083095.

In Chapter 5, I conduct and analyze a large collection of coordinated atmospheric and coupled global climate model perturbation experiments associated with the new Polar Amplification Model Intercomparison Project (PAMIP), which is contributing to the the sixth phase of the Coupled Model Intercomparison Project (CMIP6). To understand the role of mid-tropospheric warming on Arctic-mid-latitude teleconnections, I compare the sea ice-only forcing experiments in PAMIP to simulations that use a nudging method to prescribe the full effect of future Arctic amplification. Specifically, I describe an emergent relationship between the response of the high-latitude 1000-500 hPa atmospheric thickness layer and a strengthening of the Siberian High. The results of this analysis have implications for understanding the "warm Arctic, cold Siberia" temperature anomaly pattern in future climate model projections. Overall, I address the following questions in this chapter:

i What are the differences in the vertical extent of warming between climate model experiments prescribed with sea-ice anomalies compared to experiments nudged with Arctic amplification forcing?

ii Are the responses to increasing levels of Arctic amplification linearly additive in the troposphere and stratosphere?

iii What is the relationship between middle-to-upper tropospheric Arctic warming and cold surface temperature extremes in eastern Asia?

This work is in review at *Geophysical Research Letters*.

> **Labe, Z.M.**, Y. Peings, and G. Magnusdottir (2020), Warm Arctic, cold Siberia pattern: role of full Arctic amplification versus sea-ice loss alone, under review at *Geophysical Research Letters*.

In Chapter 6, I summarize the main findings of this thesis. I also provide a brief discussion on future directions for work in resolving Arctic-mid-latitude linkages, particularly in climate model studies. Note that work in Chapters 2, 3, and 4 are slightly modified versions of previously published journal articles. A list of references for all chapters and an appendix can be found at the very end of the dissertation.

Chapter 2

Variability of Arctic sea-ice thickness using PIOMAS and the CESM Large Ensemble

As appears in:

Labe, Z.M., G. Magnusdottir, and H.S. Stern (2018), Variability of Arctic sea-ice thickness using PIOMAS and the CESM Large Ensemble, *Journal of Climate*, 31(8), 3233-3247, doi: 10.1175/JCLI-D-17-0436.1.

Abstract

Due to limited high quality satellite and in situ observations, less attention has been given to the trends in Arctic sea-ice thickness and therefore sea-ice volume than to the trends in sea-ice extent. This study evaluates the spatial and temporal variability in Arctic sea-ice thickness using the Pan-Arctic Ice-Ocean Modeling and Assimilation System (PIOMAS).

Additionally, the Community Earth System Model Large Ensemble Project (LENS) is used to quantify the forced response and internal variability in the model. A dipole spatial pattern of sea-ice thickness variability is shown in both PIOMAS and LENS with opposite signs of polarity between the East Siberian Sea and near the Fram Strait. As future sea ice thins, this dipole structure of variability is reduced, and the largest interannual variability is found only along the northern Greenland coastline. Under a high emissions scenario (RCP8.5) projection, average September sea-ice thickness falls below 0.5 m by the end of the 21st century. However, a regional perspective shows internal variability contributes to an uncertainty of 10 to 20 years for the timing of the first September sea-ice thickness less than 0.5 m in the marginal seas.

2.1 Introduction

Climate in the Arctic is undergoing rapid change as the Arctic mean surface temperature is rising at twice the rate of the global mean surface temperature. Accompanying this Arctic Amplification is a widespread loss of Arctic sea ice. Quality observations of sea-ice concentration (SIC) and therefore total sea-ice extent (SIE) are available from satellites covering the entire Arctic from 1979. Observations of sea-ice thickness (SIT) are very scant by comparison (e.g., Lindsay and Schweiger, 2015). In terms of affecting surface turbulent heat fluxes in the Arctic and therefore allowing communication between the atmosphere and the underlying ocean, variability in SIC, or the fraction of the grid cell that is covered by sea ice, is more important than SIT. However, it is not clear how sensitive the atmosphere is to variability in SIT. Previous studies of the effects of sea ice forcing in an atmospheric global climate model (e.g., Peings and Magnusdottir, 2014) have shown that the atmosphere is quite sensitive to the spatial pattern of SIC forcing. Certain spatial patterns of surface forcing in late fall or early winter will excite Rossby waves that may constructively interfere with the

climatological stationary waves leading to perturbations of the stratospheric polar vortex. These perturbations may affect the tropospheric flow some weeks later or in late winter (Peings and Magnusdottir, 2014). It is reasonable to assume that the same may apply to SIT forcing, especially when perturbations are enforced in areas of thin ice where the heat flux response is greater. Indeed, Lang et al. (2017) find that thinning Arctic sea ice is a driver of changes in surface heat flux and may locally contribute to surface warming of up to 1°C per decade in winter. The issue of the relative importance of SIT forcing compared to SIC forcing remains to be quantified. In this paper, we prepare the groundwork for exploring this issue by examining SIT variability.

Since SIT observations remain scant, we resolve to using a sea-ice/ocean, model-produced SIT data set, hereafter referred to as PIOMAS (Pan-Arctic Ice Ocean Modeling and Assimilation system; Zhang and Rothrock, 2003). Surface meteorological fields (e.g., temperature and wind) as well as sea surface temperature, sea-ice velocity, and SIC are assimilated into PIOMAS, but not the scarce SIT data that are available. PIOMAS output in turn provides temporal and spatial coverage of SIT over the last several decades. Numerous studies (e.g., Schweiger et al., 2011; Laxon et al., 2013; Zygmuntowska et al., 2014; Stroeve et al., 2014a; Wang et al., 2016) have evaluated and compared the satellite and model-based products for their representation of SIT. While PIOMAS is model-produced or a reanalysis product, it provides a spatially and temporally complete simulation of Arctic SIT over the satellite era (from 1979).

Global climate model simulations of SIT, such as from the latest Coupled Model Intercomparison Project (CMIP5), indicate significant model uncertainty in the spatial distribution and variability of SIT (Blanchard-Wrigglesworth and Bitz, 2014; Stroeve et al., 2014a; Melia et al., 2015). In addition to model biases and intermodel spread, internal variability con-

tributes to large uncertainties in future Arctic climate conditions including SIT (e.g., Kay et al., 2011b; Swart et al., 2015; Jahn et al., 2016; Swart, 2017; Yang and Magnusdottir, 2018). We can address internal variability by using output from the recent Community Earth System Model Large Ensemble project (CESM-LENS; Kay et al., 2015). We use forty ensemble members of climate simulations for the twentieth and twenty-first centuries. The CESM is a later version of the model than the one that contributed to the CMIP5, and its atmospheric component (CAM5) has superior representations of physical processes in the Arctic and was the version used by Peings and Magnusdottir (2014). By averaging over all ensemble members, we estimate the forced signal in the climate system as internal variability has the characteristics of white noise. Here we assess pan-Arctic spatial and temporal variability of SIT in the LENS over the historical period (1920-2005) and in future projections (2006-2080) under a high emissions scenario (RCP8.5).

This paper is organized as follows. Section 2 describes SIT observations from submarine and satellite platforms, SIT from PIOMAS, and SIT data from LENS. Section 3 describes the methods of analysis. Results are presented in Section 4. In Section 4a, we assess the spatial and temporal variability of SIT from PIOMAS and compare with observational SIT products. In Section 4b, we evaluate trends and variability from the start of the historical LENS simulations (1920) through the PIOMAS record (until 2015). We also compare regional SIT measures/estimates between PIOMAS and LENS. In Section 4c, we investigate future projections of SIT, including the spatial patterns of sea ice thinning. Section 5 contains a summary of our study and some concluding remarks.

2.2 Data

Observations of sea-ice thickness (SIT) remain very sparse compared to observations of sea-ice concentration (SIC), which have a continuous satellite record from 1979 to the present. SIT is not measured directly by satellite, rather it is freeboard that is measured, or the height of the sea ice above the ocean surface, from which SIT may be calculated given the depth of snow on top of the sea ice and hydrostatic equilibrium. The one satellite mission (ICESat) evaluating SIT does not provide continuous measurements, rather they only offer readings over two periods of the annual cycle, close to the minimum SIT in fall and close to the maximum SIT in spring. While the other satellite mission (CryoSat-2) provides weekly and monthly data, its SIT estimates are only available during the cold season due to melt pond formation in the summertime. Only observations from submarines offer direct measurements of SIT, but those measurements are limited by small areal extent and sporadic temporal coverage. We are left with model generated fields for assessment of SIT for climate studies. Model assimilated products or reanalysis of SIT offers the aerial and temporal coverage that is required for a climate study over the observational period of SIC. For insight about possible SIT later in this century we call on the CESM large ensemble. By averaging over all 40 ensemble members we get a good approximation of the forced signal towards the end of the century, albeit from one climate model. Below, we further discuss each of these sources of SIT data.

2.2.1 Submarine

Submarine SIT data were retrieved from upward-looking sonar (ULS) instruments during missions in the 1980s and 1990s (Lindsay, 2010). We utilize gridded ULS data from 1986 to 1994 (available from `http://nsidc.org/data/NSIDC-0690/versions/1`). SIT in this data

set were interpolated onto a 100 km EASE grid (Brodzik et al., 2012) by averaging thicknesses within 70 km of a grid cell. A more comprehensive archive of ULS and mooring data (Unified Sea-Ice Thickness Climate Data Record) is provided by the University of Washington Polar Science Center (Lindsay, 2010).

2.2.2 ICESat and CryoSat-2

The poor spatial and temporal coverage of satellite data of Arctic SIT remains a significant challenge. Retrieved from its Geoscience Laser Altimetry System (GLAS), NASA's ICESat provided one of the first estimates of near pan-Arctic SIT measurements during 10 campaigns from 2003 through 2009. SIT is calculated from freeboard measurements following the methods of Kwok and Cunningham (2008) and Kwok and Rothrock (2009). Additionally, another data set of ICESat SIT is available from the NSIDC (available at `http://nsidc.org/data/docs/daac/nsidc0393_arctic_seaice_freeboard/index.html`) following the slightly different calculation of freeboard to SIT by Zwally et al. (2002). We focus on the JPL gridded data set (available at `https://rkwok.jpl.nasa.gov/icesat/index.html`) and therefore denote it as "ICESat-J." We have elected to use the JPL product of gridded SIT as its uncertainties have been widely assessed in prior comparisons (e.g., Kwok and Cunningham, 2008; Zygmuntowska et al., 2014). The ICESat campaigns ($\approx$ 34 days each) were selected to correspond with the climatological maximum (spring) and minimum (autumn) SIT. Thickness is derived from laser altimeter satellite measurements of freeboard (height of the ice above the ocean surface) and assuming hydrostatic equilibrium. Snow depth is estimated following the methods of Kwok and Cunningham (2008) by constructing daily snow fields from ECMWF snow accumulation. Zygmuntowska et al. (2014) provides a comprehensive overview of the uncertainties in these derived SIT estimates from ICESat.

The ESA launched the CryoSat-2 satellite in 2010, which similarly uses a radar altimetry system to measure freeboard and then further derives into SIT (Laxon et al., 2013) given the assumptions above. Again, biases and uncertainties may arise from snow and ice density calculations along with estimating the snow-ice interface. Laxon et al. (2013) finds a difference of 0.1 m in SIT when averaged over the Arctic domain compared to in situ observations. CryoSat-2 provides weekly and monthly data, but not in the summertime as a result of inaccuracies from radar backscattering over melt ponds. CryoSat-2 snow depth on multiyear ice is estimated from Warren et al. (1999). However, snow depth on first year ice is calculated from 50% of the Warren et al. (1999) snow depth estimates (Laxon et al., 2013). Considering the various methods and data sets, snow depth remains one of the greatest uncertainties in deriving SIT from freeboard altimetry measurements. In many cases, only climatological values of snow depth and densities of sea ice and snow are used in these estimations. Due to variable weather conditions in the Arctic, these climatologies may not be representative of the actual snow depth on top of ice.

2.2.3 PIOMAS

PIOMAS is a coupled ice-ocean model assimilation system (Zhang and Rothrock, 2003) forced by NCEP/NCAR reanalysis. Monthly SIT, SIC, and snow depth output fields are available from 1979. PIOMAS couples the Parallel Ocean Program ocean model (Smith et al., 1992) with a 12-category thickness and enthalpy sea-ice model (Zhang and Rothrock, 2003). The atmospheric forcing includes 2 m surface air temperature, 10 m surface winds, cloud fraction, and downwelling longwave radiation. Downwelling shortwave radiation is calculated following the methods of Parkinson and Washington (1979) using 2 m surface air temperature and cloud fraction. It should be noted that ice-ocean models (like PIOMAS) do not have an atmospheric model component and therefore are subject to inaccuracies

from the forcing reanalysis data (Hunke and Holland, 2007; Lindsay et al., 2014). Using PIOMAS forced by four different global reanalysis data sets, Lindsay et al. (2014) found a range in estimates of simulated sea-ice volume (SIV) trends, especially before any model bias correction is applied to each data set. Despite differences in the total trends of SIV, these simulations produced similar spatial patterns of SIT. PIOMAS has the capability of assimilating SIC, sea-ice velocity (Lindsay and Zhang, 2006), and sea surface temperature following the methods of Manda et al. (2005). However, PIOMAS does not currently assimilate any satellite SIT data. Snow depth is estimated from NCEP/NCAR precipitation, and Lindsay and Schweiger (2015) estimate the uncertainty to be approximately 0.1 m. The model is available on a generalized orthogonal curvilinear coordinate system with a mean resolution of 22 km with the highest resolution over the Greenland Sea, Baffin Bay and eastern Canadian Arctic Archipelago.

PIOMAS has been extensively validated with satellite, submarine, airborne, and in situ observations (e.g., Zhang and Rothrock, 2003; Schweiger et al., 2011; Laxon et al., 2013; Stroeve et al., 2014a; Wang et al., 2016) and compared well with these observations. Schweiger et al. (2011) found a less than 0.1 m mean difference and high pattern correlation ($r > 0.8$) between PIOMAS and ICESat SIT fields. Stroeve et al. (2014a) and Wang et al. (2016) found that PIOMAS overestimates thin ice and underestimates thick ice when compared with a variety of different observational data sets. Blanchard-Wrigglesworth and Bitz (2014) also show that PIOMAS and other ice-ocean models have damped variability due to their thermodynamic and dynamic mechanisms on simulated SIT, which may lead to its narrower distribution. While PIOMAS sea-ice fields are model-generated and sensitive to atmospheric reanalysis forcings, the spatial patterns, seasonal cycle, and trends in SIT and SIV are realistically reproduced. A closer analysis of PIOMAS uncertainty can be found by Schweiger et al. (2011). They find a SIV trend of -2.8×10^3 km^3 decade^{-1} (1979-2010) and estimate the uncertainty at 1×10^3 km^3 decade^{-1}. Comparing PIOMAS with available March and October ICESat

and CryoSat-2 data also demonstrates that PIOMAS may underestimate the trend in SIV loss (Schweiger et al., 2011).

While ICESat and CryoSat-2 provide recent satellite observations of SIT, their limited temporal availability ($\approx$ 5 years each) and limited areal coverage of SIT restrict the ability to quantify the interannual variability and long-term trends in the SIT and SIV records. Additionally, it has been shown (e.g., Zygmuntowska et al., 2014) that large uncertainties and biases may exist between satellite methods for ice age, ice density, and snow depth when deriving SIT. PIOMAS closely compares with observational (submarine and satellite) SIT spatial patterns and average SIT.

2.2.4 CESM Large Ensemble Project

To assess internal variability of Arctic SIT, we use the CESM Large Ensemble (LENS) consisting of 40 ensemble members covering 1920 to 2100. Each ensemble member is run with the fully coupled CESM1.1 model, forced using historical data from 1920 to 2005, and then followed by a RCP8.5 scenario from there on to 2100. The large number of ensemble members is useful in characterizing the internal variability in the climate system, and thereby isolating the forced signal.

Previous studies (e.g., Stroeve et al., 2014a) evaluated SIT from CMIP5, which contains a large number of models each one with different climate sensitivity and amplitude of feedback mechanisms leading to a very different Arctic Amplification (e.g., Andrews et al., 2012). The studies suggest that uncertainties due to model biases as well as internal variability need to be considered in order to realistically represent Arctic SIT. Here, we use a single climate

model (the CESM), but one that has been widely used in climate studies. By averaging over multiple ensemble members, we can largely eliminate internal variability. Recent studies have assessed SIE trends and SIC variability in LENS and show strong internal variability among ensemble members (e.g., Barnhart et al., 2015; Swart et al., 2015; Yang and Magnusdottir, 2018). In this study, we evaluate the patterns of SIT variability during the satellite period and 20th century using PIOMAS and LENS, respectively. We also consider future projections of SIT in LENS. It is the first study to comprehensively evaluate SIT variability in LENS.

2.3 Methods

We compare submarine, satellite products (ICESat-J and CryoSat-2), and PIOMAS on 100 km EASE grids, masked by their respective spatial coverage domain. CryoSat-2 covers the entire Arctic basin. In contrast, the ICESat-J SIT data are not available over the Atlantic sector of the Arctic Ocean, including portions of the Barents and Kara Seas. The ULS submarine data are limited in coverage to the region just north of Greenland.

We compare SIT between the observational products and PIOMAS without considering SIC (therefore, SIT is averaged over the entire grid cell). However, for comparing the two model-produced SIT data sets (PIOMAS and LENS), we use the effective SIT (h_{eff} = SIT $\cdot$ SIC [0,1]). The difference between these two methods of assessing SIT is largest during fall and mostly confined to the outer marginal seas (generally < 1 m).

Average SIT is estimated by area weighting SIT for grid cells with a thickness of at least 0.15 m north of 65°N. The 0.15 m mask excludes grid cells with largely open sea water. Thus, total SIV in LENS and PIOMAS is computed by:

$$\text{SIV} = \sum_i h_{eff_i} a_i \tag{2.1}$$

where, h_{eff} is the effective thickness and a_i is the area of the grid cell. All sea ice calculation estimates are on monthly time scales.

Data comparing PIOMAS and LENS are regridded onto a common 1° latitude x 1° longitude spacing using a piecewise linear interpolation method. We apply EOF analysis to monthly linearly detrended SIT fields in LENS and PIOMAS using the Dawson (2016) Python package. EOF analysis in LENS is performed by appending all of the ensemble members together. Before computing EOFs, the SIT fields are weighted by the square root of the cosine of their latitude to account for converging meridians towards the pole. To examine regional SIT variability, we further divide the Arctic Ocean into six sub-domains chosen by similar mean spatial SIT (north of 65°N). These areas are shown in Figure A.1 and represent the following: Central Arctic Basin (north of 85°N), northern Canadian Arctic Archipelago and Greenland coast, Beaufort and Chukchi Seas, East Siberian Sea, Laptev Sea, Barents and Kara Seas. Areas in the outer marginal seas such as Bering Sea, Baffin Bay, Sea of Okhotsk and the southern Canadian Arctic Archipelago are excluded as sea-ice cover is generally only present in winter.

2.4 Results

2.4.1 PIOMAS and observational sea-ice thickness data

In a similar method to the SIE visualizations in Parkinson and DiGirolamo (2016), Figure 2.1 uses a color gradient to show PIOMAS SIV anomalies over the 1979 to 2015 period, using 1981-2010 as climatology. The overall volume rankings from highest (rank of 37) to lowest (rank of 1) are also displayed for each month in the time series. For instance, a ranking of "1" is the lowest total SIV for that respective month over the time series. While there is considerable interannual variability, there is a net loss of SIV in every month of the year during the satellite era. More recently, since 2007, SIV anomalies are greatest in summer (JJA). This is in contrast to the recent greatest total SIE anomalies (and largest variability) in September, which is the climatological end of the melt season (Serreze and Stroeve, 2015; Serreze et al., 2016). A study by Bushuk et al. (2016) found that this enhancement of the summertime anomaly is driven by a positive feedback between SIT and ice-albedo and is affected by melt pond formation, snowfall, and SIC.

To compare the depiction of SIT distributions in the various datasets, we show violin plots of their March SIT in Figure 2.2. Violin plots are useful in visualizing a kernel density estimate to show the shape of the distribution on each side of the center axes. Each observational product is compared with PIOMAS over the relevant period (shown in brackets on the left-hand side) and spatial domain (shown in the right-hand column). The means of the distributions are shown by black bold ticks. The difference in mean SIT between the various observational products and PIOMAS is in all cases less than 0.4 m. A larger range in ICESat-J's March SIT values is found. However, this difference may in part be due to an overestimation of SIT near Greenland from ICESat-J due to the choice of sea-ice density (Zygmuntowska et al., 2014). Greater variability is found in both submarine and ICESat-J estimates with stan-

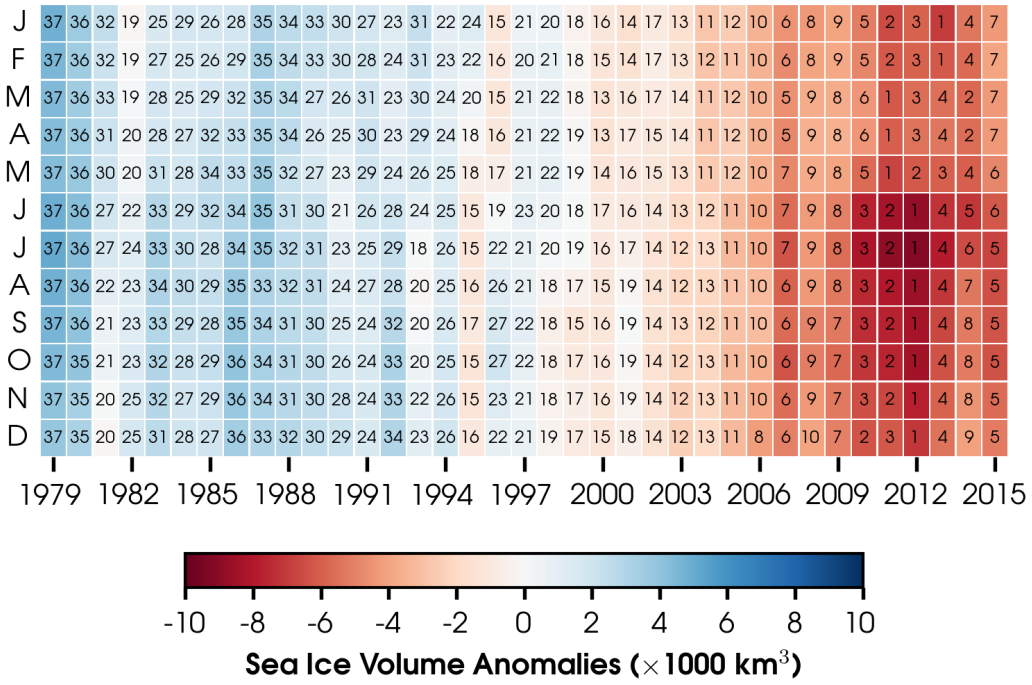

Figure 2.1: PIOMAS Arctic sea-ice volume anomalies (color gradient) for each month over the period from 1979 to 2015. The 37 years are ranked (black numbers) for each month by total volume; therefore, "1" identifies the lowest sea-ice volume in the 37-year record for each individual month.

dard deviations of 0.96 m and 0.91 m when compared with PIOMAS of 0.61 m and 0.64 m, respectively. Standard deviations are similar in CryoSat-2 and PIOMAS and correspond to 0.71 m and 0.70 m. Overall, the closest agreement is found between CryoSat-2 and PIOMAS.

Comparing spatial differences between gridded SIT in the various observations suggests PIOMAS consistently underestimates in regions of thicker ice and overestimates in regions of thinner ice. This is particularly noticeable in the comparison of gridded submarine and ICESat-J with PIOMAS SIT over the region of climatologically thickest ice north of Greenland and along the coastline in the Greenland Sea (not shown). These results are consistent

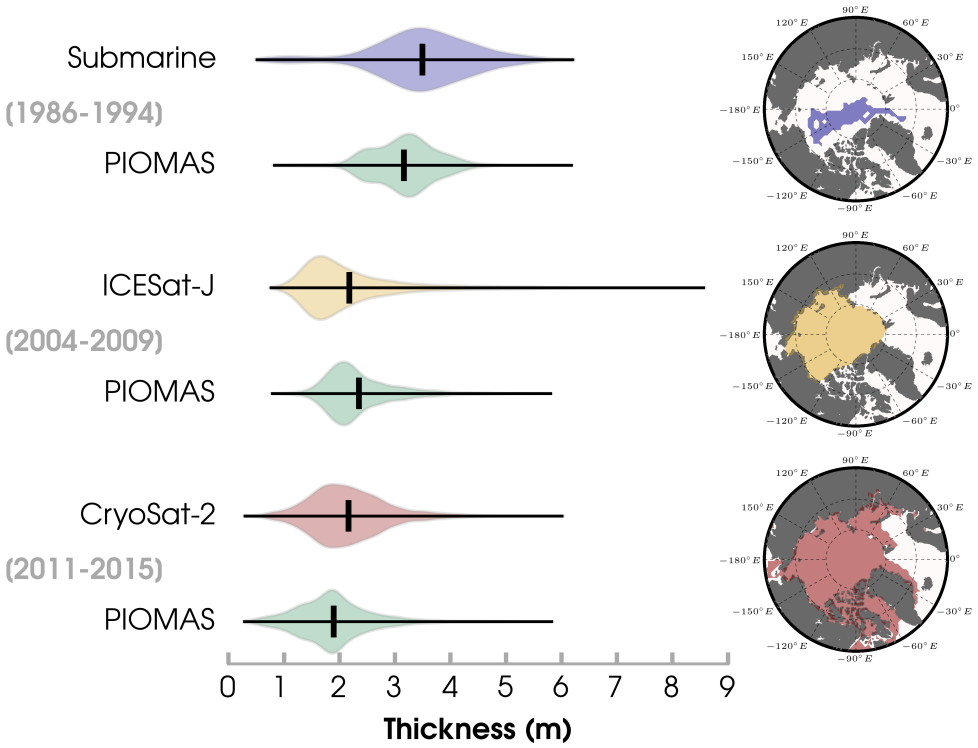

Figure 2.2: Violin plots showing distributions (left column) of March sea-ice thickness from PIOMAS and three observational datasets, each plotted over the years of operation of the observation platform. On left from top: PIOMAS and submarine (1986-1994); middle: PIOMAS and ICESat-J (2004-2009); bottom: PIOMAS and CryoSat-2 (2011-2015). The domain that the three different observation platforms cover is shown on the right. Data are interpolated onto a common 100 km EASE-Grid. The mean is indicated by a bold black line in each violin plot.

with earlier studies (e.g., Schweiger et al., 2011; Laxon et al., 2013; Stroeve et al., 2014a; Wang et al., 2016).

PIOMAS produces a similar SIT spatial distribution compared with submarine and satellite data. While there are small regional differences as previously noted, all SIT comparisons show reasonable agreement over space and time and support the use of a PIOMAS climatological record. Henceforth, we will use PIOMAS SIT for our analysis. Additional information

about PIOMAS SIT uncertainties and biases are detailed in Schweiger et al. (2011).

We calculated linear (least squares) SIT trends over overlapping 10-year periods from 1980 to 2015 (not shown). Shorter periods over the PIOMAS time series reveal large variability in SIT trends, particularly across the Beaufort, Chukchi, and East Siberian Seas. However, over the entire time series (1979-2015), decadal trends shown by season in Figure 2.3 indicate an extensive thinning of sea ice across the Arctic Ocean basin in all seasons and especially north of the Canadian Arctic Archipelago and in the East Siberian Sea.

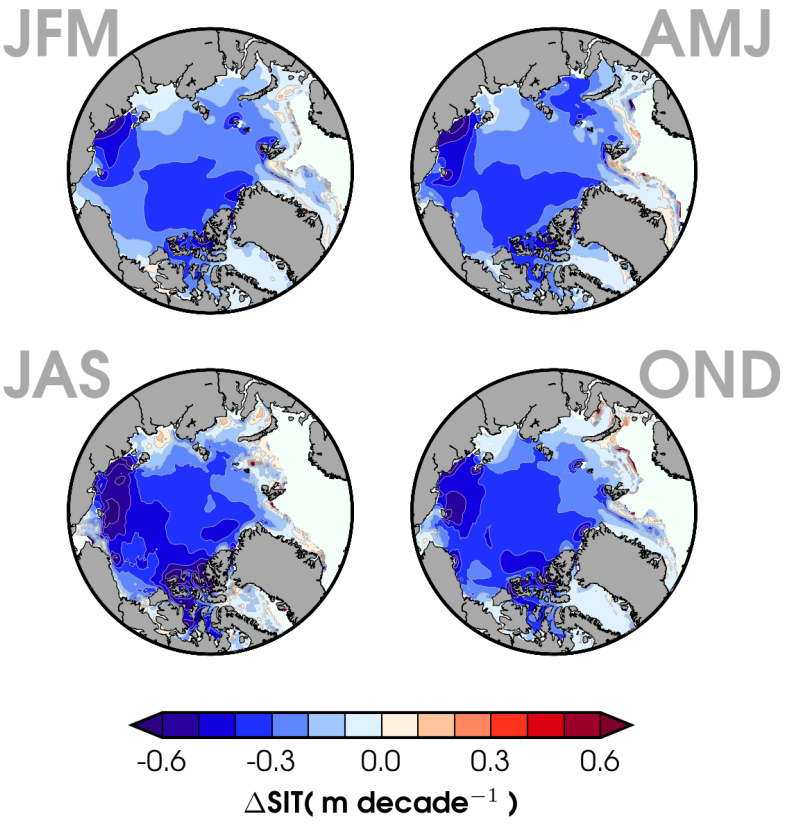

Figure 2.3: Linear trends in PIOMAS sea-ice thickness (SIT) from 1979 to 2015 in m decade^{-1} calculated over each season. Contour intervals are 0.1 m decade^{-1}.

We evaluate interannual variability of SIT in PIOMAS, as in Blanchard-Wrigglesworth and Bitz (2014), by calculating standard deviation of linearly detrended monthly thickness, here for each season, shown in Figure 2.4. The greatest variability is found along the coastlines, especially north of the Canadian Arctic Archipelago and in the East Siberian Sea, during all seasons. Areas of thicker ice (such as north of Greenland) often have higher variability. The lowest variability in all seasons is found in the central Arctic basin.

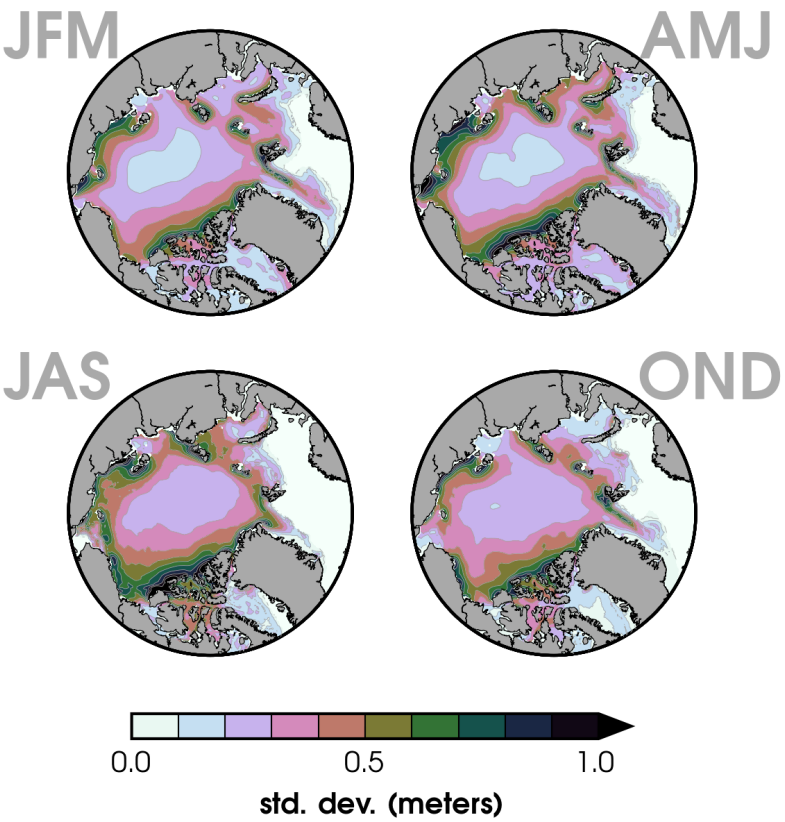

Figure 2.4: Standard deviations (m) of sea-ice thickness averaged for each season. The monthly sea-ice thickness at each grid point is first linearly detrended before calculating the standard deviation. Contour intervals are 0.1 m.

2.4.2 Regional sea-ice thickness variability (1920-2015)

We use the CESM large ensemble (LENS) to evaluate regional SIT variability over historical (1920-2005) and future (RCP8.5; 2006-2080) periods (subsection 2.4.3). Previous studies have shown that LENS realistically reproduces the interannual cycle and internal variability of Arctic SIC (Barnhart et al., 2015; Swart et al., 2015; Jahn et al., 2016; Yang and Magnusdottir, 2018). Our analysis is focused on SIT variability in LENS, which has not been previously addressed. In this subsection, we combine a few years of projected LENS (specifically 2006-15) with the part of the historical period that overlaps with PIOMAS (1979-2015). Figure 5 compares the SIT seasonal cycle from PIOMAS with LENS over the 1979-2015 time period. The ensemble-mean of LENS overestimates SIT by 0.5 m on average in the annual mean. All of the LENS members closely reproduce the PIOMAS SIT seasonal cycle with only minor differences in the timing of the minimum thickness in late fall. Ensemble spread is greatest in September at approximately 0.48 m between the maximum and minimum ensemble members and decreases to 0.32 m in May (near the SIT climatological maximum). The difference in the spatial distribution of the annual mean SIT between the ensemble mean of LENS and PIOMAS (1979-2015) is shown on the right-hand side of Figure 2.5. The LENS mean is thicker by more than 1 m along coastal Greenland, the northern Canadian Arctic Archipelago, and near the New Siberian Islands in the East Siberian Sea. These areas are located near the greatest variability expressed by PIOMAS SIT as seen in Figure 2.4 and in areas where PIOMAS consistently underestimates thick ice along coastal Greenland.

In Figure A.2 we assess our six defined sea-ice regions (Figure A.1) for comparisons between LENS and PIOMAS. Comparing the differences between the historical LENS mean and PIOMAS in September from 1979 to 2015, we find close agreement for average SIT in the Central Arctic Basin, the Barents-Kara Seas, and the Laptev Sea (Figure A.2). The largest

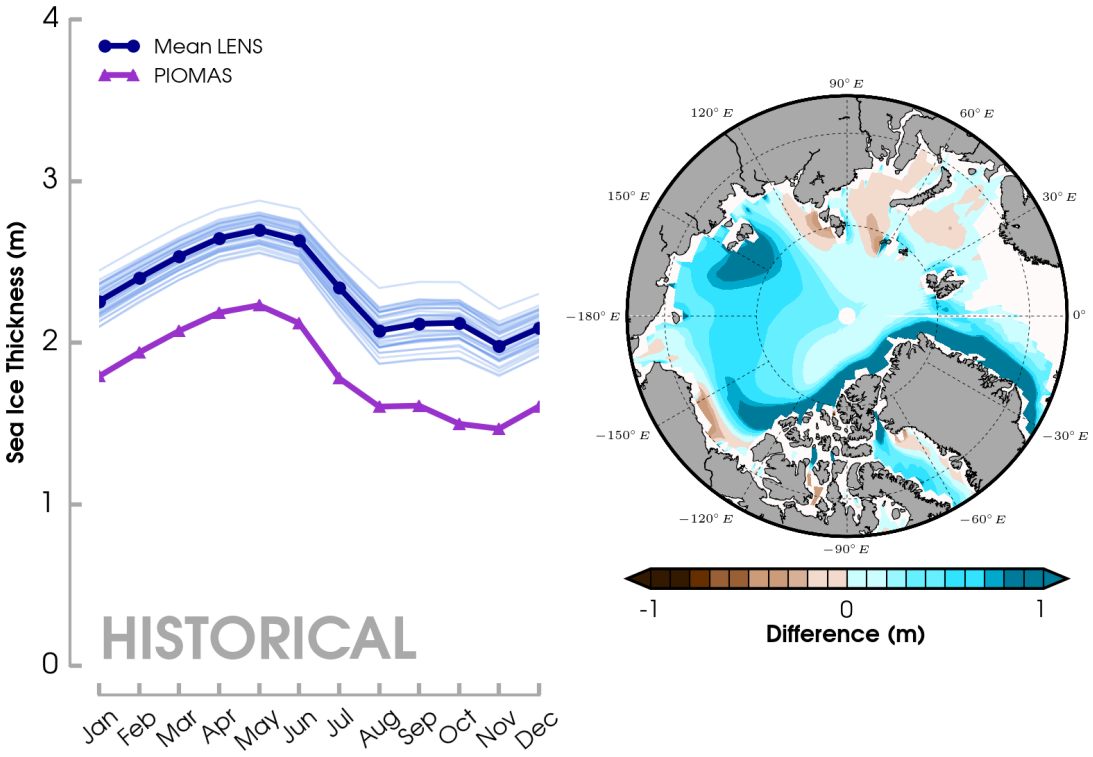

Figure 2.5: Seasonal cycle of sea-ice thickness (north of 65°N) calculated for PIOMAS and LENS (left). All forty ensemble members are used for LENS, but only over the period overlapping with PIOMAS (1979-2015). Each LENS member is denoted by a light blue line and the ensemble mean in dark blue. The difference in mean annual SIT (right) between the ensemble mean of LENS and PIOMAS. Contour intervals are 0.1 m.

differences are north of Greenland (> 1 m), the Beaufort and Chukchi Seas, and in the East Siberian Sea, where the ensemble mean has thicker sea ice than PIOMAS. March differences between the LENS mean and PIOMAS (not shown) are approximately the same magnitude as in September for all regions.

To get a quick overview of the spatial character of September SIT in LENS and PIOMAS, Figure 2.6 represents a composite, first from LENS over the historical period split into two equal time periods shown in Figure 2.6a-b, for 1920-62 and 1963-2005. We also composited September SIT in LENS so that it overlapped with the PIOMAS time period, 1980-2015.

These are shown in Figure 2.6c (1980-97) and Figure 2.6g (1998-2015) and should be compared with the equivalent field from PIOMAS shown in Figure 2.6d and 6h. The LENS composite of projected SIT (shown in Figure 2.6e-f) will be discussed in the next subsection (4c). There is little change in the spatial distribution of SIT in the historical LENS until the late 1990s. From then on there is a thinning of sea ice across much of the central Arctic basin. A comparison of the $\text{LENS}_{\text{PIOMAS}}$ composites and PIOMAS shows that the ensemble mean has thicker ice extending from the central Arctic basin into the East Siberian and Laptev Seas (Figure 2.6, two right-hand columns). Further, $\text{LENS}_{\text{PIOMAS}}$ has an area of thicker sea ice extending along the east coast of Greenland from the Fram Strait. These regions of thicker sea ice in $\text{LENS}_{\text{PIOMAS}}$ are present in both periods (1980-1997 and 1998-2015). In contrast, PIOMAS only distributes its region of thicker ice (> 3 m) close to Greenland and the northern Canadian Arctic Archipelago coast. The latter half of the PIOMAS time series is consistent with a general thinning over all sea-ice covered areas.

To investigate regions of SIT variability in PIOMAS and the historical LENS, we use EOF analysis to determine the primary modes of variability. The first leading mode in the historical (1920-2005) LENS (EOF1; representing 41% of the variance) is depicted in Figure 2.7 and has opposite-sign centers of action near the New Siberian Islands and close to Svalbard. This pattern corresponds to the Northern Annual Mode (NAM) in the atmosphere, which is the first mode of variability of the atmospheric circulation in the Northern Hemisphere extratropics, including the Arctic, and where a positive polarity drives sea ice away from the coast of Siberia toward the Fram Strait and leads to an increase in Arctic sea-ice divergence (Rigor et al., 2002). The second leading mode in LENS (EOF2; representing 14% of the variance) again has two opposite-sign centers of action: East Siberian Sea and Greenland Sea (Fram Strait). Thus, both EOFs show a dipole in sea-ice thickness between the eastern and western Arctic, which underscores the importance of this pattern.

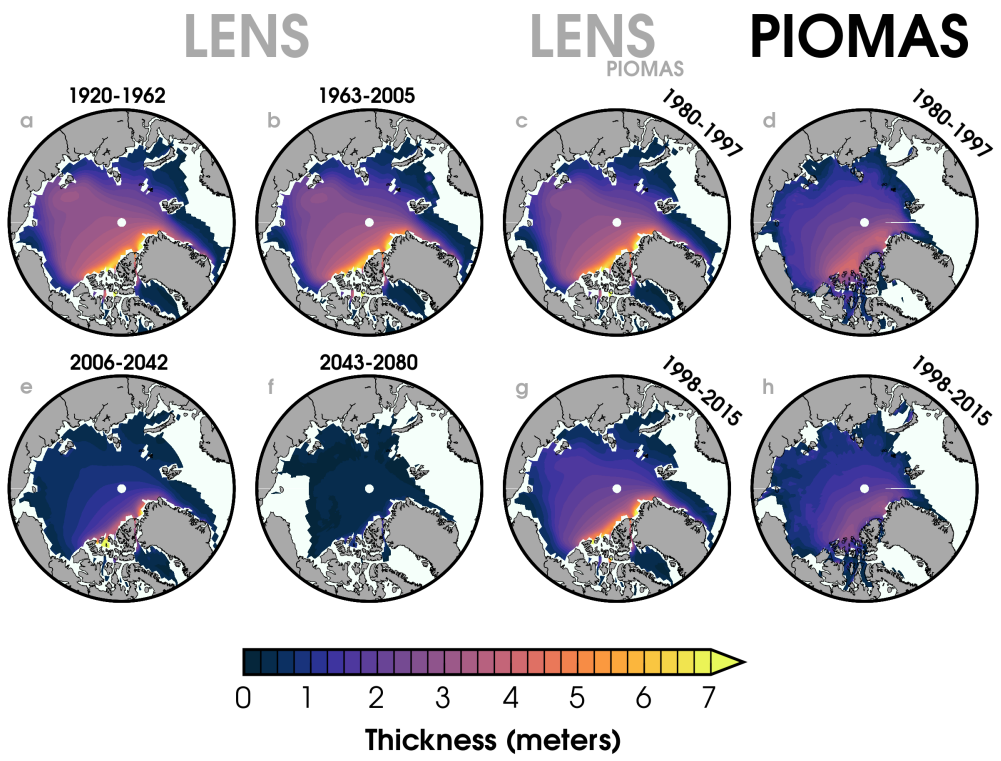

Figure 2.6: September sea-ice thickness composites from the historical and future LENS ensemble average and from PIOMAS (right column). The LENS ensemble mean (1920-2080) is composited over four different equal-length time periods shown in the two left-hand columns (1920-1962, 1963-2005, 2006-2042, 2043-2080). Furthermore, for comparison with PIOMAS, the third column shows the LENS ensemble member over 1980-1997 (top) and 1998-2015 (bottom).

For consistency with the PIOMAS temporal record, we compute EOFs from 1979 through 2015 in LENS, shown in Figure 2.7 (middle column). The first leading mode (EOF1; representing 26% of the variance) reflects the dipole structure of two opposite-sign centers of action, in the East Siberian to Laptev Seas and near the Fram Strait. The second leading mode in LENS from 1979 to 2015 (EOF2; representing 17% of the variance) reflects a slightly more homogeneous structure stretching from over the central Arctic to near Svalbard. We also see a decrease in the percentage variance explained by the EOF1 composite in the 1979 to 2015 LENS.

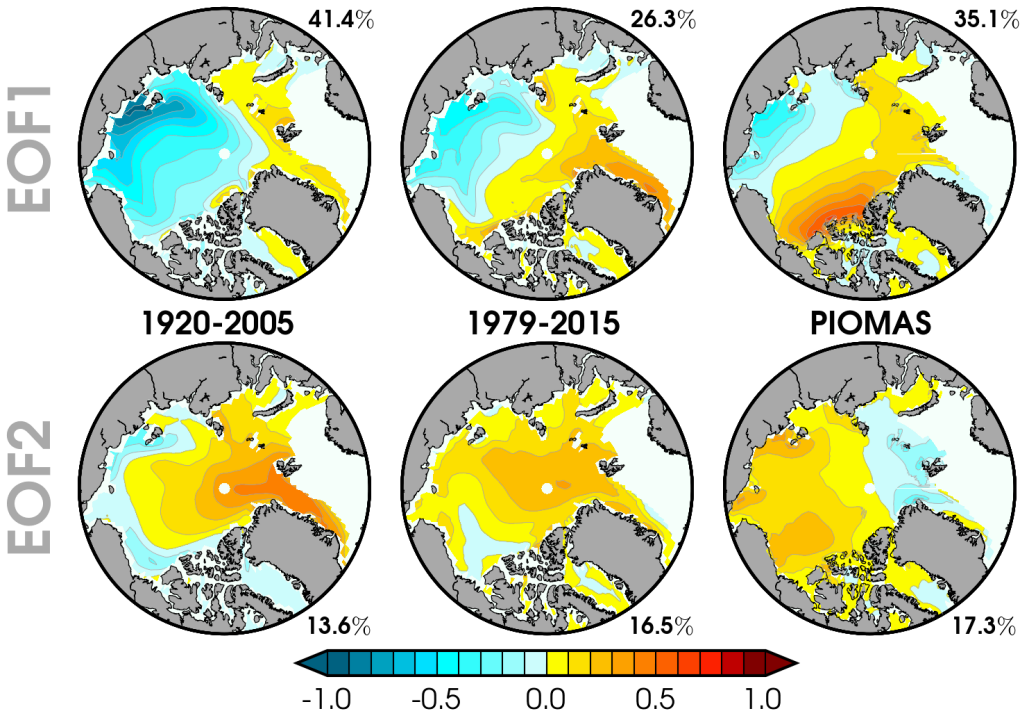

Figure 2.7: Spatial patterns of the first two leading EOF modes (top; EOF1, bottom; EOF2) calculated from all monthly sea-ice thickness fields in the LENS historical simulations (left; 1920-2005), LENS overlapping with PIOMAS (middle; 1979-2015) and PIOMAS (right; 1979-2015). Monthly sea-ice thickness points are detrended (linearly) before computing the EOF analysis. The percentage of explained variance is given in the upper/lower right-hand corner for each of the EOF maps.

The first leading mode in PIOMAS (EOF1; representing 35% of the variance) shares some common features with the east-west Arctic anomaly pattern (Zhang et al., 2000). The east-west Arctic anomaly pattern is a sea-ice mass dipole anomaly between the Beaufort Sea and the East Siberian and Laptev Seas region. This dipole is enhanced during strongly positive NAM periods and acts to increase Fram export and hence, leaving significantly reduced thickness in the eastern Arctic (Zhang et al., 2000). We see again the opposite centers of action from near the East Siberian Sea region to the Atlantic sector. PIOMAS's second leading mode (EOF2; representing 17% of the variance) is more homogenous, similar to LENS (1979-2015) EOF2, but shows a larger maximum anomaly from the Beaufort Sea to the New

Siberian Islands region.

We find that LENS captures similar patterns of spatial variability as PIOMAS shown in Figure 2.4. The largest differences reside in the Beaufort Sea and Canadian Arctic Archipelago regions where PIOMAS' both EOF1 and EOF2 patterns feature a maximum anomaly, which is not present in LENS. The PIOMAS EOF1 spatial pattern is similarly captured by the interannual variability in Figure 2.4, but extends farther from the immediate coastlines in the East Siberian and Beaufort Seas. We show late summer (JAS) SIT variability in Figure 2.8 characterized by the standard deviation of LENS detrended SIT fields. In comparison to PIOMAS in Figure 2.4, we see greater variability in the East Siberian Sea and less so north of the Canadian Arctic Archipelago, but the overall spatial patterns remain similar. A decrease in LENS SIT variability is evident with time as sea ice becomes thinner over the Arctic Ocean. By the 2006-2042 composite in Figure 2.8, the greatest SIT variability is confined to the coastlines of Greenland and the Canadian Arctic Archipelago.

2.4.3 LENS future projections of sea-ice thickness (2006-2080)

Some characteristics of SIT in LENS projections were highlighted in Figure 2.6e-f with substantially thinner ice across most of the Arctic Ocean as well as the corresponding future SIT standard deviations (shown in Figure 2.8) and SIT EOFs (shown in Figure 2.7). During the mid-2020s, September ice is generally less than 1 m, except for a small area north of Greenland and the Canadian Arctic Archipelago. By the end of the 21^{st} century, September is less than 0.5 in all regions. In Figure 2.9 we show the basin-wide average SIT in LENS (all ensemble members in grey, ensemble mean in bold) over the historical period and projected to 2080 during the months of September (climatological minimum SIE) and March (climato-

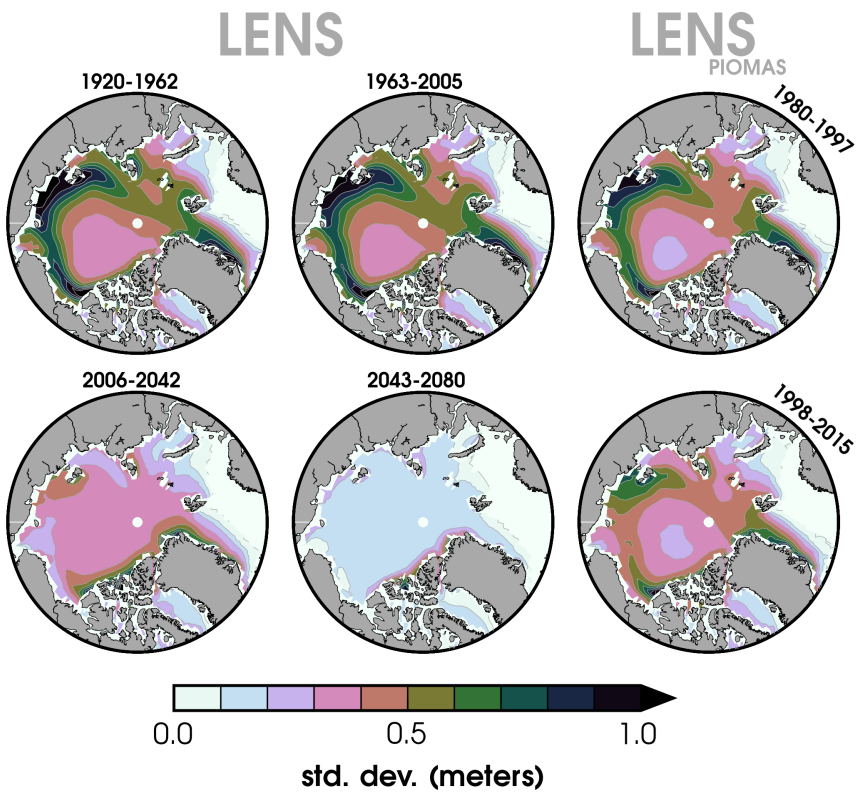

Figure 2.8: Standard deviations (m) of LENS sea-ice thickness averaged for July through September (JAS). The monthly sea-ice thickness at each grid point is first linearly detrended. LENS composites are averaged over two equal periods per historical (1920-1962 and 1963-2005) simulation and future (2006-2042 and 2043-2080) projections along with a closer comparison to PIOMAS over the period they share in common (1980-1997 and 1998-2015). Contour intervals are 0.1 m.

logical maximum SIE). Substantial spread is found in the historical simulations in September with an average of 1.1 m between the minimum and maximum SIT ensemble members (Figure A.3). There are also several outliers at more than 0.75 m from the mean. The ensemble spread decreases to approximately 0.5 m by 2080 between the minimum and maximum ensemble members. Moreover, spread decreases as SIT thins over the Arctic Ocean, which is partly due to the overall decrease in the mean SIT. As already discussed, areas of thin ice have reduced SIT variability. PIOMAS average SIT is outside the LENS envelope and approximately 0.5 m below the ensemble mean. Nevertheless, the rate of decline is similarly captured by the ensemble mean as in PIOMAS. Ensemble spread is smaller for March

than September at an average of 0.8 m for the historical simulations and decreases to 0.4 m for the future projections (Figure A.3). There is minimal interannual variability in March after 2040. This timing is also consistent with the appearances of the first "ice-free" SIE summers in LENS; nevertheless, a large spread in this timing still remains (Jahn et al., 2016).

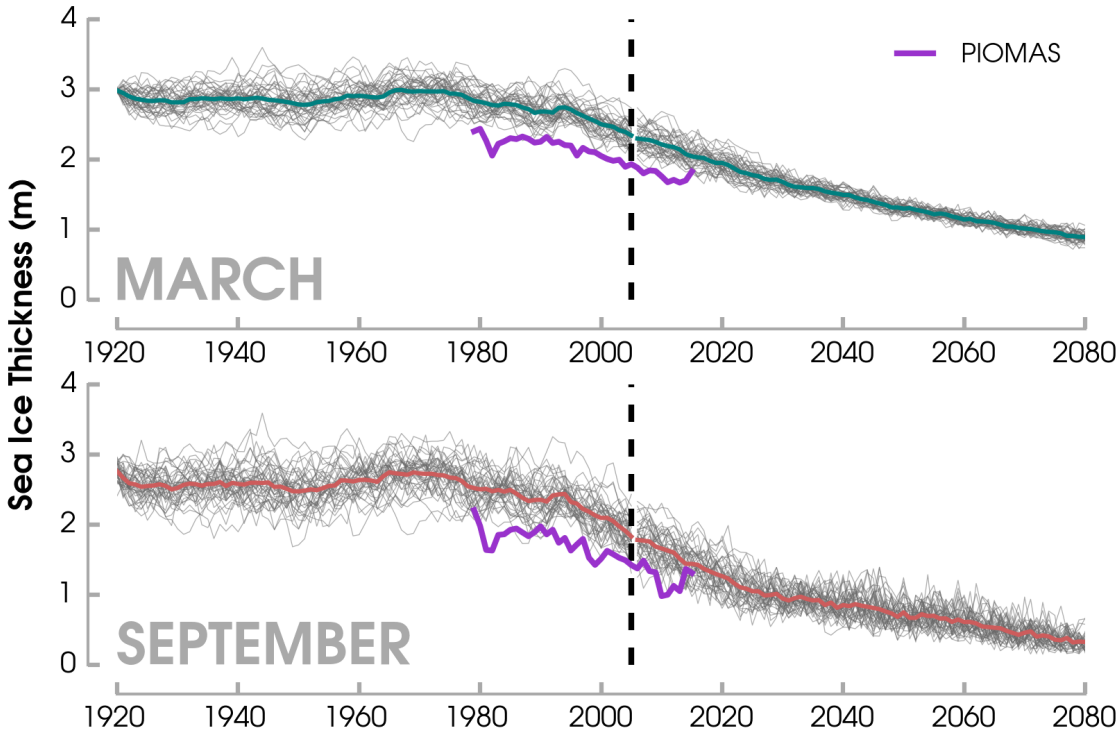

Figure 2.9: Time series of March (upper) and September (lower) sea-ice thickness (north of 65°N) for LENS and PIOMAS (purple). Each LENS member indicated (gray) in addition to their ensemble mean (blue/red lines). The dashed vertical line separates the historical from the future LENS simulations.

A comparison of SIV (for the months September and March) between PIOMAS and LENS shows that PIOMAS is inherently lower than the LENS ensemble mean in both months. LENS also has greater spread between ensemble members in September than March (not shown).

Further, Figure A.4 shows that this internal variability contributes to a range between the 5th and 95th percentile of 2040 to 2049 for the timing of the first mean-September SIV dropping below 1000 km^3 among ensemble members. In Figure 2.10, we show the September, area-averaged SIT time series for each sea-ice zone (Figure A.1) through 2080. All regions fall below 0.5 m in thickness during the future LENS period, but the timing of this event varies considerably. It occurs as early as the 2020s in the ensemble mean for the Barents-Kara Seas, Laptev Sea, and East Siberian Sea. Substantial thinning also occurs in the Central Arctic Basin. For the Greenland area, the mean September SIT remains greater than 0.5 m for the better part of the period or until the 2060s. A corresponding time series plot for March (not shown) does not indicate any regions in the ensemble mean falling below 0.5 m average thickness through 2080. If we examine the average timing of when the first September falls below

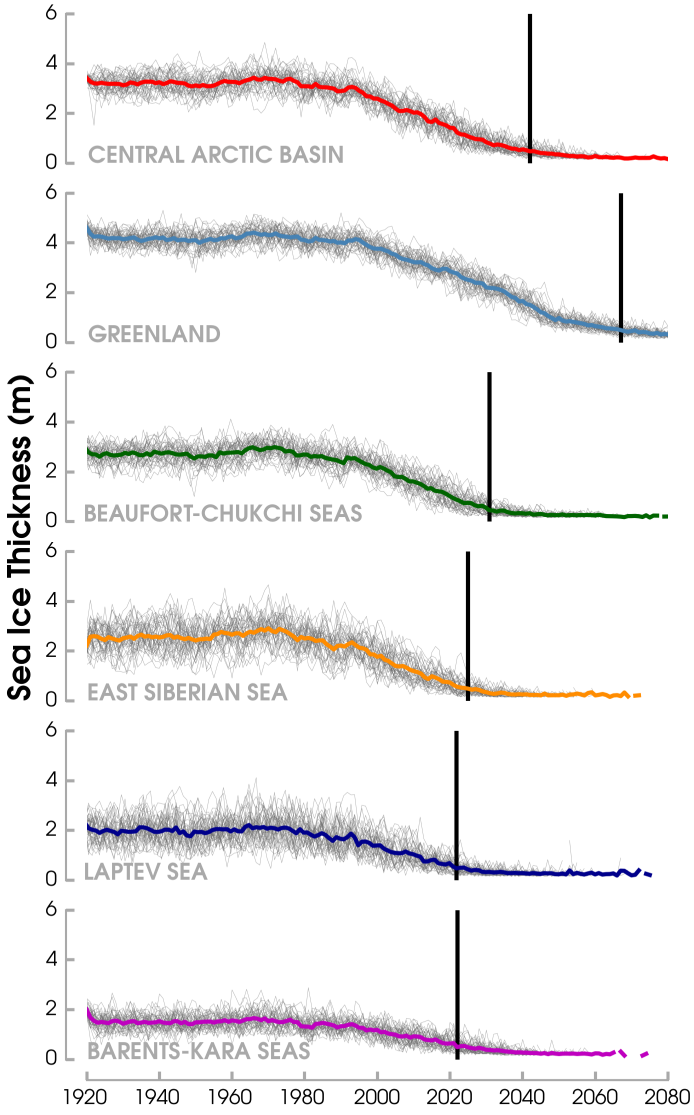

Figure 2.10: Regional September sea-ice thickness through the historical and future LENS time series (1920-2080) for all ensemble members (gray lines) and the ensemble means (bolded colored lines). The first instance of the average sea-ice thickness at or below 0.5 m is shown by a vertical black line.

0.5 m SIT for each ensemble member, this occurs earlier than for the LENS ensemble mean and is shown in Figure 2.11 for the different regions. The difference from the ensemble mean is especially pronounced in the regions of thinner ice, such as the Laptev and Barents-Kara Seas, where the 5-95th percentile ensemble years range from 2002-2022 and 1999-2021, respectively.

While 21st century sea ice thins substantially in all seasons, a large sea-ice cover continues to reform during the cold season. A region of perennially thick ice north of Greenland also remains. We note that there is a large spread between ensemble members of SIT greater than 1 m in all regions through at least 2020 as seen in Figure 2.10. The largest spread is found in the East Siberian and Laptev Seas. Consequently, the variance begins to decrease as average sea ice thins over the entire Arctic basin. This implies reduced uncertainty from future SIT internal variability.

Linear SIT trends over the same observational period (1979-2015) for LENS and PIOMAS (not shown) reveal close agreement in the rate of sea-ice thinning. Comparing future LENS SIT linear trends (2006-2080) with the previous PIOMAS record (1979-2015) shows little to no change in the rate of sea-ice thinning in winter and spring and little spread among ensemble members as seen in Figure 2.12 (JFM, AMJ). The rate of thinning increases slightly in summer (JAS) and fall (OND) as seen by the increased spacing between the two vertical lines, the black one representing the LENS ensemble average and the purple on representing the PIOMAS record. The spread between ensemble members is largest in JAS and OND at approximately 0.25 m decade^{-1}. Evidence of regional variations in SIT have been well documented since the late 1950s (e.g., Rothrock et al., 1999; Rothrock and Zhang, 2005; Rothrock et al., 2008) through submarine sea-ice draft data and modeling experiments. In LENS the rate of future thinning is similar in all six areas; however, sea ice loss accelerates near the climatologically thicker ice near the Canadian Arctic Archipelago and Greenland

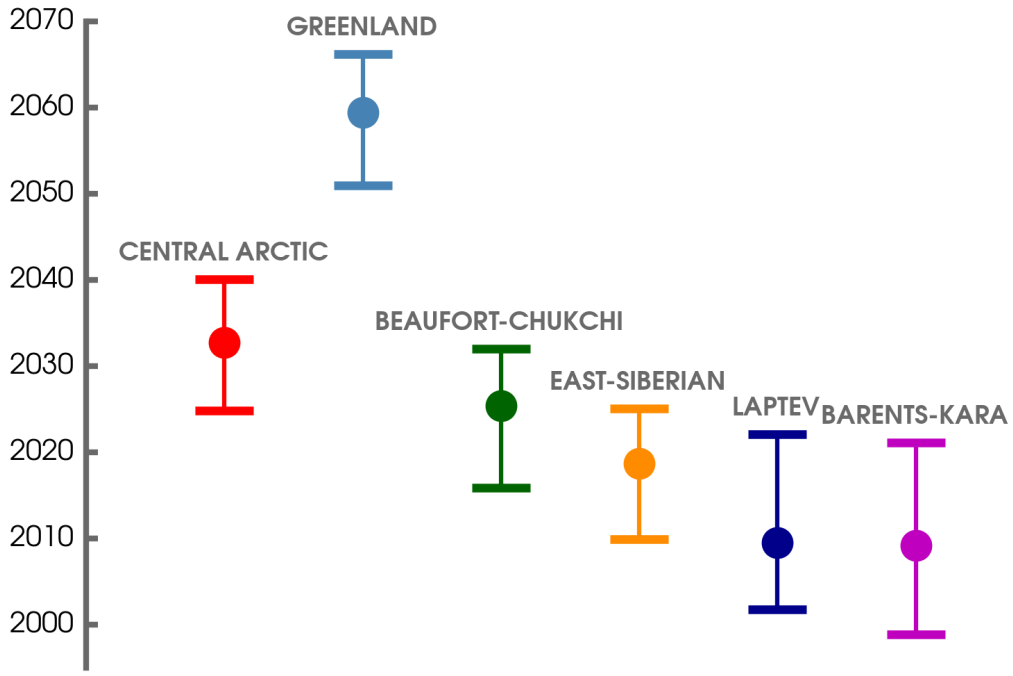

Figure 2.11: Regional timing of the first September sea-ice thickness to fall below 0.5 m averaged by each ensemble member's year (center point). The 5th-95th percentile years are visualized by the error bars.

(not shown). This is consistent with Bitz and Roe (2004) showing that areas of thicker ice have the greatest thinning.

2.5 Summary and conclusions

We use PIOMAS and LENS to assess the historical and future variability of Arctic SIT. To validate that we can use PIOMAS as a reanalysis data set, we compare PIOMAS with SIT observations from submarine data and satellites. The key results of this study are summarized below.

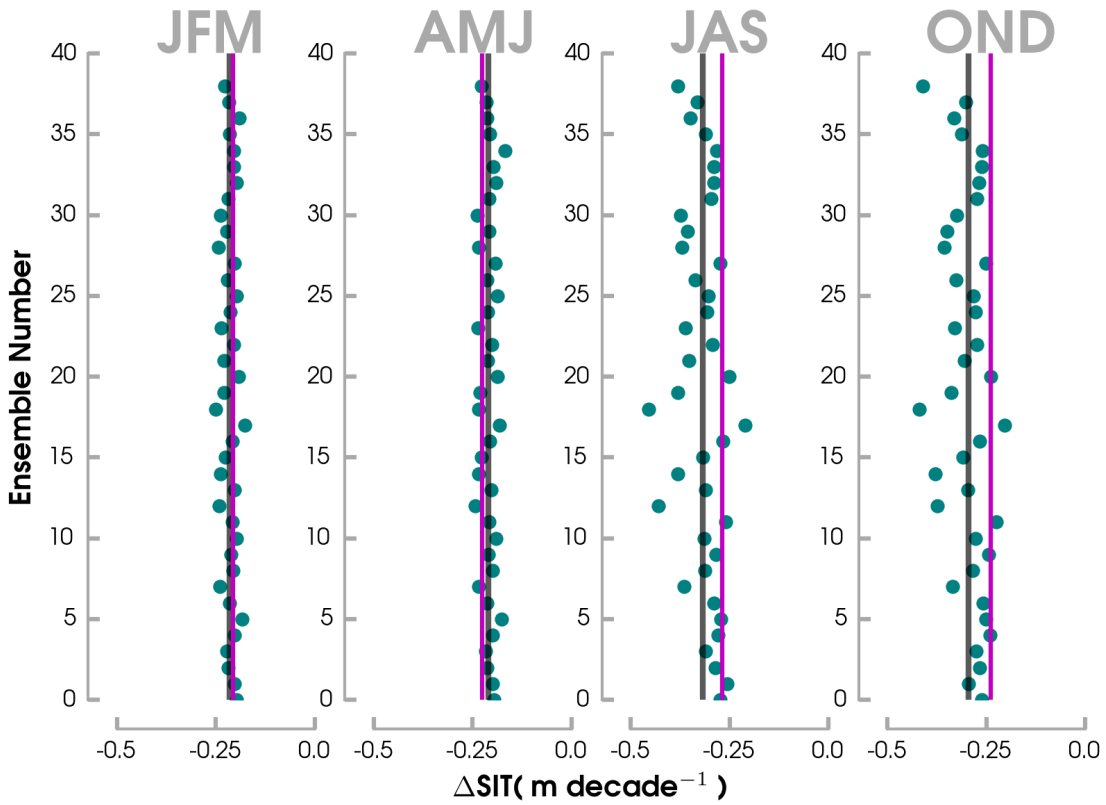

Figure 2.12: Seasonal decadal trends in average sea-ice thickness (SIT) averaged through the future LENS period (2006-2080) from each ensemble member (blue points). Ensemble mean decadal trend (2006-2080) shown by a vertical black line. PIOMAS SIT trends for the 1979 to 2015 period shown by a purple vertical line.

1. PIOMAS realistically reproduces the spatial distribution of SIT when compared with satellite and submarine observations. We find long-term losses in Arctic SIT and SIV during all months of the year in the PIOMAS record (1979-2015) with the largest trends during the summer months (JAS). We find considerable spatial variability in seasonal PIOMAS SIT over the Beaufort, Chukchi, and East Siberian Seas and along coastal areas.

2. We show that LENS compares well with PIOMAS both in the regional distribution of mean SIT and in revealing similar patterns of spatial variability. The largest differences are in areas north of the Canadian Arctic Archipelago and coastal Greenland where

LENS simulates thicker sea ice. PIOMAS underestimates SIT in this region when compared with satellite and submarine observations. There is a documented negative bias in PIOMAS (Schweiger et al., 2011), and this likely contributes to the larger total SIV in LENS than PIOMAS. Compared with PIOMAS, the LENS annual mean also places significantly thicker sea ice near the New Siberian Islands in the East Siberian Sea.

The first EOF of the historical LENS (1920-2005) places a center of action over the East Siberian Sea with same-signed anomalies stretching over the entire Arctic. Opposite anomalies are found over the Atlantic side of the Arctic. The area of the East Siberian Sea has the greatest thinning in recent decades as obtained from PIOMAS. Using a similar model as PIOMAS, Rothrock and Zhang (2005) also find that the East Siberian Sea has the greatest loss in SIT through 1999. When considering only the time period 1979-2015 (the time of the PIOMAS record), the first mode of SIT variability in LENS shows a shrunken area around the East Siberian Sea center of action and the area of the opposite polarity now reaches deep into the Arctic including north of Greenland. It is more similar to the PIOMAS first mode of variability, which has the primary center of action north of Greenland with an area of opposite signed anomalies that is smaller in extent centered in the East Siberian Sea.

3. All LENS members indicate a long-term decrease in SIT across the Arctic Ocean through the end of the 21st century. Both September and March SIT in the entire LENS time series (1920-2080) show significant spread between individual ensemble members in the Beaufort, East Siberian, and Laptev Seas of approximately 2 m through 2020. The large ensemble spread early on indicates that internal variability has an important role in determining regional SIT during all months. By the middle of the 21st century and on, SIT becomes less sensitive to interannual changes in most regions except for areas of thicker ice near Greenland. An area of perennially thick sea ice remains north

of Greenland during all months of the year, but it significantly thins (especially in September) by the mid-21st century. Average September SIT in all regions eventually falls below 0.5 m during the 21st century. However, the timing of this event varies by more than a decade among ensemble members. We also show that the timing of the first September SIT below 0.5 m occurs substantially earlier than the timing of that event for the ensemble mean in the outer marginal seas, but year-to-year variability remains. Recent summer sea-ice conditions have already shown this to be the case, for instance in the Barents-Kara Seas. Even in the area of climatologically thick sea ice north of Greenland, the first September with SIT less than 0.5 m is reached on average by 2059±7 years. While future rates of declining SIT may temporarily slow or even pause as a result of this high internal variability and the resiliency of SIV (Tilling et al., 2015; Blanchard-Wrigglesworth and Bitz, 2014), future simulations from LENS indicate a continued loss of thicker, multi-year sea ice and a reduction in interannual variability

Our results are limited by any inherent bias in using the output of a coupled sea-ice-ocean model (in this case PIOMAS) as a SIT reanalysis data set, as well as from any model bias due to CESM1.1. While PIOMAS has the capability to assimilate SIC and SST, additional improvements to other similar coupled sea-ice ocean models have been made by assimilating SIT observations (e.g., Xie et al., 2016). More satellite and in situ observations are especially needed in the East Siberian and Beaufort Seas where there is substantial SIT variability.

A thinning sea-ice cover will bring challenges to future sea-ice prediction as the response of SIE to atmospheric circulation patterns may change (Holland and Stroeve, 2011). Further idealized experiments using realistic long-term SIT data are also needed to assess the influences of a thinning sea-ice cover on the local and large-scale atmospheric responses (Lang

et al., 2017), such as that on Arctic Amplification.

Acknowledgements

We acknowledge the CESM Large Ensemble Community Project and supercomputing resources provided by NCAR for making the CESM-LENS data available. Output from PIOMAS is available from the Polar Science Center at the University of Washington. Additional gridded observational sea-ice thickness products are available from the NSIDC. We thank three anonymous reviewers for their suggestions and comments. This work was supported by NSF grants AGS-1407360, AGS-1624038, and NRT-1633631.

Chapter 3

Contributions of ice thickness to the atmospheric response from projected Arctic sea-ice loss

As appears in:

Labe, Z.M., Y. Peings, and G. Magnusdottir (2018), Contributions of ice thickness to the atmospheric response from projected Arctic sea-ice loss, *Geophysical Research Letters*, 45(11), 5635-5642, doi :10.1029/2018GL078158.

Abstract

A large ensemble of simulations from a high-top atmospheric general circulation model (AGCM) are conducted to compare the atmospheric responses from loss of Arctic sea-ice thickness and sea-ice concentration. The response to projected sea-ice thickness loss indicates substantial surface warming over the Arctic Ocean and up to 1°C of cooling in Eurasia.

While the dynamic circulation response from sea-ice thickness loss is smaller in magnitude, it has a similar spatial anomaly pattern as that due to sea-ice concentration loss. This pattern resembles the negative phase of the Northern Annular Mode. The simulations reveal that sea-ice thickness loss enhances the thermodynamic and large-scale circulation response from sea ice anomalies. These results stress the importance of considering a realistic sea-ice thickness distribution in future AGCM sea ice perturbation experiments.

3.1 Introduction

Reconstructed observations of sea-ice thickness (SIT) in the central Arctic have shown a reduction of approximately 65% since the mid-1970s (Lindsay and Schweiger, 2015). This loss of Arctic SIT has also been accompanied by a loss of sea-ice concentration (SIC), and therefore total sea-ice extent (SIE) (Serreze and Stroeve, 2015). As the climate in the Arctic continues to dramatically change, it remains uncertain how this loss of sea ice will remotely impact weather and climate, such as in the mid-latitudes (e.g., Vihma, 2014; Barnes and Screen, 2015; Overland et al., 2016). To understand the physical mechanisms between sea ice loss and the mid-latitude circulation in the presence of internal variability and a limited (spatially and temporally) observational record, we turn to performing atmospheric general circulation model (AGCM) sensitivity experiments. Understanding how thinning sea ice may affect climate variability is limited by the fact that satellite observations of SIT are less than a decade long. While a few studies have evaluated the effect of changes in SIT on the atmosphere (e.g., Gerdes, 2006; Rinke et al., 2006; Krinner et al., 2009; Lang et al., 2017) or from a sudden loss of thickness (e.g., Nakamura et al., 2016b; Semmler et al., 2016b), we provide the first (to our knowledge) quantitative assessment of the relative atmospheric response to SIT loss, compared to SIC loss under projected late twenty-first century Arctic sea ice conditions.

To address contrasting signals found in previous AGCM sea ice studies, Screen et al. (2018a) suggest that the prescription of SIT boundary conditions may result in different atmospheric responses. Some model experiments have used a fixed SIT (usually 2-m) across the Arctic (e.g., Peings and Magnusdottir, 2014; Sun et al., 2015), whereas others have prescribed a more realistic seasonal cycle of SIT (e.g., Deser et al., 2010) or empirically derived SIT from SIC fields (e.g., Screen et al., 2015). Comparing the atmospheric responses to a parameterized SIT distribution or fixed SIT (3-m), Krinner et al. (2009) found a significant negative SLP response over Eurasia from SIT loss and a Northern Annular Mode (NAM)-like response in the 500 hPa geopotential height. Earlier studies have also demonstrated the importance of SIT on the surface air temperature response over the Arctic. Conducting regional climate model experiments to compare the effect of prescribing a realistic SIT distribution versus a fixed (2-m) SIT, Rinke et al. (2006) showed much stronger upward heat fluxes and warmer temperatures where ice is thinner in the outer marginal seas. On the contrary, they found slightly colder near-surface air temperatures over the central Arctic in response to the realistic SIT, which is thicker than 2-m. Similarly, using hindcast simulations over 50 years (1948-1998), Gerdes (2006) showed a significant role of SIT loss on surface air warming with a maximum of 3.5°C near the New Siberian Islands. Results from Lang et al. (2017) suggest that loss of SIT may be responsible for up to half of the recent temperature trends in the eastern Arctic and up to 37% of the observed total Arctic amplification. Quantitatively similar, Sun et al. (2017) found a more realistic warming over the Arctic when compared with reanalysis by prescribing SIT as 1-m (rather than 2-m) in their atmospheric model experiments.

Here we use a high-top AGCM forced with prescribed repeating seasonal cycles of SIT, SIC, and sea surface temperature (SST). We isolate the role of SIT in forcing the large-scale atmosphere and compare its response to an experiment forced by only SIC anomalies. We also conduct an experiment to assess the response from the combined changes in future SIT and

SIC. Using a model with a well-resolved stratosphere, we are interested in improving our understanding of the stratosphere-troposphere pathway that has been shown to be important in the negative NAM response found in other AGCM sea ice studies (e.g., Nakamura et al., 2016a; Kim et al., 2014). Further, we expand upon the results of Sun et al. (2015) by using a realistic SIT distribution in comparing the response from regional sea ice anomalies.

3.2 Experiment design

To isolate the role of SIT on the atmospheric circulation, we use the Whole Atmosphere Community Climate Model, version 4 (WACCM4; Marsh et al., 2013). WACCM4 is a high-top atmospheric general circulation model (AGCM) with 66 vertical levels extending into the thermosphere to 5.1×10^{-6} hPa and includes stratospheric interactive chemistry. In addition to parameterizations from the low-top CAM4 model, WACCM4 has incorporated an additional turbulent mountain stress parameterization (Richter et al., 2010) and thus has a realistic climatology of sudden stratospheric warming. In this study, we use WACCM4 with specified chemistry (Smith et al., 2014) and a horizontal resolution of 1.9° latitude by 2.5° longitude. Greenhouse gas and aerosol concentrations are set to present-day conditions (year 2000). To assess the relative contributions of SIC and SIT, we run experiments consisting of 100 ensemble members each from September through March as summarized in Table A.1. The first month is discarded from analysis. Ensemble members are branched from a 200-year control simulation (as used in Peings et al., 2017). The Quasi-Biennial Oscillation (QBO) is set to a 28-month cycle derived from observed radiosonde data. We prescribe annually repeating cycles of SST, SIC, and SIT taken from the fully coupled Community Earth System Model Large Ensemble project (CESM-LENS; Kay et al., 2015). Earlier studies have demonstrated that LENS sufficiently reproduces present sea ice trends and variability when

compared with observations (e.g., Jahn et al., 2016; Labe et al., 2018a). The mean from 40 ensemble members is used to represent the historical (H; 1976-2005) and future (F; 2051-2080) periods. The future period in LENS is simulated under a high-emissions scenario (RCP8.5) with substantial loss of sea ice in all months of the year.

For all five simulations, SST is prescribed with a repeating climatology from the 1976-2005 LENS mean, except for grid cells where their 2051-2080 SIC has changed by 10% or more when compared to the historical mean (Peings and Magnusdottir, 2014). In these areas, we instead use a SST climatology from the 2051-2080 LENS mean. Previous AGCM sea ice studies (e.g., Peings and Magnusdottir, 2014; Sun et al., 2015) have fixed SIT at 2-m across the entire Arctic Ocean. To compare our atmospheric responses with these earlier studies, we conduct two simulations with SIT set to 2-m across the Arctic (HIC and FIC). HIC is prescribed with a repeating historical SIC climatology, while FIC is set to a repeating future SIC climatology. The response to loss of SIC is represented by ΔSIC (FIC minus HIC).

To isolate the atmospheric response from a change in SIT alone, we conduct two simulations (HIT and FIT). Both simulations have a prescribed historical SIC and historical SST from the LENS mean. However, HIT consists of SIT set to a repeating historical climatology taken from the 1976-2005 LENS mean, whereas FIT is set to the 2051-2080 LENS mean. To keep SIC constant between experiments, we set SIT to a thin layer (0.15 m) in grid cells where ice fractions become open water in the future period. Therefore, the total SIE is unchanged between HIT and FIT. In this case, we partially neglect the influence of SIC on the atmospheric response and instead isolate the role of SIT. We denote the response to loss of SIT as ΔSIT (FIT minus HIT).

We conduct a fifth simulation (FICT) including both future SIC and SIT taken from the 2051-2081 LENS mean. Overall, the difference from the future simulations minus the historical simulations represents the sea ice effect and a local SST effect. The total response from projected sea ice loss (both concentration and thickness) is estimated from FICT minus HIT and represented as ΔNET. All statistical significance is determined at the 95% confidence level using the two-sided Student's t test.

Finally, to investigate the influence of SIT and SIC on the response to regional sea ice anomalies, we conduct two additional WACCM4 experiments. We follow the methods of Sun et al. (2015) in defining the regions, which we denote as polar (FPOL) and subpolar (FSUB). FPOL is defined as future SIC and SIT from the LENS 2051-2080 ensemble mean within the 66.6°N meridian and historical SIC and fixed 2-m SIT prescribed elsewhere. On the contrary, FSUB is prescribed with future SIC and SIT equatorward of 66.6°N and historical SIC and 2-m SIT within the Arctic circle. The sea ice anomalies in FSUB are mostly confined to the Sea of Okhotsk and Bering Sea. Our experiments differ from Sun et al. (2015) in that we are interested in the impacts of using a realistic SIT distribution rather than a fixed value (2-m) for the sea ice anomalies. SST are set to historical values or following the methods described in Section 2. We assess the atmospheric response by subtracting HIC from each of the experiments (FSUB, FPOL).

3.3 Results

3.3.1 Projected Arctic sea ice loss

The wintertime (DJF) SIC and SIT distributions and their differences between historical and future periods are depicted in Figure A.5. Previous studies (e.g., Rinke et al., 2006) have shown the greatest atmospheric response to changes in Arctic SIT during the boreal winter. In an earlier study (Labe et al., 2018a), we show that the spatial and temporal variability of SIT in LENS closely compares with satellite-based SIT estimates and output from an atmospheric-forced ice-ocean model. The wintertime difference between the future and historical periods (F–H; Figure A.5) of SIT highlights a dramatic thinning across the entire Arctic Ocean. Reductions of >3 m thickness are found along the Canadian Arctic Archipelago and Greenland coastlines, 1-2 m in the central Arctic to Siberian coastline, and 0.5-1 m in the far marginal seas (not shown). On the contrary, wintertime losses of SIC are only confined to the outer marginal seas (bottom right; Figure A.5). During the fall (October to November), the loss of SIC is more widespread and includes portions of the central Arctic basin (Figure A.6). The seasonal cycles of SIT and SIC from October through March are shown in Figure A.7.

3.3.2 Atmospheric thermodynamic response

The mean wintertime (DJF) 2-m air temperature response to future SIT (ΔSIT; a), future SIC (ΔSIC; b), and the total sea ice change (ΔNET; c) are shown in Figure 3.1. Warming from loss of SIT (Figure 3.1a) is confined fairly uniformly over the Arctic Ocean. Consistent with Lang et al. (2017), positive anomalies are generally found near the surface (below 850 hPa) without a statistically significant temperature response in the zonally averaged

atmospheric column in the troposphere and stratosphere (Figure A.8). Figure 3.1a shows small negative anomalies ($\sim$ -1°C) over portions of Eurasia. Cooling is also present to a lesser extent in the response to future SIC (Figure 3.1b) over a similar region. The negative anomalies in both ΔSIT and ΔSIC extend into the lower troposphere over Eurasia as shown in Figure A.9. This pattern of Eurasian cooling is found in other AGCM sea ice studies (e.g., Peings and Magnusdottir, 2014; Nakamura et al., 2015; Sun et al., 2015). The mechanisms driving the larger cooling response in ΔSIT compared to ΔSIC are still unclear. One possible explanation is that the local thermodynamic effect from greater warm anomalies extending over land may cancel the dynamically-induced cooling in ΔSIC (Screen et al., 2015).

The spatial coverage of positive anomalies is significantly larger in the response to the reduction of SIC shown in Figure 3.1b. Warmth is greatest over the outer marginal seas, which is consistent with the largest reductions in SIC. Smaller positive anomalies ($<$ 5°C) also extend over land, particularly in Greenland, North America, and eastern Russia. The 2-m air temperature response to the net sea ice effect (Fig 1c; ΔNET) indicates significant warming of more than 15°C across the entire Arctic Ocean. The extent and magnitude of the negative anomalies over Eurasia are also greater ($\sim$ -2°C) from the combined effects of reduced SIC and SIT. The warming of the Arctic Ocean is more uniform than in Figure 3.1b in response to significantly thinner sea ice and greater open water in the Barents-Kara Seas and portions of the Beaufort, Chukchi, and East Siberian Seas. We note that adding the temperature response from ΔSIT (Figure 3.1a) plus ΔSIC (Figure 3.1b) almost gives the temperature response in Figure 3.1c.

The seasonal cycle of net surface turbulent heat flux (sensible plus latent) is shown in Figure 3.1d for the three experiments (Figure 3.1a,b,c). The maximum in all experiments is reached in December after the sea ice minimum earlier in the fall. The net flux is averaged north

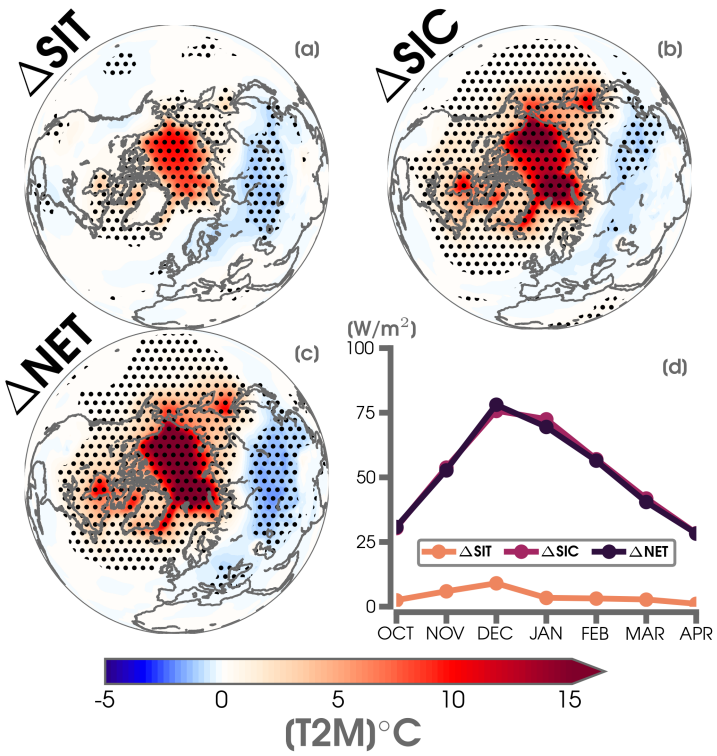

Figure 3.1: Responses of mean winter (DJF) 2-m air temperature (°C) from (a; ΔSIT) future sea-ice thickness, (b; ΔSIC) future sea-ice concentration, and (c; ΔNET) net future sea ice effect. Statistical significance at the 95% confidence level is identified by the black stippling. Note the difference in color scaling between positive and negative values. Responses of the mean DJF turbulent fluxes (sensible plus latent; W m^{-2}) are shown in (d) for the experiment comparisons in (a, b, c).

of 40°N where SIC is greater than 10% in the control (HIT or HIC). We only show the net turbulent flux as its contribution from loss of sea ice dominates compared to the radiative fluxes (Deser et al., 2010). Energy (surface heat flux) is communicated to the atmosphere in response to the large winter air-ocean temperature gradient. The flux response is significantly greater in the future SIC experiments, resulting from the reduction and removal of sea ice fraction in the marginal seas exposing more open water. Since SIC is held to historical values in the ΔSIT experiment, the net flux is smaller and transmitted through the sea ice, rather than directly from an open ocean-air exchange. Nevertheless, reduced ice thickness still contributes to an area-integrated turbulent heat flux anomaly, mainly during the winter

season, which results in a thermodynamic (surface warming) and a dynamic atmospheric response (Krinner et al., 2009).

3.3.3 Circulation response

We show the mean winter atmospheric circulation response to the three future sea ice experiments in Figure 3.2. A dipole pattern of reduced sea level pressure (SLP) over the central Arctic Ocean and higher SLP over northern Eurasia is found in response to future SIT (Figure 3.2a). This spatial pattern is somewhat similar to ΔSIC (Figure 3.2b; SIC alone) and ΔNET (Figure 3.2c; combined) experiments, but with a lesser amplitude. Both ΔSIC and ΔNET suggest a zonal wavenumber 1-like anomaly pattern. However, the negative SLP anomalies in ΔSIT are only confined to the central Arctic in response to the greatest surface forcing from loss of thickness. Unlike the experiments with loss of SIC, there are no significant SLP responses in the North Pacific or North America from reduced SIT. A large SLP response in the North Pacific is also found in other SIC perturbation experiments (e.g., Peings and Magnusdottir, 2014).

No response in the 500-hPa geopotential height (Z500) is found over the central Arctic in ΔSIT (Figure 3.2d). The response is equivalent barotropic over most of the North Atlantic and Eurasia, except for in east Asia where negative 500-hPa anomaly and a positive SLP response is found. While the response in ΔSIT at 500-hPa is small, the spatial pattern partially resembles the negative phase of the NAM. A negative phase of the NAM in winter is consistent with earlier studies from projected sea ice loss (e.g., Deser et al., 2010; Peings and Magnusdottir, 2014; McKenna et al., 2017). The response from ΔSIC in Figure 3.2e and ΔNET in Figure 3.2f indicates a much larger Z500 response with increasing heights over the

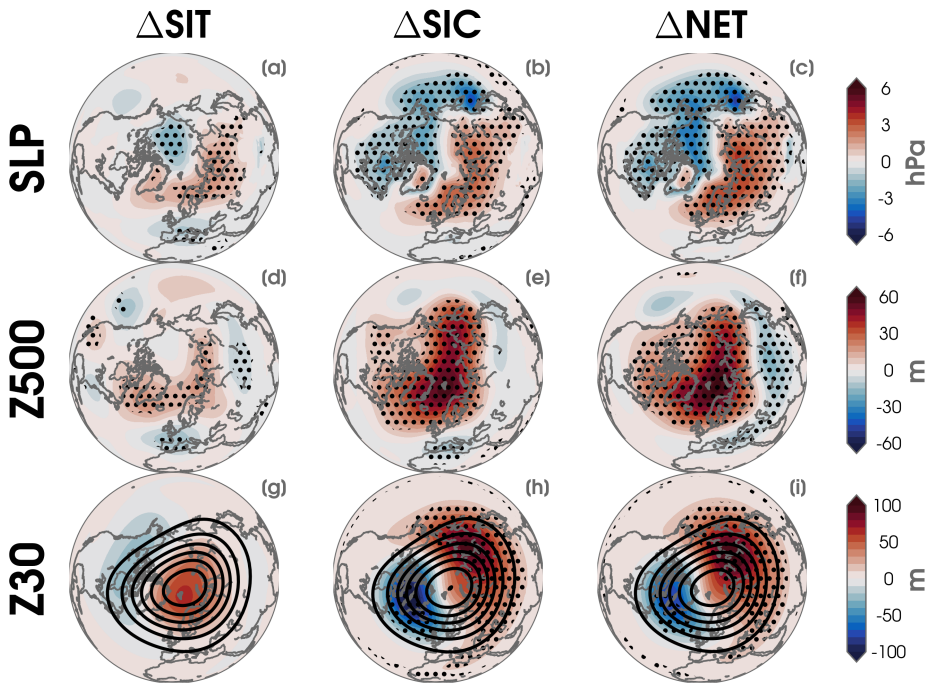

Figure 3.2: Mean winter (DJF) responses for sea level pressure (SLP; hPa), 500-hPa geopotential height (Z500; m), and 30-hPa geopotential height (Z30; m). Statistically significant anomalies at the 95% confidence level are shown by the black stippling. The climatological Z30 heights are superimposed from HIT in (g, i) and HIC in (h) with black contours at an interval of 250 m.

entire Arctic, particularly over the Barents-Kara Seas region. ΔNET (Figure 3.2f) shows an upper level ridge structure over the Arctic Ocean and a downstream trough over Eurasia. Interestingly, this trough feature in Eurasia is also present in ΔSIT (Figure 3.2d), but it is not statistically significant in ΔSIC (Figure 3.2e). Figure A.10 shows the daily evolution of the geopotential height response averaged over the polar cap (north of 67° N). The polar cap height response is an approximation for the daily NAM index, in which a positive anomaly is associated with a negative NAM (Baldwin and Thompson, 2009). We indeed find a significant positive anomaly throughout the winter in ΔSIC and ΔNET, but this response is mostly confined to the troposphere. Interestingly, only ΔSIT shows a statistically significant

anomaly in the stratosphere, which develops by mid-March and could be indicative of an early weakening of the polar vortex.

We investigate the DJF stratospheric response at the 30-hPa geopotential height (Z30) in Figure 3.2g,h,i. There is no significant response in the stratosphere from the loss of SIT (Figure 3.2g), but a strengthening and shift of the polar vortex towards the North Atlantic in ΔSIC (Figure 3.2h,i). Consistent with lower Z30 anomalies over the North Atlantic, we find positive anomalies of 10-hPa zonal winds (U10) in this region on the order of 3-6 m/s (not shown). Therefore, the loss of SIC contributes to a strengthening of the wintertime polar vortex in our experiments.

It has been shown that the spatial distribution of sea ice anomalies between the Pacific and Atlantic sectors contributes to an opposite sign response in the stratosphere (e.g., Sun et al., 2015; McKenna et al., 2017). As in Sun et al. (2015)'s Figure 3.4, we show our zonal-mean, zonal wind response for DJF in Figure A.11 for the two regional experiments. We also find an impressive contrast between responses from prescribed regional sea ice anomalies. Sea ice anomalies in the high polar region are mostly found in the Atlantic sector, such as the Barents-Kara Seas, and contribute to a significant weakening of the polar vortex. In the subpolar experiment (FSUB minus HIC), the anomalies are not significant at the 95% confidence level. However, the spatial pattern suggests a strengthening of the polar vortex with a maximum near 10 hPa. These results are in agreement with analysis of the zonal-mean response of geopotential heights over the polar cap (not shown). While the polar sea ice anomalies contribute a larger and statistically significant response (weakening of the polar vortex) than the strengthening response from the subpolar experiment, it is interesting to note that the anomalies in ΔNET show a strengthening of the polar vortex. As shown in Figure A.12, the polar and subpolar responses are therefore not additive (nonlinear), mostly

in the stratosphere.

We further explore the monthly evolution of the zonal-mean, zonal wind response from future SIT (ΔSIT) and the net sea ice effect (ΔNET) in Figure 3.3. The climatological wind from HIT is superimposed over the anomalies. We see little response in the troposphere or stratosphere resulting from SIT loss. There is a statistically significant decrease in the stratosphere during March, which may suggest an early breakdown of the wintertime polar vortex. This is consistent with the analysis in Figure A.10. Further investigation (not shown) of the mechanisms for this weakening of the polar vortex remain unclear.

A clearer tropospheric response is shown from the loss of both SIT and SIC in Figure 3.3 with a weakening of the westerlies and equatorward shift of the jet, especially in December and January. This response is primarily from the contribution of SIC loss with a similar magnitude and sign zonal-mean, zonal wind anomaly found in ΔSIC (not shown). Similar to Sun et al. (2015), the primary contribution to the equatorward shift of the midlatitude jet is found in the polar sea ice anomalies experiment (FPOL minus HIC) with a robust weakening of the westerlies also in December and January. On the contrary, we find only a small statistically significant decrease between 50-60°N in January from the subpolar sea ice loss (not shown).

3.3.4 Relative contributions from ice thickness

To assess the atmospheric response from SIT compared to SIC, we compute the relative magnitude and spatial correlation (Pearson's r) of various thermodynamic and dynamic responses for DJF in Table 3.1. The response contributions (%) are computed as the ratio

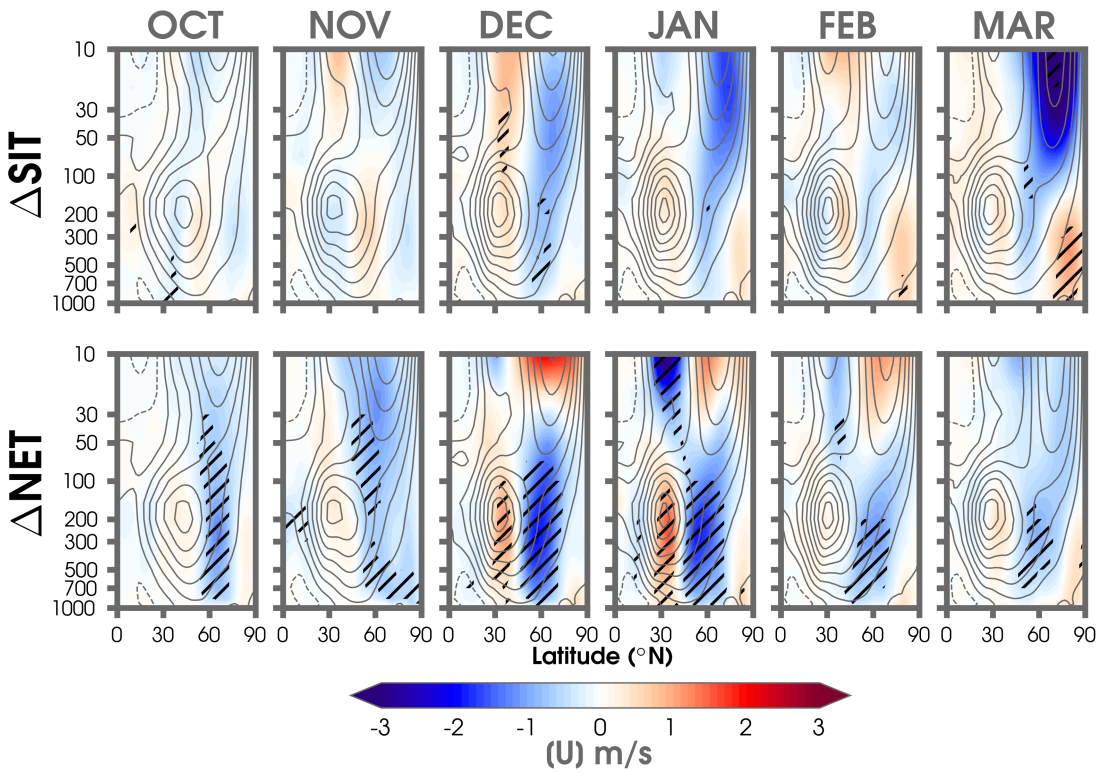

Figure 3.3: Monthly zonal-mean, zonal wind (U; m s^{-1}) responses comparing the effect of future sea-ice thickness (ΔSIT; colored shading) and the combined effect of sea-ice thickness and sea-ice concentration loss (ΔNET; colored shading). Climatological zonal-mean, zonal wind from HIT is overlayed by the grey contours (interval of 5 m s^{-1}) in each month. Statistically significant responses at the 95% confidence level are shown by the black hatching.

of the absolute value of ΔSIT or ΔSIC over ΔNET for the area-weighted average poleward of 40°N (significant at the 95% confidence level). As a result of the little to no significant stratospheric response from SIT loss, we hence see no spatial correlation with the SIC response for the zonal wind at 10 hPa (U10) or the 30 hPa geopotential height anomaly (Z30). We find a closer pattern correlation in the troposphere from SIT and SIC loss, particularly at Z500 (r=0.53) and SLP (r=0.52). The SLP response from SIT contributes as much as 26% of the response from SIC loss, furthermore the spatial patterns of the response are similar. Interestingly, the response contributions between ΔSIT and ΔSIC are nearly linear for U300, Z500, and SLP. As expected, the closest agreement in response between SIT and SIC loss

is found in the thermodynamic fields at the surface. The 2-m air temperature response in ΔSIT is one third of that from SIC loss (r=0.89), although the warming from ΔSIC accounts for 90% of the total in ΔNET. Our results are consistent with prior studies (e.g., Lang et al., 2017; Sun et al., 2017) showing a contribution from thinning sea ice to near-surface Arctic amplification. The pattern correlations between ΔSIT and ΔSIC are also computed for each month in Figure A.11, with the closest agreement in the response sign found during the early winter, especially in December. The negative correlations of Z30 and U10 in March are in agreement with the stratospheric response shown in ΔSIT.

Table 3.1: Magnitude (ratios) of sea-ice thickness (ΔSIT; FIT–HIT) response and sea-ice concentration (ΔSIC; FIC–HIC) response compared to the net sea ice effect (ΔNET; FICT–HIT). Pattern correlations compare the response of ΔSIT with ΔSIC (averaged north of 40°N in DJF, for areas of at least 95% significance level only).

	Response Contribution (%)		Pattern Correlation (r)
	ΔSIT	ΔSIC	
U10	4	114	-0.12
Z30	2	116	-0.03
U300	19	69	0.46
Z500	16	88	0.53
SLP	20	76	0.52
T2M	30	90	0.89

3.4 Discussion and conclusions

This study assesses the role of SIT on the boreal winter large-scale atmospheric response from projected twenty-first century sea ice loss. It is shown that the magnitude of surface warming from future SIT loss is as high as one third of the response from SIC anomalies. We also find good qualitative agreement in the sign of the spatial pattern of tropospheric anomalies between SIT and SIC forcings. Further, the response from future SIT loss has a non-negligible influence on the large-scale dynamic circulation with a response contribution

in SLP up to 26% that of SIC. In particular, we find an enhancement of the Z500 and SLP anomalies from SIT loss. It is interesting to note the linearity in the responses to SIT and SIC loss. This is mostly found at the surface and lower to mid-troposphere. The combined loss of SIT and SIC shows a negative NAM response. In December and January, there is a robust equatorward shift of the Northern Hemisphere mid-latitude jet and weakening of the westerlies. This change in circulation is in agreement with the thermal wind balance and is a result of the substantial Arctic warming from sea ice loss and hence reduced meridional thermal gradient. Overall, we do not find a significant role of the stratosphere from the losses of SIT, SIC, or the combined forcing experiment. However, an opposing response in the stratosphere from regional sea ice anomalies in the subpolar oceans (mostly Pacific) and into the Arctic (mostly Barents-Kara Seas region) is demonstrated by including a realistic SIT and is in line with other studies (e.g., Sun et al., 2015; McKenna et al., 2017). The subpolar anomalies induce a stronger polar vortex in winter, while the polar sea ice response shows a significant weakening of the polar vortex.

It is worthwhile to note that our experiments do not reflect the importance of ocean-atmospheric interactions (Deser et al., 2015). We instead performed idealized perturbation experiments to better understand the role of using a realistic distribution of SIT. Further sensitivity studies on the effects of SIT loss using other AGCMs is needed, as the atmospheric response could depend on model physics (Screen et al., 2018a) or the use of a low-top vs. high-top model (Sun et al., 2015). In that regard, the newly-designed Polar Amplification Model Intercomparison Project will represent an excellent opportunity to coordinate sensitivity experiments to sea ice anomalies, including sea-ice thickness.

Preliminary results suggest the stratosphere-troposphere pathway from sea ice loss is sensitive to the phase of the QBO, which has been shown to modulate other surface-stratosphere

teleconnections (Peings et al., 2017). This will be the subject of future investigation. In summary, our results indicate a notable influence on the large-scale atmospheric circulation communicated by the surface heat flux anomaly transmitted through the thinner sea-ice cover. We recommend prescribing a realistic SIT distribution in future AGCM experiments in order to reveal the total atmospheric response from sea ice loss.

Acknowledgements

This project was supported by NSF grants AGS-1624038 and NRT-1633631. We would like to thank Russell Blackport for providing the modified CICE4 code to read in the sea-ice thickness data. We acknowledge high-performance computing support from Cheyenne (doi:10.5065/D6RX99HX) provided by NCAR's Computational and Information Systems Laboratory, sponsored by the National Science Foundation. We also thank the CESM Large Ensemble Community Project with supercomputing resources provided by NSF/CISL/ Yellowstone. CESM-LENS data is available at `http://www.cesm.ucar.edu/`. The WACCM4 model experiment output is available and stored on Cheyenne's High Performance Storage System (HPSS) long-term data archive. This data is available by contacting the corresponding author. We thank the editor and two anonymous reviewers for their helpful suggestions and comments to improve the manuscript.

Chapter 4

The effect of QBO phase on the atmospheric response to projected Arctic sea-ice loss in early winter

As appears in:

Labe, Z.M., Y. Peings, and G. Magnusdottir (2019), The effect of QBO phase on the atmospheric response to projected Arctic sea-ice loss in early winter, *Geophysical Research Letters*, 46(13), 7663-7671, doi :10.1029/2019GL083095.

Abstract

Recent modeling studies have shown an important role for stratosphere-troposphere coupling in the large-scale atmospheric response to Arctic sea-ice loss. Evidence is growing that the Quasi-biennial Oscillation (QBO) can contribute to or even mitigate teleconnections from surface forcing. Here, the influence of QBO phase on the atmospheric response to projected

Arctic sea-ice loss is examined using an atmospheric general circulation model with a well-resolved stratosphere and a QBO prescribed from observations. The role of the QBO is determined by compositing seasons with easterly phase (QBO-E) separately from seasons with westerly phase (QBO-W). In response to the sea-ice forcing in early winter, the polar vortex during QBO-E weakens with strong stratosphere-troposphere wave-1 coupling and a negative NAM-type response. At the surface, this results in more severe Siberian cold spells. For QBO-W, the polar vortex strengthens in response to the sea-ice forcing.

4.1 Introduction

The pronounced warming in the Arctic over recent decades may not only affect the local climate, but also mid-latitude areas through atmospheric teleconnections (e.g., Cohen et al., 2014). The remote impact of Arctic sea-ice loss is unclear due to disagreement in the atmospheric response among modeling studies and low signal-to-noise ratio (e.g., Overland et al., 2016; Smith et al., 2019). However, recent coupled global climate model experiments where sea-ice is forced to substantially decrease by longwave radiative forcing (Tomas et al., 2016), albedo change (Blackport and Kushner, 2017) or by nudging (Smith et al., 2017), find robust response to the sea-ice forcing as summarized in Screen et al. (2018a).

Studies have pointed to the importance that the stratospheric circulation may play in shaping the response to sea-ice forcing (e.g., Kim et al., 2014; Peings and Magnusdottir, 2014; Sun et al., 2015; Zhang et al., 2018a). Anomalies in the polar stratosphere driven by wave breaking of surface-forced planetary waves affect the tropospheric circulation through the Northern Annular Mode (NAM; Baldwin and Dunkerton, 2001). Specifically, boundary conditions such as sea surface temperature (SST), sea-ice concentration/thickness (SIC/SIT), or snow anomalies impact the polar stratosphere when the tropospheric anomalies they gener-

ate constructively interfere with the climatological stationary waves (Fletcher and Kushner, 2011; Smith et al., 2011; Henderson et al., 2018).

Any teleconnection that involves stratosphere-troposphere coupling may be impacted by the Quasi-biennial Oscillation (QBO), a ∼28 month oscillation of the equatorial zonal wind in the stratosphere (Baldwin et al., 2001). As first hypothesized by Holton and Tan (1980), the QBO may affect the strength of the Northern Hemisphere polar vortex by altering the background flow and the propagation of extratropical planetary waves in the polar stratosphere. This mechanism is usually referred to as the Holton-Tan effect and is apparent in observations as well as model simulations (e.g., Watson and Gray, 2014; Anstey and Shepherd, 2014). Although the QBO is an importance source of predictability for Northern Hemisphere winter surface climate (Thompson et al., 2002), models generally simulate a weaker extratropical signal than in reanalysis (Scaife et al., 2014; Andrews et al., 2019). Further, the role of the QBO in modulating teleconnections related to surface forcings has received little attention. Some studies have explored how the QBO modulates the atmospheric response to Eurasian snow anomalies (Peings et al., 2017; Tyrrell et al., 2018), but to our knowledge no studies have evaluated its influence on the atmospheric response to Arctic sea-ice change.

Here we address the role of the QBO in teleconnections involving surface forcing due to sea-ice melt. We build primarily on two of the experiments considered in Labe et al. (2018b) using a high-top atmospheric global climate model (AGCM) for forcing of SIC and SIT. In this work, we have extended the number of ensemble members for each experiment in Labe et al. (2018b) from 100 to 200 and focus on the response in relation to QBO phase.

4.2 Methods, model, and experiments

The AGCM used in this study is the specified chemistry version of WACCM (SC-WACCM4; Smith et al., 2014). It includes CAM4 physics, 66 vertical levels (up to 5.1×10^{-6} hPa, ∼140 km), and a parameterization of nonorographic gravity waves that contributes to the realistic frequency of stratospheric sudden warming events (Richter et al., 2010). The QBO is prescribed in the model by relaxing equatorial (between 22°S and 22°N) zonal winds from 86 to 4 hPa to the observed ∼28-month cycle from radiosonde observations (Hansen et al., 2013). The horizontal resolution is 1.9° latitude by 2.5° longitude. Two ensembles of simulations are branched from a 200-year control as described in Peings et al. (2017).

Our model setup is the same as in Labe et al. (2018b), but extended to 200 ensemble members per experiment to increase the number of seasons composited per QBO phase. Each simulation is prescribed with annually repeating cycles of SST, SIT, and SIC, which are taken from the mean of forty ensemble members from the fully coupled Community Earth System Model Large Ensemble (LENS; Kay et al., 2015). LENS uses historical forcing and then continues to the end of the 21st century under Representative Concentration Pathway 8.5. Earlier studies (e.g., Jahn et al., 2016; Labe et al., 2018a) have demonstrated that LENS captures spatial patterns of sea-ice variability quite well when compared with current satellite observations. Our two experiments represent sea-ice conditions in the 1976-2005 observational period (hereafter, historical) and projected sea-ice conditions during 2051-2080 (hereafter, future). Following convention, SST are set to historical values in all grid cells, except where SIC has changed by more than 10% in the future experiment. In these SIC loss areas, SST are set to the 2051-2080 LENS mean. A thorough description of these experiments can also be found in Labe et al. (2018b)'s Table S1 (HIT for historical, FICT for future). Figure A.14a-f shows the difference in SIC and SIT between the future and historical experiments for October, November and December. Widespread loss of SIC (∼ 75-100%)

is found in October and November with almost ice-free conditions across the Arctic Ocean (Figure A.14a-b). The reduction in sea-ice cover leads to an upward (positive) surface heat flux response in areas of thinner ice and newly open water, up to 100 W m^{-2}, primarily due to turbulent heat flux (Figure A.14g-i).

The QBO index is defined as the average October to November 30-hPa zonal wind from 5°S to 5°N. We composite winters into easterly (QBO-E) or westerly (QBO-W) phases by the lower and upper terciles of the QBO index (i.e., approximately 67 winters per phase). As shown in Hansen et al. (2013) and Peings et al. (2017), SC-WACCM represents the Holton-Tan effect, with weaker (stronger) westerlies circling the polar vortex under QBO-E (QBO-W).

The atmospheric response to Arctic sea-ice loss is obtained by subtracting the historical ensemble mean from the future ensemble mean after compositing by QBO phase. Statistical significance of the atmospheric response is determined using the two-sided Student's t test at the 95% confidence level, unless otherwise stated. Here we focus on the atmospheric response in early boreal winter (November to December) when the QBO influence is greatest in our model. This period is consistent with earlier studies showing a larger Holton-Tan effect in both observations and models in early winter (Anstey and Shepherd, 2014).

4.3 Large-scale atmospheric response

4.3.1 Free troposphere/stratosphere response

Figure 4.1 shows the December atmospheric response to the sea-ice forcing (future minus historical) composited by QBO phase. The right-hand column shows the difference in response depending on QBO phase (QBO-E minus QBO-W) and only areas that are statistically significant at the 90% confidence level are shaded. The overall tropospheric response corresponds to a negative NAM signature, with higher 500 hPa geopotential height (Z500) over the pole, and lower Z500 in mid-latitudes (Figures 1a-b). This NAM response is stronger over the Atlantic for QBO-W (Figure 4.1a) and over the Pacific for QBO-E (Figure 4.1b) and is associated with equatorward shifts of the mid-latitude jet streams (Figure 4.1d-e). While at first glance the two responses are similar, they project differently on the climatological stationary wave pattern. Under QBO-E, the tropospheric response reinforces wave number 1 (Figure 4.1h), while this is not the case in QBO-W (Figure 4.1g). Therefore, QBO-E promotes constructive interference (Smith et al., 2011) and anomalous Rossby wave propagation into the stratosphere in December. Consistently, a warming of the polar stratosphere is found under QBO-E (Figure 4.1k-l), while QBO-W rather exhibits a cooling and a shift of the polar vortex towards the North Atlantic sector (Figure 4.1j). The statistical significance of the results in Figures j-k is also robust when using a 10,000 bootstrap resampling method instead of the two-sided Student's t test (black stippling).

The stratospheric response under QBO-E is consistent with constructive intereference between the forced wave number 1 and the climatological stationary wave 1 (Figure 4.1h). A more complete visual of linear interference between the forced and climatological stationary wave is provided in Figure A.15. For QBO-E, there is large coherence between the climatological and forced wave number 1 (R = 0.87), while for wave number 2 the two fields

are uncorrelated. This is consistent with other studies finding that the Holton-Tan effect is primarily driven by modulations of wave number 1 in early winter (Hu and Tung, 2002; Ruzmaikin et al., 2005). For QBO-W (top), the correlation is considerably less for the total (left) and wave number 1 (center) forced and climatological fields indicating there is less wave number 1 propagation into the stratosphere. For wave number 2 the spatial correlation is higher, but that is entirely due to values within the troposphere (right).

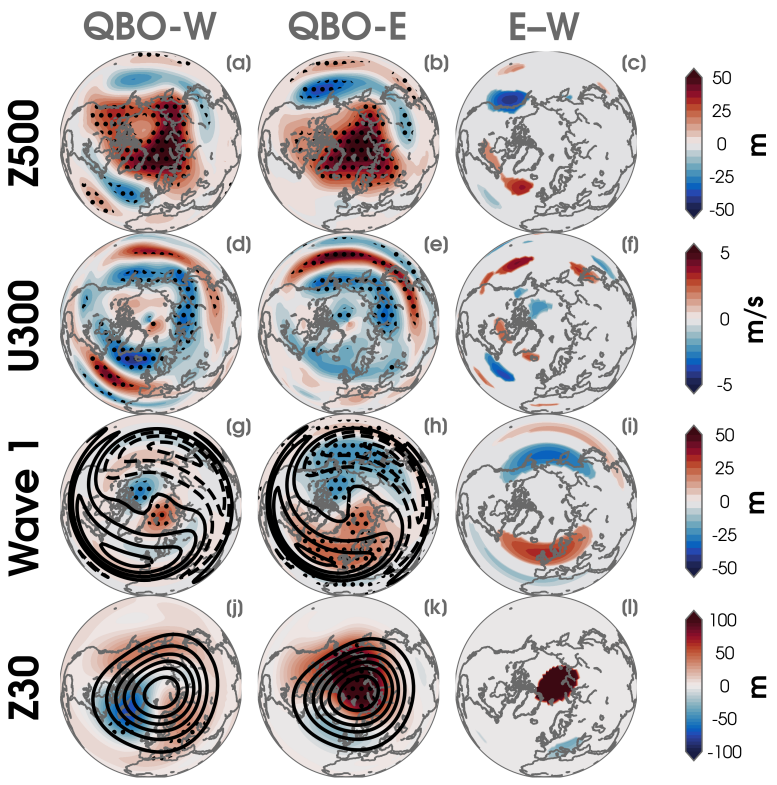

Figure 4.1: (a) December response to sea-ice loss of the 500-hPa geopotential height (Z500) under QBO-W (Future-QBO-W minus Historical-QBO-W); (b) Same as (a), but for QBO-E; (c) Difference in the response under QBO-E minus QBO-W. Color shading indicates areas with at least 90% statistical significance; (d-f) Same as (a-c) but for the 300-hPa zonal wind (U300); (g-i) same as (a-c) but for the zonal wave number 1 component of the 300-hPa geopotential height (Wave 1). The 300-hPa climatological wave number 1 from the historical simulation is superimposed (50 m interval, black contours); (j-l) Same as (a-c) but for the 30-hPa geopotential height (Z30). The climatological Z30 heights from the historical simulation are superimposed (250 m interval, black contours). Black stippling is shown for statistically significant anomalies at the 95% confidence level in the first two columns.

The daily evolution of the geopotential response to sea-ice forcing, integrated over the polar cap (north of 65°N), is shown as a function of height in Figures 4.2a-b for October-March. For QBO-W, the statistically significant response is confined to the troposphere, with the positive polar geopotential response corresponding to the negative NAM observed in the mid-troposphere in Figure 4.2a. In the stratosphere, the polar vortex strengthens through early winter, with little statistical significance in the anomalies. However, under QBO-E, there is a robust stratospheric response to the forcing in late November and December. This diagnostic clearly indicates that for QBO-E the stratospheric pathway has a role in the large-scale circulation response to the sea-ice. While our focus is on early winter due to greater statistical significance, there is also a difference in the stratospheric response between QBO phases through the end of winter.

Figures 4.2c-d show the response of the November-December (ND) vertical component of the Eliassen-Palm flux (Plumb, 1985), equivalent to the meridional eddy heat flux, in a latitude-pressure cross section. The zonal-mean, zonal wind response in both QBO phases is also superimposed on the normalized flux anomalies. Both phases exhibit responses in the troposphere, with an equatorward shift of the westerlies, in line with previous studies that investigated the response to future Arctic sea-ice loss (Screen et al., 2018a; Labe et al., 2018b). However, under QBO-E, the weakening of the westerlies extends to the stratosphere and is associated with increased vertical wave activity flux (WAFz) throughout the vertical column centered at 50°N (Figure 4.2d). In contrast, under QBO-W, the zonal-mean WAFz anomalies are confined in the tropophere (Figure 4.2c). The question is: under QBO-E conditions, where does this flux originate from? To answer that question, in Figure A.16 we examine WAFz for the ND response to sea-ice forcing under QBO-W (left) and QBO-E (right). At 850 hPa under QBO-E, WAFz is positive largely in areas corresponding to the sea-ice forcing. By contrast at 150 hPa, which is in the lower stratosphere, the area where the flux is strongly positive and statistically significant is in the area of the Siberian High.

This flux is weaker and insignificant under QBO-W. We will look closer at this region and its importance for the response in the next section.

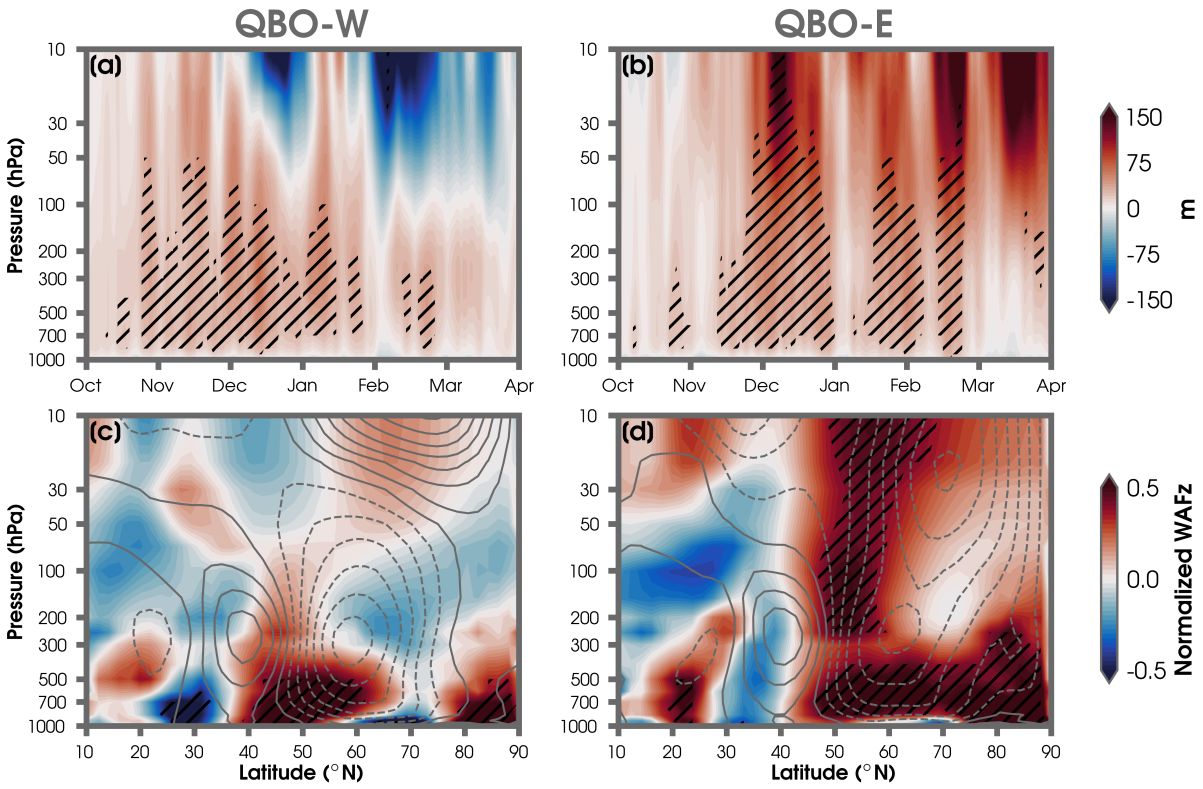

Figure 4.2: (a-b) Geopotential height response to sea-ice decline as a function of height (pressure) over the polar cap (>65°N) for QBO-W (a) and QBO-E (b). Anomalies are shown from October 1 through March 31. (c-d) Zonally-averaged response (latitude-pressure vertical profile) of the normalized vertical wave activity flux (WAFz) averaged for November and December. The gray contours show the zonal-mean, zonal wind anomalies (0.25 m/s contour interval, dashed contours indicate negative values). Black hatch marks indicate statistical significance at the 95% confidence level.

4.3.2 Surface temperature response

The concurrence of Arctic sea-ice anomalies with recent cold extremes has led to the hypothesis that they may be causally related, i.e., that Arctic sea-ice loss may lead to winter

cold extremes. However, linking sea-ice loss to cold extremes and to the "warm Arctic, cold continent" spatial temperature pattern is not robust, neither in reanalysis nor in climate models (Overland et al., 2011; Barnes and Screen, 2015; Mori et al., 2014; Screen et al., 2015; Sun et al., 2016; Mori et al., 2019). Here we examine whether there is also a different signal at the surface depending on QBO phase.

Following the methods of Peings et al. (2018), we assess the change in cold temperature extremes by defining a cold-days index (CDI; degree day). At each grid point, a December CDI is computed by summing each daily deviation of the 1000-hPa temperature from its corresponding daily 10th percentile, based on the historical distribution. Therefore, this index captures both changes in frequency and intensity of cold extremes. Figure 4.3a shows a spatial map of the change in CDI due to sea-ice loss and filtered by QBO phase. For both QBO-W and QBO-E there is a substantial reduction in CDI intensity (positive anomalies) over high-latitude North America and much of northern Eurasia during December. This is in response to warm air advection induced by sea ice loss. However, under QBO-E, there is a significant increase in CDI intensity (negative anomalies) over central and eastern Asia.

Figure 4.3b shows the probability density function (PDF) for the daily December 1000-hPa temperature anomalies within the area of the cold patch in Figure 4.3a (35-60°N, 70-140°E). The Kolmogorov-Smirnov two-sample test is used to compare the shape of the distributions of the responses to sea-ice loss under QBO-E and QBO-W. They are statistically different ($p < 0.001$), and for QBO-E the PDF is shifted to cooler temperatures with an increased variance. Although this area of cooling is similar to the 2-m temperature response in Labe et al. (2018b), it is further amplified under QBO-E. These results suggest that the surface response to sea-ice loss is modulated by the QBO and leads to an intensification of the cold

temperature extremes under QBO-E.

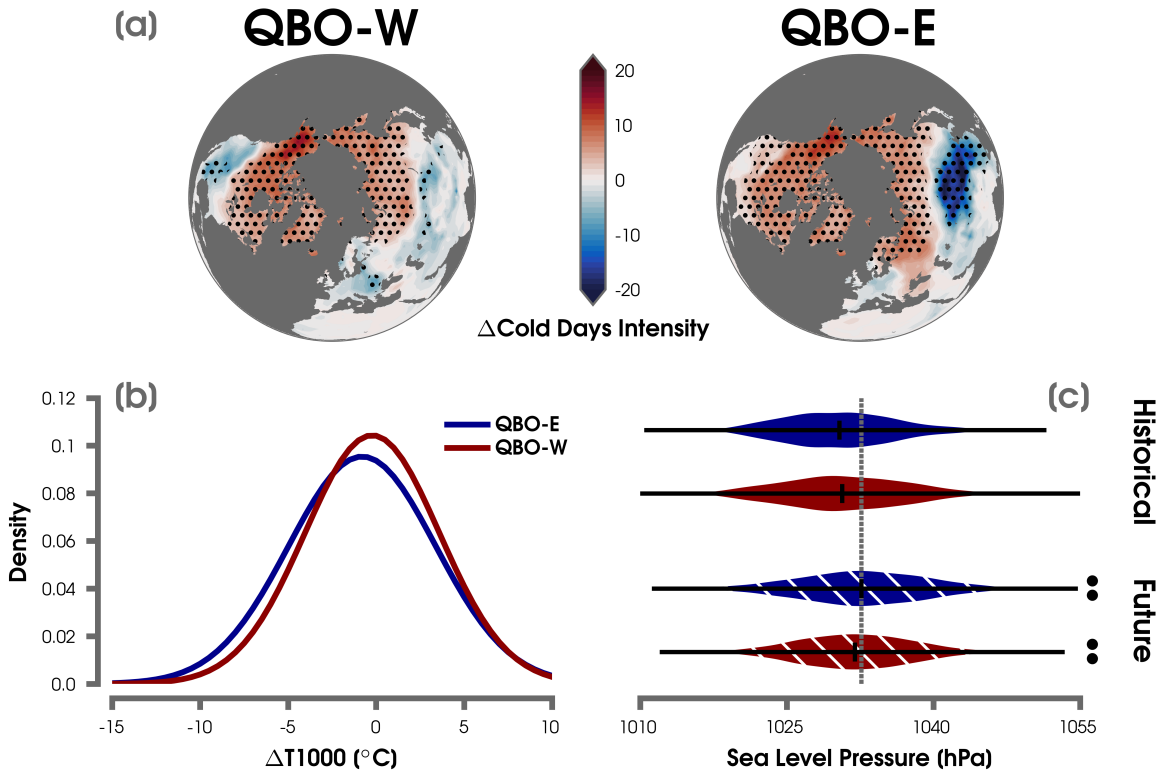

Figure 4.3: (a) Change in December cold day intensity (CDI) for each QBO phase in response to sea-ice decline. Statistical significance at the 95% confidence level is indicated by the black stippling. (b) The normalized probability density functions of the daily December temperature at 1000-hPa (T1000) response to sea-ice loss for Eurasia (35-60°N and 70-140°E). The T1000 responses are composed by the easterly (QBO-E; blue) and westerly (QBO-W; red) phases of the QBO. (c) Violin plots of the distributions of average daily sea level pressure over the Siberian High region (40-65°N and 80-120°E) in the historical and future experiments. Black lines show the median in each distribution. The dashed grey vertical line is displayed to highlight the median of the future QBO-E simulation. White hatch marks and the two black dots indicate a statistically significant difference in the means and between QBO-E and QBO-W composites in each experiment, respectively.

The advection-induced cooling over central and eastern Asia is thought to arise from the intensification of the Siberian High (Mori et al., 2014). We show violin plots (Figure 4.3c) of the daily Siberian High Index (SHI) using sea level pressure averaged over 40-65°N and 80-120°E, which corresponds to the area of the Siberian High (Panagiotopoulos et al., 2005). The violin plots show the median SHI (center black lines) in addition to its kernel probability density symmetric around the 5th-95th percentile range (horizontal lines). We find a slightly stronger Siberian High response under QBO-E compared to QBO-W ($p < 0.001$). Note that under both QBO phases the Siberian High strengthens due to sea-ice loss. This helps explain the similar location of the CDI minima for both QBO phases, although for QBO-E the amplitude is substantially larger.

An outstanding question is whether the stronger Siberian High response under QBO-E is driven by the polar vortex weakening. To investigate this question, Figure 4.4 shows daily time series of the responses in meridional eddy heat flux at 100 hPa ($\overline{v'T'}$; MHF100), SHI, 1000-hPa temperature over Eurasia (T1000), and 30-hPa geopotential (Z30) averaged over the polar cap. During QBO-E in early December, positive MHF100 anomalies coincide with a strengthening of the SHI and decrease in mean temperature. This is followed by a stratospheric warming in mid-December, and persistent Siberian High and cold temperature anomalies in December (bottom). Over the entire season, the SHI is highly anticorrelated to T1000 (R = -0.86). Based on these results, we propose the following interpretation to explain how the QBO modulates the response to sea-ice in our experiments: (1) the QBO modulates the wave number 1 pattern response to sea-ice anomalies (Figures 1g-h); (2) the enhancement of the Siberian High induces upward wave activity anomalies that lead to a warming of the polar stratosphere; (3) the stratospheric anomaly propagates downward (Figure 4.2b) and reinforces the Siberian High/cold eastern Asia anomalies (Figure 4.3a). Thus, the Eurasian cooling is primarily driven by tropospheric processes, but the stratosphere reinforces the tropospheric response, leading to greater persistence in the Siberian High anomaly. Under

QBO-W, episodes of strong SHI and T1000 are found, but they are less persistent, consistent with the absence of any stratospheric warming.

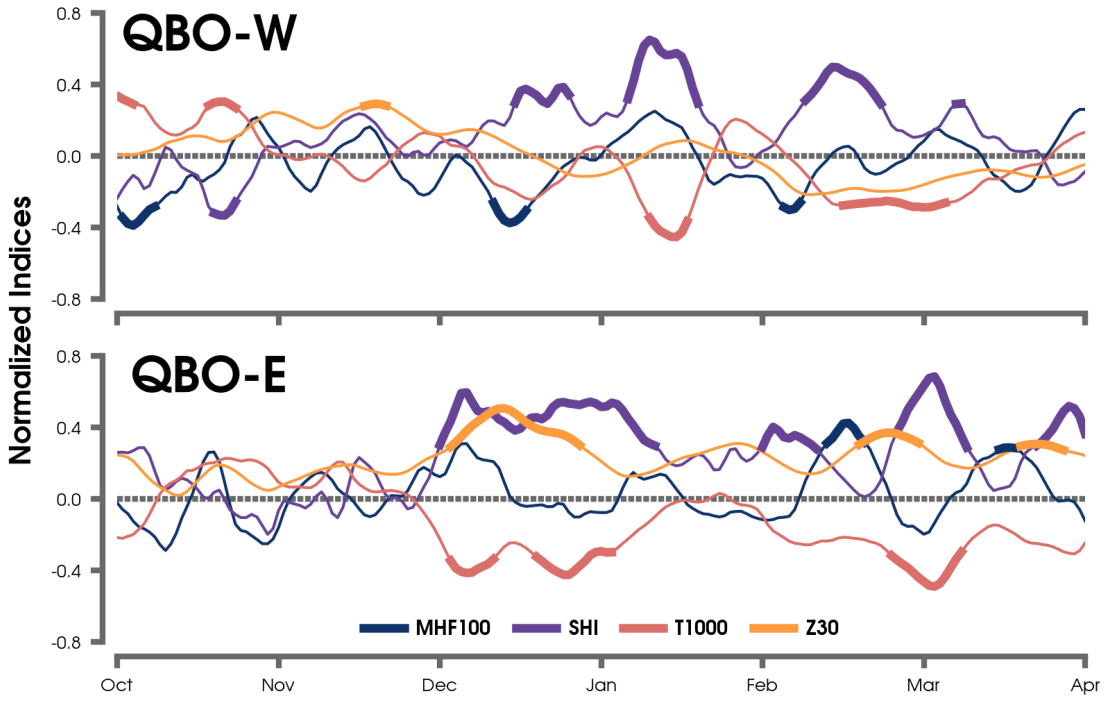

Figure 4.4: Daily time series of the zonal-average of the meridional eddy heat flux at 100 hPa (MHF100; blue line; 40-80°N), the Siberian High sea level pressure index (SHI; purple line; 40-65°N and 80-120°E), 1000-hPa temperatures in Eurasia (T1000; red line; 35-60°N and 70-140°E), and the geopotential at 30 hPa averaged over the polar cap (Z30; orange line; >65°N) for QBO-W (top) and QBO-E (bottom) phases in response to sea-ice loss. The fields have each been smoothed using a 10-day running average and normalized by their standard deviation. Statistical significance at the 90% confidence level is indicated by the bold line segments.

4.4 Conclusions

This illustrates for the first time how the QBO can modulate the atmospheric response to projected sea-ice loss using perturbation experiments with a high-top AGCM (SC-WACCM4). A robust weakening of the polar vortex is found under QBO-E in response to sea-ice decline. In contrast, there is a strengthening of the polar vortex under QBO-W. The total ensemble mean response shows a marginal strengthening of the stratospheric polar vortex as in Labe et al. (2018b), due to the fact that neutral QBO years exhibit a strengthening of the polar vortex (not shown). However, a modulation of the response in the mid-troposphere is not clear from this analysis.

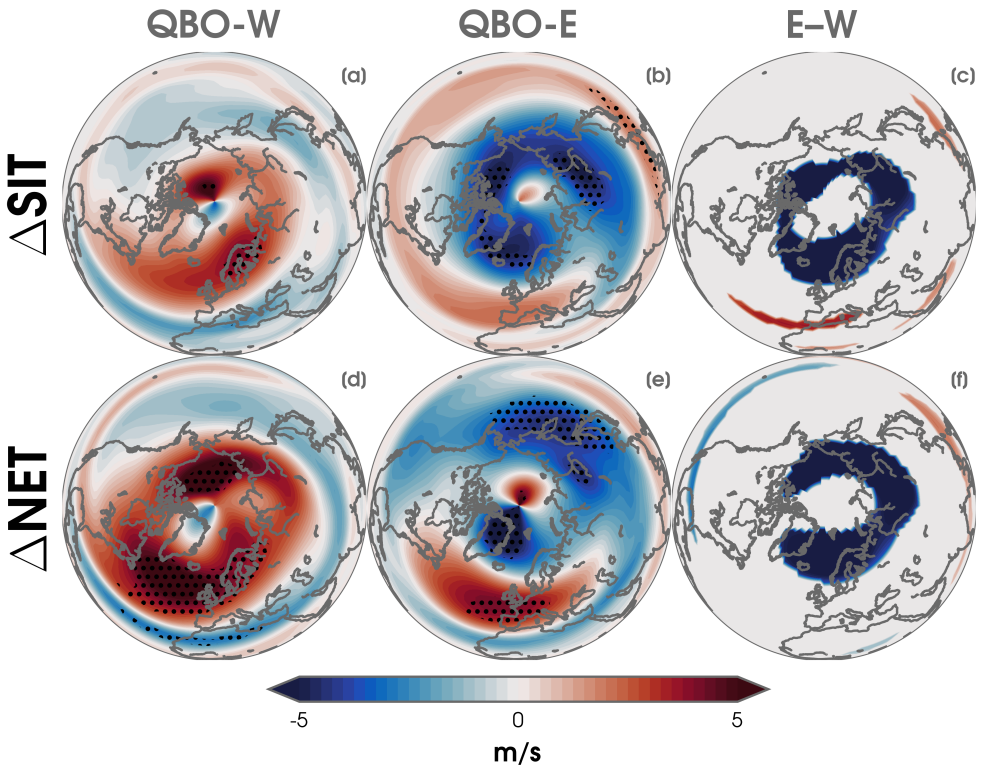

Figure 4.5: As in Figure 4.1, but for the December responses of the 10-hPa zonal wind in a sea-ice thickness-loss only experiment (ΔSIT; a-c) and the total sea-ice change (concentration and thickness) experiment (ΔNET; d-f).

The stratospheric response under QBO-E is driven by waves propagating into the stratosphere that coincide with the reinforcement of a wave number 1 pattern and a stronger Siberian High response than under QBO-W. As a consequence, the warm Arctic–cold Siberia pattern is only statistically significant under QBO-E. These results illustrate how sensitive the large-scale response to Arctic sea ice is, even when using a strong forcing as in this study. Depending on the phase of the QBO, the conclusions significantly differ, which may be problematic in modeling studies that do not include a realistic QBO or are run under permanent QBO conditions. We also find that additional experiments forced by sea-ice thickness only simulate a similar stratospheric response, despite much reduced heat flux anomalies at the surface (Labe et al., 2018b, Figure 4.1d). Figure 4.5 shows the 10-hPa zonal wind response to a future SIT-only loss experiment (ΔSIT) compared with the SIC-SIT-loss experiment used in this study (ΔNET). Despite the much smaller forcing in ΔSIT, there is also a robust weakening of the polar vortex under QBO-E (Figure 4.5b). Further, the evolution of the daily time series fields for ΔSIT (not shown) are remarkably similar to those in Figure 4.4. Therefore, the response to Arctic sea-ice loss is highly non-linear, and the modulating role by the QBO may also intervene with smaller sea ice loss, although with weaker forcing internal variability cannot be ruled out. Note that the mechanisms leading to the influence of the QBO on the climatological stationary wave pattern are still under investigation.

Such strong dependence to seemingly minor changes in the experiment protocol suggests the importance of the model mean state regarding its sensitivity to sea-ice anomalies. Along with other parameters that influence the model mean state, e.g., background SST (Osborne et al., 2017; Smith et al., 2017), inconsistent representation of the QBO may lead to discrepancies among modeling studies (Overland et al., 2016; Screen et al., 2018a). In that context, it is well established that accompanying a change in phase of the QBO are changes in the mean circulation such as strength of the stratospheric polar vortex and even the character of the tropospheric jets (Kidston et al., 2015). The sensitivity that we find in the sea-ice loss

experiments is associated with QBO-phase since the sea-ice forcing is strong enough, and the number of ensemble members is great enough that we can rule out internal variability. Most models still struggle to produce a realistic internally-generated QBO (Schenzinger et al., 2017), and our results suggest this may affect how they respond to Arctic sea ice or other boundary conditions. At this stage, we do not know whether other GCMs exhibit similar sensitivity to the QBO.

Acknowledgements

Computing support is provided through NCAR, sponsored by the National Science Foundation (NSF) (`https://doi.org/10.5065/D6RX99HX`). We thank two anonymous reviewers for their insightful comments to improve this study. CESM-LENS sea ice data are available at `http://www.cesm.ucar.edu/projects/community-projects/LENS/data-sets.html`. Outputs from the AGCM simulations are available from the corresponding author and stored on Cheyenne's High Performance Storage System long-term data archive. This study was supported by DOE grant DE-SC0019407, NOAA grant NA15OAR4310164, and NSF grants AGS-1624038 and NRT-1633631.

Chapter 5

Warm Arctic, cold Siberia pattern: role of full Arctic amplification versus sea-ice loss alone

This work is in review at *Geophysical Research Letters*.

Labe, Z.M., Y. Peings, and G. Magnusdottir (2020), Warm Arctic, cold Siberia pattern: role of full Arctic amplification versus sea-ice loss alone, under review at *Geophysical Research Letters*.

Abstract

The effect of future Arctic amplification (AA) on the extratropical atmospheric circulation remains unclear in numerous modeling studies. Using a collection of coordinated atmospheric and coupled global climate model perturbation experiments, we find an emergent relationship between the high-latitude 1000-500 hPa thickness response and an enhancement of the

Siberian High in winter. This wave number 1-like sea level pressure anomaly pattern is linked to an equatorward shift of the eddy-driven jet and a dynamical cooling response in eastern Asia. Additional simulations, where AA is imposed directly into the model domain by nudging, demonstrate how the sea-ice forcing is insufficient by itself to capture the vertical extent of the warming and by extension the amplitude of the response in the Siberian high. This study demonstrates the importance of the vertical extent of the tropospheric warming over the polar cap in revealing the "warm Arctic, cold Siberia" anomaly pattern in future projections.

5.1 Introduction

Attributing robust response in the wintertime extratropical circulation to Arctic climate change remains unresolved in both historical observations (Cohen et al., 2019) and future climate model projections (Smith et al., 2019). It is widely understood that the surface-albedo feedback, through loss of sea ice and snow cover, is only one of the important contributions to Arctic amplification (AA; Stuecker et al., 2018; Dai et al., 2019). Due to the nonlinear nature of polar feedbacks, it remains challenging to separate the relative importance of local and remote processes that result in AA (Goosse et al., 2018). While the largest AA has occurred near the surface in the zonal-mean average, there is evidence of substantial warming extending vertically into the upper troposphere in reanalysis and satellite-derived observations (Graversen et al., 2008; Screen and Simmonds, 2011; Alexeev et al., 2012; Cohen et al., 2019).

Recent warming of the lower-to-middle Arctic troposphere has been suggested to lead to a weakening of the midlatitude westerlies and increase in the amplitude of planetary waves through thermal wind arguments (e.g., Francis and Vavrus, 2015). Further, deep tropospheric warming may be important in resolving the "warm Arctic, cold Siberia" temperature

anomaly pattern (Xu et al., 2019), and there is also evidence that the Arctic-midlatitude teleconnection is sensitive to the depth of vertical warming in idealized models (Sellevold et al., 2016). While it is currently not possible to attribute forced causes to the continental cold extremes and atmospheric waviness due to the short historical record and substantial internal variability (Barnes and Screen, 2015; McCusker et al., 2016; Ogawa et al., 2018; Peings, 2019; Blackport et al., 2019; Blackport and Screen, 2020), a better understanding on the effects of AA is still needed (Cohen et al., 2019). To address future climate linkages between the Arctic and midlatitudes, many studies have performed atmospheric general circulation model (AGCM) experiments by prescribing changes in 21st century Arctic sea ice boundary conditions (e.g., Deser et al., 2010; Peings and Magnusdottir, 2014; Nakamura et al., 2016b; Sun et al., 2015; Labe et al., 2018b). However, most of these AGCM experiments have shown that warming is vertically trapped near the surface in response to sea ice forcing. This may be due to a lack of ocean coupling (e.g., Deser et al., 2015; Blackport and Kushner, 2018), not allowing sea-ice thickness (SIT) to change (Labe et al., 2018b), but also to the fact that AA is also largely driven by remote sea surface temperature (SST) changes (e.g., Screen et al., 2012; Perlwitz et al., 2015) and other climate feedbacks (Goosse et al., 2018; Park et al., 2018).

It remains an open question how important the vertical extent of the tropospheric warming is in assessing Arctic-midlatitude teleconnections from future projections of Arctic change (Xu et al., 2019). This also has implications for improving our understanding of the intermodel spread of the eddy-driven jet response in the latest Coupled Model Intercomparison Project (CMIP) projections due to the competing "tug-of-war" effects between upper troposphere tropical warming and AA (Barnes and Polvani, 2015; Zappa et al., 2018; Vavrus, 2018; Peings et al., 2018, 2019). To answer this question, we make use of a collection of large ensemble experiments that are prescribed with different levels of sea ice-forcing and AA within the framework of a single GCM. Here we focus our attention on understanding the tropospheric

pathway by which sea-ice anomalies modulate the Northern Annular Mode (NAM; Thompson and Wallace, 1998) through eddy-mean flow interactions and the excitation of Rossby waves, which can reinforce anticyclonic anomalies over Eurasia (Honda et al., 2009; Nakamura et al., 2016b). By doing so, we find an emergent relationship between anomalies of the geopotential thickness of 1000-500 hPa thickness layer over the Arctic and the response of the Siberian High. We also examine the degree of linearity in the responses to different levels of AA forcing in the GCM by nudging the temperature directly in the Arctic and maintaining the thermal anomaly throughout the simulation. The results have implications for disentangling the sensitivity of the large-scale atmospheric response to varying amounts of projected Arctic sea-ice decline from AA.

5.2 Climate model experiments and analysis

The high-top AGCM numerical experiments are implemented using the National Center for Atmospheric Research (NCAR) Whole Atmosphere Community Climate Model, version 4 (WACCM4; Marsh et al., 2013) and the Department of Energy (DOE) Energy Exascale Earth System Model, version 1 (E3SM; Golaz et al., 2019). WACCM4 includes 66 vertical levels (5.1×10^{-6} hPa, $\sim$140 km) and uses CAM4 physics. We use the specified chemistry version of WACCM4 (SC-WACCM4 Smith et al., 2014), which is cheaper in computational cost, but simulates dynamical coupling and stratospheric variability that is comparable to the interactive chemistry model version. The SC-WACCM4 experiments are run with a horizontal resolution of 1.9° latitude by 2.5° longitude and include present-day (year 2000) radiative forcings. A repeating 28-month cycle of the Quasi-biennial Oscillation (QBO) is included in the SC-WACCM4 experiments by using a nudging technique to relax the equa-

torial stratospheric winds to observed radiosonde data.

The E3SMv1 atmospheric component was developed from CAM5.3 and includes additional turbulence parameterizations and improvements to cloud and aerosol physics (Rasch et al., 2019). E3SM includes 72 vertical layers (compared to 30 in CAM5) with a model top at ∼0.1 hPa (∼60 km). We use the lower-resolution version of E3SM with a horizontal resolution of 100 km and present-day (year 2000) radiative forcings. While the model includes an internally generated QBO-like oscillation of the equatorial stratospheric wind, the period is too short, and the westerly winds are too strong (Richter et al., 2019).

5.2.1 Atmosphere-only simulations

5.2.1.1 Role of future Arctic sea ice

The first set of AGCM experiments are conducted following the Polar Amplification Model Intercomparison Project (PAMIP; Smith et al., 2019) tier 1 protocol. They consist of 100 members of 14-month (April through May of the following year) simulations with prescribed SST and sea-ice concentration (SIC) representative of future conditions, which are compared to two different sets of simulations corresponding to pre-industrial (Pi) and present-day (Pd) boundary forcing. SIT is held constant throughout the Arctic at 2 m. The Pd simulation is conducted using average SST and SIC from a 1979-2008 annual cycle climatology in HadISST1 (Rayner et al., 2003). Future sea ice fields are constructed from an ensemble of 31 CMIP5 models (Representative Concentration Pathway 8.5) representing 2°C of global warming above pre-industrial level. Similarly, Pi SIC is derived from Pi control runs of these 31 CMIP5 models (see details on the PAMIP forcing fields in Smith et al. (2019)). SST are held to Pd values, except in grid cells where SIC differs by more than 10% in Pi/future

experiments (Screen et al., 2013; Peings and Magnusdottir, 2014). To isolate the effect of SIC in each model, we take the difference of the future experiment minus Pd (denoted as ΔWACCM-SIC-Pd or ΔE3SM-SIC-Pd) and Pi (denoted as ΔWACCM-SIC-Pi or ΔE3SM-SIC-Pi).

An additional set of experiments using SC-WACCM4 are conducted to include the effects of SIT decline between future and Pd conditions (denoted at ΔWACCM-SIT-Pd). For fields of SIT, Pd conditions are taken from the Pan-Arctic Ice Ocean Modeling and Assimilation System, version 2.1 (PIOMAS; Schweiger et al., 2011), and future conditions are taken from the ensemble of the 31 CMIP5 models. SST and SIC fields follow the same protocol as previously described for ΔWACCM-SIC-Pd.

Finally, we compare the PAMIP experiments, which consider future warming conditions of 2°C, to an experiment with a stronger sea ice forcing (denoted as ΔNET). This SC-WACCM4 experiment isolates the role of sea-ice loss in the late 21st century (2051-2080 minus 1976-2005) using forcing fields from the mean of 40 ensemble members in the Community Earth System Model Large Ensemble (LENS; Kay et al., 2015). More details about this experiment can be found in Labe et al. (2018b, 2019).

5.2.1.2 Role of AA

To quantify the effect of sea ice-only forcing in AA, we use three experiments of SC-WACCM4 where AA is directly imposed in the model domain by nudging - corresponding to the projected state of the Arctic in 2030, 2060 and 2090 (Peings et al., 2019). A 51-year control simulation is conducted using a repeating cycle of SST and SIC taken from the 1979-2008

climatology in HadISST1. To assess the influence of AA, three perturbation experiments are conducting using a regional nudging within the Arctic ($> 70°$N) in the lower troposphere (up to to 600 hPa) to temperature fields representing conditions in the early (2020-2039), middle (2050-2069), and late (2080-2099) 21st century within the mean of 40 ensemble members from LENS. To isolate the effect of AA, we take the difference between the perturbation experiments and the control (denoted as ΔAA-2030, ΔAA-2060, ΔAA-2090). Details and validation of the nudging protocol can be found in Peings et al. (2019).

5.2.2 Atmosphere-only transient simulations

To compare our SC-WACCM4 simulations with observations, we utilize two transient AGCM experiments with 10 ensemble members each. The first simulation follows the standard Atmospheric Model Intercomparison Project II protocol (AMIP; Taylor et al., 2000) with monthly SST and SIC variability over the 1979 to 2016 period. SIT is prescribed to 2 m. This experiment is denoted as ΔAMIP. In a second transient simulation (denoted as ΔAMIP-HL), we follow the same set-up as ΔAMIP, but instead apply a nudging scheme (as in Section 2.1.2) to the Arctic Circle ($> 65°$N) lower troposphere (up to 300 hPa). In that domain, temperature, horizontal winds, and surface pressure are nudged observed 3-hour anomalies, superimposed on the model 3-hour climatology. This way we prescribed the observed variability of the atmosphere in high-latitudes while retaining the model mean state. The 3-hour observed anomalies are from the NASA's Modern-Era Retrospective Analysis for Research and Applications, version 2 (MERRA2; Gelaro et al., 2017). We compare ΔAMIP and ΔAMIP-HL to monthly observations from the National Centers for Environmental Prediction/National Center for Atmospheric Research reanalysis project (NCEP/NCAR R1; Kalnay et al., 1996) and the European Centre for Medium-Range Weather Forecasts (ECMWF) next-generation

reanalysis ERA5 (Hersbach and Dick, 2016).

5.2.3 Coupled atmosphere-ocean simulations

We consider a set of coupled experiments to compare the short-term (S) effects of ocean coupling on the atmospheric response to Arctic sea-ice loss. In this experiment (denoted as ΔS-Coupled-Pi or ΔS-Coupled-Pd), each SC-WACCM4 ensemble member is run for 14 consecutive months (April through May of the following year) with an interactive ocean and follows the same PAMIP forcing for Pi, Pd, and future sea-ice conditions. To have similar sea-ice fields as in the AGCM simulations (see section 2.1.1), SIT is nudged to its prescribed value in the AGCM runs, i.e., 2 m.

5.2.4 Statistical testing

A summary of the experiments used in our study can be found in Table A.2. Here we focus our analysis on the boreal winter (DJF; December-January-February) when the ensemble mean atmospheric response to Arctic sea-ice decline is found to be the largest (e.g., Deser et al., 2010; Blackport and Screen, 2019). We use a two-sided Student's t test and control for field significance using the false discovery rate (FDR; Wilks, 2016). A response is considered statistically significant if the FDR-adjusted p-value is less than 0.05, unless otherwise stated.

5.3 Results

Figure 5.1 shows the DJF near-surface (2-m) air temperature response in the AA (top row) and Pd sea ice-forcing PAMIP experiments (bottom row). There is a nearly-uniform warming over the Arctic Ocean in response to the AA forcing (Figure 5.1a-c). The ΔAA-2090 warm anomalies range from more than 10°C over the central Arctic to only 1-3°C over parts of North America, as far south as around 45°N latitude (Figure 5.1c). Thus, even under the late 21st century AA-forcing, the thermodynamic warming remains mostly confined to the polar cap. However, a small cooling response (down to ~ -2°C) is revealed in eastern Asia in ΔAA-2060. This cooling is amplified in ΔAA-2090 with negative temperature anomalies (down to ~ -4°C) expanding westward across Siberia.

Similar to ΔAA-2060, the warming response to sea-ice loss in the short-coupled experiment (ΔS-Coupled-Pd) is uniform across the Arctic Ocean (Figure 5.1e). Without ocean coupling, the near-surface temperature response is greatest in the outer marginal seas (e.g., Barents-Kara Seas) in direct association with the sea ice forcing (Figure 5.1d,f). This suggests that even on short time-scales, ocean feedbacks may contribute to further high latitude warming in the Arctic (e.g., north of 75°N latitude). However, this is not the case with the land temperature response, which is meridionally confined to the Arctic within the PAMIP experiments (Figure 5.1d-f). Again, we find a small patch of cooling over eastern Asia in the ΔS-Coupled-Pd and ΔSIT-Pd experiments. This "warm-Arctic, cold Siberia" pattern is in agreement with earlier studies (e.g., Mori et al., 2014, 2019; Peings and Magnusdottir, 2014; Nakamura et al., 2015; Labe et al., 2018b) and can be linked to a strengthening of the Siberian High (Sun et al., 2015; Screen et al., 2015; Labe et al., 2019). The dynamically-induced cooling results from cold air advection in association with a strengthening of the Siberian High. This is consistent with northerly meridional wind anomalies found near the surface over Eurasia in our experiments (not shown). Overall, despite differences in magni-

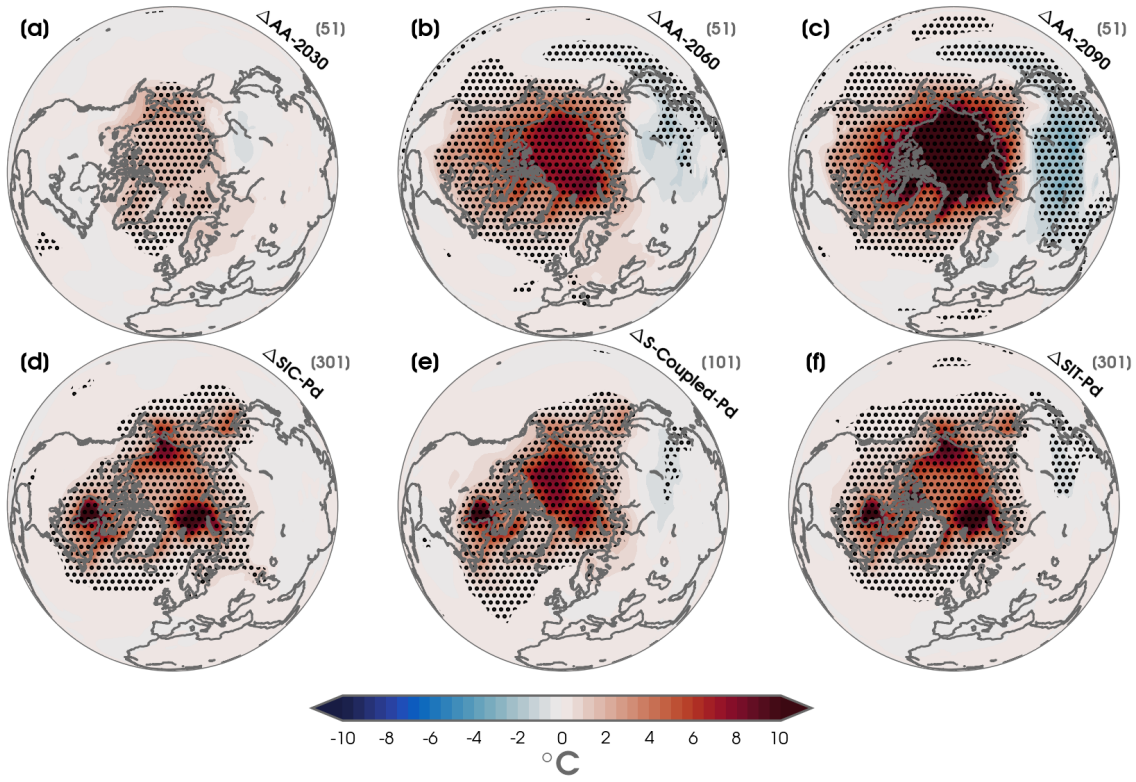

Figure 5.1: (a) Boreal winter (December-February) 2-m air temperature anomalies (interval of 0.5°C) for ΔAA-2030. (b) Same as (a) but for ΔAA-2060. (c) Same as (a) but for ΔAA-2090. (d) Same as (a) but for ΔSIC-Pd. (e) Same as (a) but for ΔS-Coupled-Pd. (f) Same as (a) but for ΔSIT-Pd. Statistically significant anomalies are overlaid with black stippling at the 95% confidence level after adjusting for FDR. The number of ensemble members for each experiment is listed in the upper right-hand corner in gray.

tude, we find strikingly similar patterns of temperature response in SC-WACCM4 in the sea ice-forcing (coupled/uncoupled) and AA experiments.

As with the 2-m air temperature response, the sea level pressure (SLP) response in the ΔAA-2030 experiment is weaker and statistically insignificant (Figure 5.2a). However, a different picture emerges with stronger AA forcing. The response in ΔAA-2060 (Figure 5.2b) is robust and characterized by higher SLP anomalies stretching from Greenland to Eurasia and lower SLP anomalies over the central Arctic Ocean and in the vicinity of the Aleutian

Low. This dipole pattern of SLP anomalies resembles a zonal wave number 1-like pattern and is further amplified in ΔAA-2090 (Figure 5.2c). The circulation response exhibits an equivalent barotropic structure over the North Pacific and North Atlantic. However, the response is baroclinic over the Arctic Ocean with positive anomalies of geopotential heights at 500 hPa (Z500) resembling a negative phase of the NAM (not shown). The pattern of SLP anomalies in ΔAA-2060 and ΔAA-2090 is also quite similar to that of ΔNET (Figure 5.2c in Labe et al. (2018b)). The response to increasing levels of AA forcing reinforces the wave-1 SLP pattern and suggests that the large-scale circulation response may be linear.

In contrast, we find a much weaker SLP response to the Pd sea-ice forcing in the three PAMIP experiments (Figure 5.2d-f). Decreases in SLP are found in the vicinity of the SIC anomalies (compare with Figure 5f in Smith et al. (2019)) and over the Hudson Bay. We also find an increase in SLP over Eurasia, albeit weaker than ΔAA-2060. The greatest SLP response is in the combined SIC and SIT-forcing experiment (ΔSIT-Pd). The robustness of this stronger response was tested by adding additional ensemble members for a total ensemble size of 300 (compared to the recommended 100 in PAMIP protocol). This result is in agreement with Labe et al. (2018b) indicating that loss of SIT reinforces the large-scale atmospheric response to SIC anomalies (Figure 5.2d). Although there are substantial differences in magnitude, the pattern of the wintertime SLP response in the coupled (Figure 5.2e) and uncoupled sea ice-forcing experiments (Figure 5.2d,f) still resembles the wave-1 response found in ΔAA-2060 and ΔAA-2090.

We now turn to vertical cross-sections of the zonal-mean temperature response to better understand the differences in magnitude of the surface response. Figure 5.3 shows the zonal-mean temperature response as a function of height (pressure) for each of the experiments. Statistically significant warming extends up to 500 hPa in ΔAA-2060 (Figure 5.3b) and up

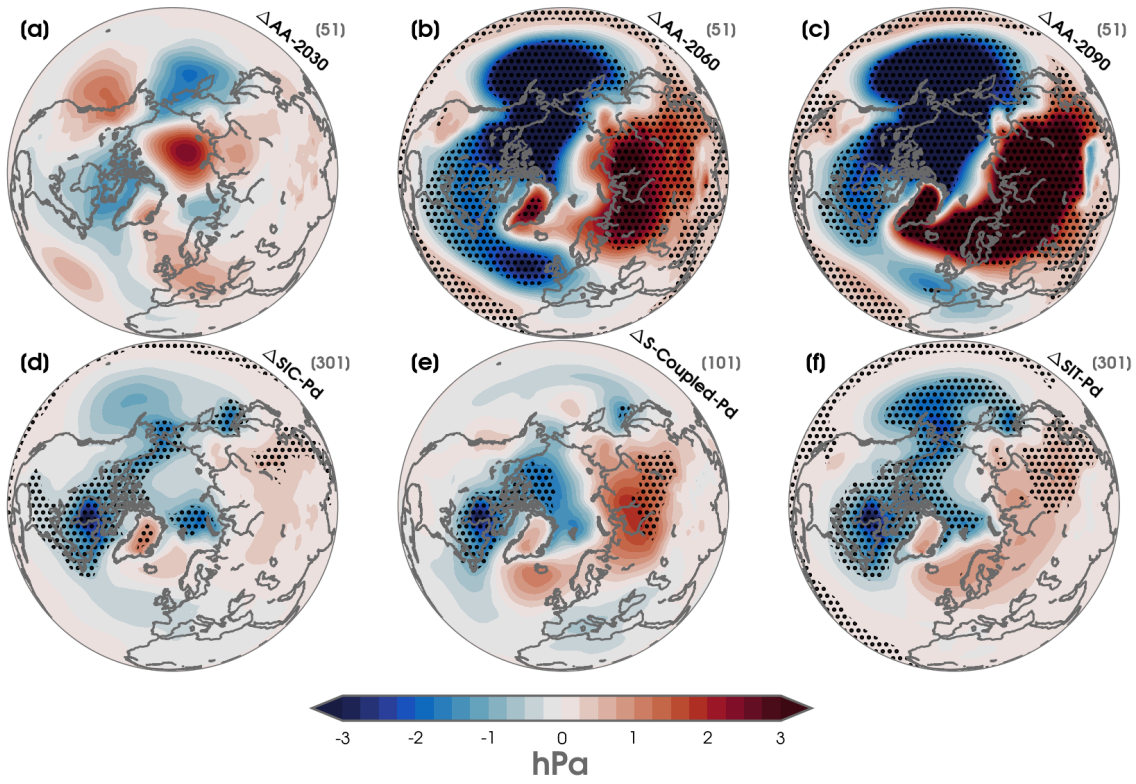

Figure 5.2: Same as Figure 5.1, but for the mean sea level pressure response (interval of 0.25 hPa) in each experiment.

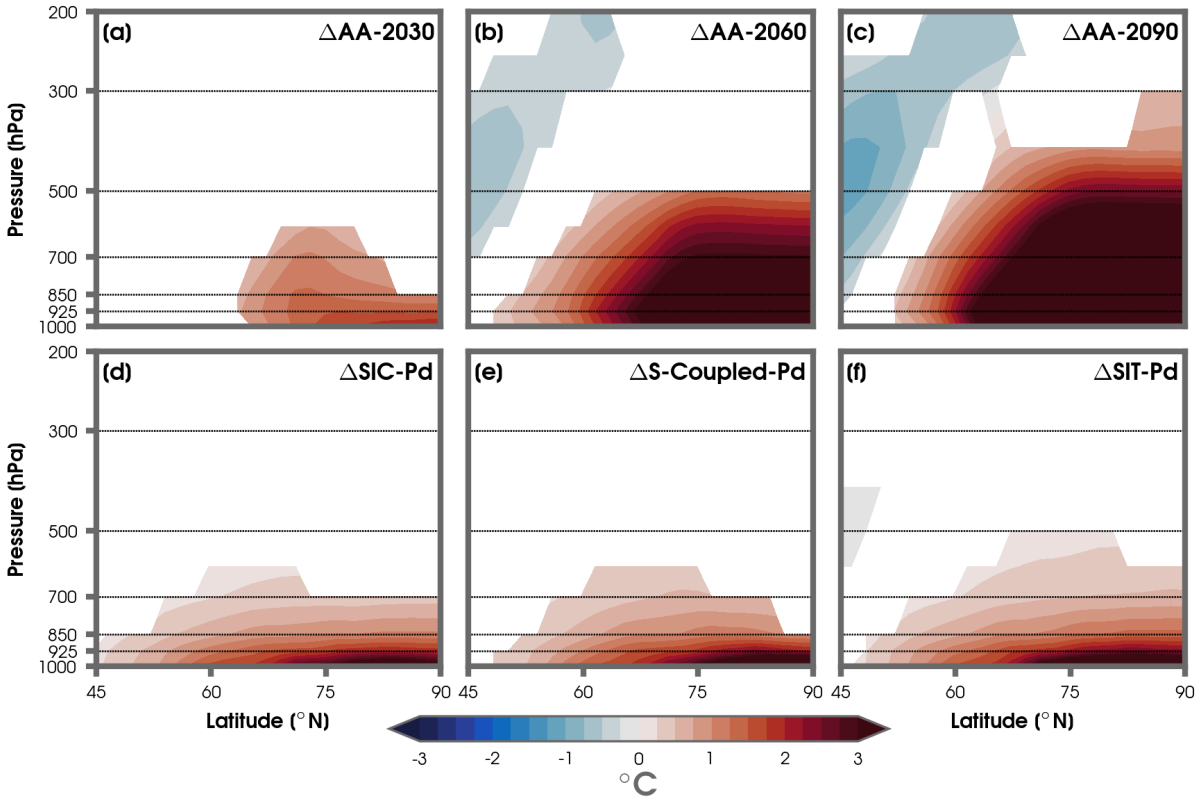

Figure 5.3: (a) Average December-February zonal-mean air temperature anomalies (interval of 0.25°C) as a function of height (pressure) for ΔAA-2030. (b) Same as (a) but for ΔAA-2060. (c) Same as (a) but for ΔAA-2090. (d) Same as (a) but for ΔSIC-Pd. (e) Same as (a) but for ΔS-Coupled-Pd. (f) Same as (a) but for ΔSIT-Pd. Shading is only shown for statistically significant responses after controlling for FDR at the 95% confidence level.

to 300 hPa in ΔAA-2090 (Figure 5.3c) within the Arctic. Recall that the nudging only extends to 600 hPa. In contrast, vertical warming is much smaller and confined to the lower troposphere within the sea ice-forcing experiments (Figure 5.3d-f). Warming reaches up to 500 hPa due to both SIT and SIC loss (ΔSIT-Pd), but only up to about 700 hPa in the SIC-only forced experiment (ΔSIC-Pd).

To contrast this simulated vertical warming with recent observations, we compare cross-sections of the zonal-mean temperature difference in the most recent decade (2010-2019) minus the first decade of the satellite-era record (1988-1979) in Figure A.17. The last decade

(2010-2019) overlaps with an observed period of substantial AA (Cohen et al., 2019). There is close agreement in the structure of vertical warming between ERA5 and NCEP/NCAR R1 datasets with statistically significant warming extending up to 300 hPa above portions of the Arctic. The largest warming is found in the lower troposphere (up to 850 hPa) and poleward of 75°N latitude. While we cannot rule out internal variability, this suggests that the sea ice-only forcing experiments do not capture key processes that are important for AA in the middle-to-upper troposphere (Perlwitz et al., 2015; Francis, 2017).

Figure A.18 compares the response of the 1000-500 hPa thickness layer between the AA and PAMIP experiments. As expected, the largest tropospheric thickness increases (>40 m) are found in simulations with the highest vertical extent of warming in Figure 5.3. This reveals a uniform increase in thickness over the Arctic Ocean in ΔAA-2060 (Figure A.18b) and ΔAA-2090 (Figure A.18c) due to AA forcing. We also find a decrease in thickness extending from the North Pacific to Siberia in association with troughing and surface cooling downstream of the Siberian High. The spatial pattern of tropospheric thickness anomalies is consistent in the sea ice-forcing experiments, although the change is smaller in magnitude (Figure A.18d-f). The largest increases in thickness are found over the Hudson Bay and the Barents-Kara Seas. Moreover, the only statistically significant decrease in thickness is found in ΔSIT-Pd over Siberia (Figure A.18f).

To evaluate the dynamical effect of a reduction in the meridional tropospheric thickness gradient, we plot the monthly mean response of the eddy-driven jet in Figure A.19. In all experiments, we find a weakening on the poleward flank of the eddy-driven jet from October through March. However, this weakening of the 700-hPa zonal wind (U700) is only statistically significant in the ΔAA-2060 (Figure A.19b), ΔAA-2090 (Figure A.19c), and ΔSIT-Pd (Figure A.19f) experiments and is largest over eastern Siberia (not shown). In addition to

the weakening, there is an equatorward shift of the eddy-driven jet with positive anomalies of U700 around 40°N latitude, especially in ΔAA-2060 and ΔAA-2090. The positive anomalies of U700 are mostly insignificant in the ΔSIT-Pd experiment. In general, the magnitude of the U700 response to 2°C of sea ice-forcing is small relative to climatology and internal variability (Figure A.19d-f). Note that there are again similarities in the pattern of U700 anomalies between experiments despite the differences in forcing, number of ensemble members, and model set-up.

Some studies have pointed to the role of the stratosphere in linking the Siberian cooling pattern to Arctic sea-ice anomalies (e.g., Cohen et al., 2019; Kim et al., 2014; Peings and Magnusdottir, 2014; Sun et al., 2015; Zhang et al., 2018a; Labe et al., 2019). However, we do not find that to be the case for the PAMIP experiments in response to the relatively small sea ice-forcing at 2°C of future climate warming. Figure A.20 shows the geopotential height response at 50 hPa (Z50) for the AA and sea ice-forcing experiments. We do not find any robust Z50 response in the stratosphere for the sea ice experiments (Figure A.20d-f) or for ΔAA-2030 (Figure A.20a). However, in response to greater AA, we do find an increase in Z50 heights over the polar cap in association with a warming of the stratospheric polar vortex. This weakening of the polar vortex may be linked to the greater equatorward shift of the eddy-driven jet found in Figure A.19b-c (Peings et al., 2019).

We refine our understanding of the wintertime relationship between the vertical warming of the mid-troposphere to the response of the Siberian High by using an emergent constraints-like approach (e.g., Hall et al., 2019) in Figure 5.4. In this assessment, we consider additional coupled and uncoupled SC-WACCM4 experiments along with AGCM simulations using E3SM. Further, we use two transient atmosphere-only experiments (ΔAMIP and ΔAMIP-HL) by considering the difference in their first and last 10-year epochs (2016-2007 minus

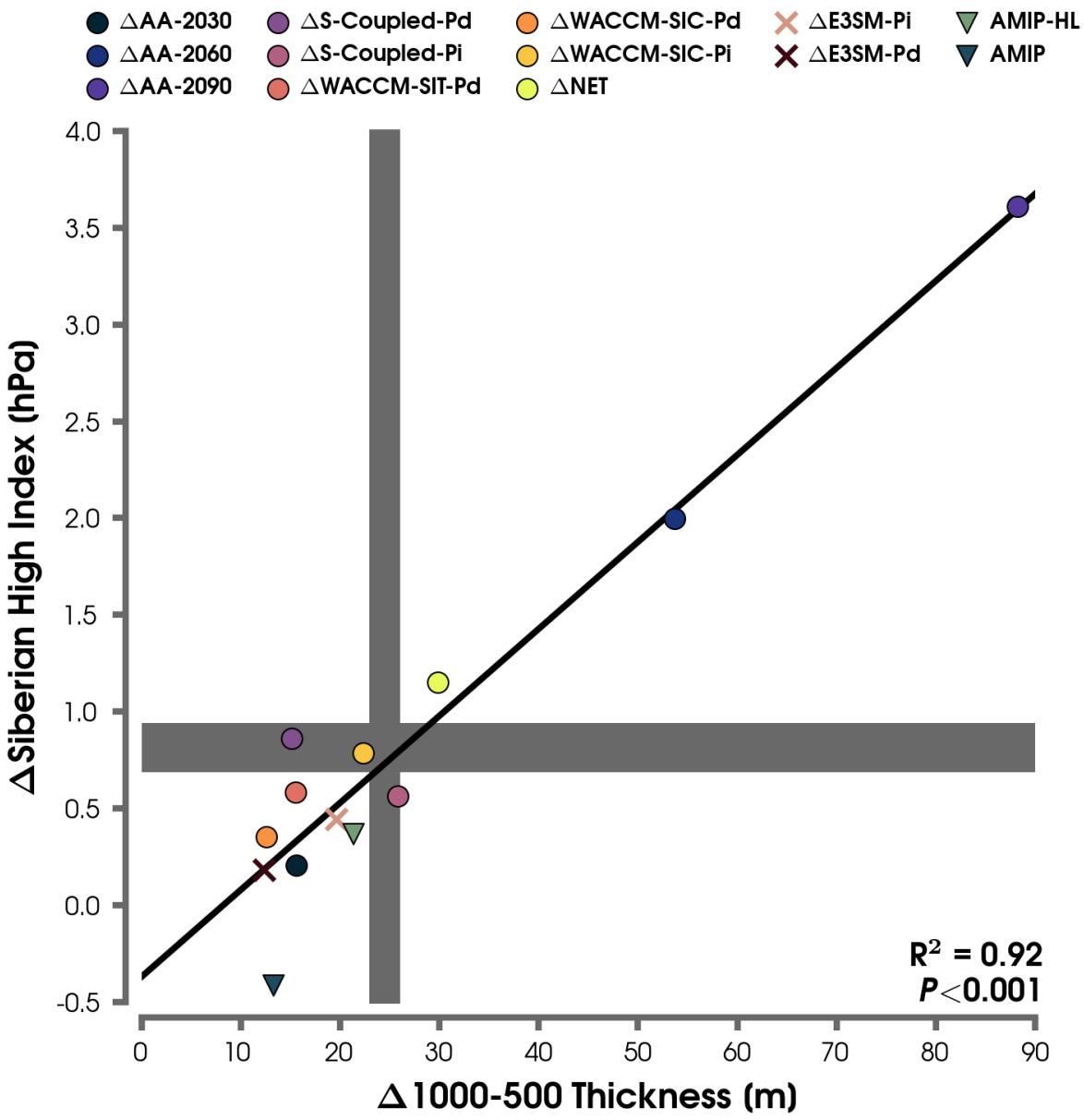

Figure 5.4: Dependence of the Siberian High Index on the 1000-500 hPa layer thickness response averaged over the polar cap (>65°N) for the boreal winter (December-February). Responses for the coupled and uncoupled experiments in SC-WACCM4 are shown with circular points. The responses in the AMIP-style (SC-WACCM4) simulations are shown with downward triangles. The responses in E3SM are indicated by X marks. Gray shading indicates the range in 1000-500 hPa layer thickness anomalies (vertical bar; 2019-2010 minus 1988-1979) and for the Siberian High Index (horizontal bar; 2019-2010 minus 1988-1979) between ERA5 and NCEP/NCAR R1. The black line shows the linear (least squares) fit after taking into consideration all of the climate model experiments.

1988-1979). We find a highly positive linear correlation ($R^2 = 0.92$; $p < 0.001$) between the response of the 1000-500 hPa thickness layer over the polar cap (weighted average north of 65°N latitude) and the Siberian High Index (weighted average over 40-65°N and 80-120°E; Panagiotopoulos et al. (2005)) after considering all of the experiments irrespective of forcing, model, or model-setup (black line). Lastly, we compare this modeled linear relationship with 10-year epoch differences (2010-2019 minus 1988-1979) in reanalysis data using gray shading to represent the range between ERA5 and NCEP/NCAR R1 (Figure 5.4). While these 10-year epochs are too short to make attribution statements on a forced response, due to decadal and multidecadal internal variability, they add confidence to the interpretation of this Siberian High relationship with increases in tropospheric thickness over the polar cap. Unsurprisingly, with a larger sea ice-forcing (Pi compared to Pd), we find more warming and a stronger response of the Siberian High (ΔWACCM-SIC-Pi and ΔE3SM-SIC-Pi).

Since ΔNET is forced with late 21st century SIC and SIT boundary conditions from LENS using SC-WACCM4 (Labe et al., 2018b, 2019), we can compare this experiment with the nudging experiments that reflect the total large-scale atmospheric response to AA. We find that both the mid-tropospheric warming and Siberian High responses are much smaller in ΔNET (see also Table A.2). This further illustrates the importance of the other feedbacks contributing to vertical warming in the Arctic, rather than only surface forcing from sea ice boundary conditions.

We note that ΔAMIP is an outlier relative to the other experiments. However, we can compare ΔAMIP to ΔAMIP-HL, which nudges the high latitudes to observed tropospheric air temperatures (up to 300 hPa). ΔAMIP-HL is warmer in the lower-to-middle troposphere and is in closer agreement to the reanalysis data sets (grey shading) and modeled linear relationship (black line) in Figure 5.4. This supports earlier studies (e.g., Perlwitz et al.,

2015) that the ensemble mean response in AMIP-style experiments, with observed SST and SIC variability, does not capture the total AA-effect found in recent reanalysis, especially in the mid-troposphere.

5.4 Conclusions

In summary, we use an extensive number of large ensemble perturbation experiments with different combinations of sea ice forcing and AA to understand the relationship between Arctic warming and Siberian cooling in boreal winter. We find that the vertical extent of warming into the middle-troposphere over the Arctic is important for revealing this surface temperature anomaly pattern. Using an integrated approach, we find that an increase in the 1000-500 hPa thickness layer over the polar cap is associated with a strengthening of the Siberian High. The emergence of a zonal wave number 1 SLP anomaly pattern and weakening on the poleward flank of the eddy-driven jet are also closely linked to the magnitude of warming in the middle-troposphere. Using a novel set of nudging experiments, we also show that this SLP pattern is reinforced with increasing levels of future AA. Moreover, the cooling response over Eurasia is also enhanced with greater AA (not considering other greenhouse gas forcing) and occurs downstream of the Siberian High anomaly due to cold air advection. Warming is vertically trapped near the surface in experiments prescribed with changes in Arctic sea ice, and increasing sea-ice loss is not enough to get the full flavor of the influence of AA in the midlatitudes. Therefore, sea ice perturbation experiments can miss important effects of AA on the large-scale extratropical circulation. Overall, the dynamical response to the PAMIP sea ice forcing at 2°C is small and non-robust relative to internal variability when compared with present-day conditions. This low signal-to-noise ratio will

be the subject of future work.

Our results are consistent with Xu et al. (2019), which found that the vertical extent warming over the Barents-Kara Seas can help resolve differences in the strength of Arctic-midlatitude linkages in historical simulations. While we primarily make use of one model (SC-WACCM4), we find that atmospheric thickness is also closely coupled to the Siberian High response in E3SM (Figure 5.4). Our results, in conjunction with Xu et al. (2019), contribute further evidence to the importance of understanding how CMIP6 models simulate the vertical structure of tropospheric warming when assessing future Arctic-midlatitude linkages in wintertime.

Acknowledgements

This project was supported by DOE Grant DE-SC0019407 and NSF Grant AGS-1624038. We also acknowledge high-performance computing support for SC-WACCM4 from Cheyenne (doi:10.5065/D6RX99HX) provided by NCAR's Computational and Information Systems Laboratory, sponsored by the National Science Foundation. E3SM simulations were performed using resources from National Energy Research Scientific Computing Center, a U.S. Department of Energy Office of Science User Facility. Figures were generated using Python 3.7, Matplotlib 3.1, and colormaps provided by Thyng et al. (2016). Sea ice fields from LENS are publicly available at http://www.cesm.ucar.edu/projects/community-projects/. Model data from the AA nudging experiments are available on Zenodo (https://zenodo.org/record/3066448). PAMIP experiment data are publicly available at https://www.earthsystemgrid.org/. Monthly reanalysis data are publicly available for NCEP/NCAR R1 (https://www.esrl.noaa.gov/psd/data/gridded/data.ncep.reanalysis.html) and ERA5 (https://climate.copernicus.eu/climate-reanalysis).

Chapter 6

Conclusions

Coinciding with a rapid warming of Arctic surface air temperature, mid-latitude regions have experienced extreme cold outbreaks during recent winters. Guided by this seeming paradox, a large body of research has hypothesized that the simultaneous warming of the Arctic and cooling across parts of the mid-latitudes are connected. However, despite recent advances in state-of-the-art climate models, statistical methods, and growing observational data networks in the Arctic, there is still no consensus on how Arctic climate change may influence mid-latitude weather and climate. Since the high-quality satellite record is only about forty years-long and affected by decadal and multi-decadal natural variability, targeted global climate model experiments are needed for disentangling causal pathways of Arctic teleconnections.

The motivation behind the dissertation was to investigate the physical mechanisms associated with the large-scale atmospheric response to projected Arctic sea-ice decline. While perturbation experiments are idealized scenarios, they provide insight to mechanisms found within fully-coupled global climate model experiments. Here, I primarily focus on the impor-

tance of the boundary condition forcing and the background mean-state. I have shown that realistic spatial variability of Arctic sea-ice thickness (SIT), simulation of the Quasi-biennial Oscillation (QBO), and the structure of warming in the high-latitude lower-to-middle troposphere are critical features for revealing Arctic-mid-latitude linkages in climate models. These advances will help to inform society on the impacts from internal climate variability, extreme events, and future Arctic climate change.

6.1 Summary of results

In Chapter 2, I investigate the spatial and temporal variability of Arctic SIT in historical and future projections through the 21st century. I use a coupled ice-ocean model assimilation system (PIOMAS) as a reanalysis data set to compare with LENS. PIOMAS is shown to realistically reproduce the variability and long-term trends of Arctic SIT and SIV when compared to satellite-derived products (ICESat and CryoSat-2) and submarine ULS data. However, as found in other studies (e.g., Schweiger et al., 2011), PIOMAS tends to underestimate thicker sea ice and overestimate thinner sea ice. This bias is most clearly evident in the Fram Strait. Although there is substantial interannual variability, declining trends in SIT are statistically significant in all months of the year. While LENS has a tendency toward thicker sea ice in the western Arctic (up to 1 m difference) compared to PIOMAS, it reproduces similar mean trends and variability in their overlapping historical period (1979-2015). The first leading EOF mode shows two opposite-sign centers of action and closely resembles the east-west Arctic anomaly pattern. This dipole represents the Transpolar Drift Stream with sea ice motion from near the New Siberian Islands moving toward the Fram Strait. The pattern is accelerated during the positive phase of the AO. Overall, there is a reduction in September SIT variability over the 21st century in LENS. All marginal seas of the Arctic observe average September SIT falling below 0.5 m before 2080 in LENS. However, this is

last to occur along the northern coast of Greenland where a perennially thick area of sea ice remains. Internal variability contributes to an uncertainty of 10 to 20 years in LENS for the timing of regional mean SIT to fall below 0.5 m.

After evaluating the internal variability of SIT in LENS, in Chapter 3, I conduct a series of perturbation experiments to quantify the relative contributions of SIT and SIC to the large-scale atmospheric response to Arctic sea-ice decline. To assess Arctic-mid-latitude linkages, previous studies (e.g., Peings and Magnusdottir, 2014; Sun et al., 2015) have generally prescribed SIT as a constant ($\approx$ 2 m) across the entire Arctic Ocean. By forcing SC-WACCM4 with sea ice and SST boundary conditions from LENS, this study provides the first comprehensive assessment on the responses to late-21st century declines of SIT and SIC, respectively. The combined SIT and SIC forcing simulates a negative NAM-like response in boreal winter with an equatorward shift of the eddy-driven jet. In agreement with Lang et al. (2017), the 2-m temperature response from SIT loss contributes up to one third of that from SIC decline. While the dynamical contributions are much smaller from SIT, they reinforce the SIC response in the lower-to-middle troposphere (e.g., Z500). Although there is little to no role of the stratosphere in the combined SIT and SIC forcing experiment, we do find that additional regionally-forced sea ice experiments (Atlantic versus Pacific sectors) contribute a nonlinear response to the stratospheric polar vortex. This study shows that it is important to consider SIT variability when addressing the effects of sea-ice decline in climate model experiments.

In Chapter 4, I analyze the role of the QBO in modulating the wintertime atmospheric response to late-21st century Arctic sea ice. A repeating 28-month cycle of the QBO is prescribed in SC-WACCM4 by nudging the stratospheric equatorial winds to observed radiosonde data. The effect of the QBO is assessed by compositing the atmospheric responses

to sea-ice loss according to their phase of the QBO (easterly or westerly). Under QBO-E, there is a robust weakening of the stratospheric polar vortex in response to sea-ice loss. On the contrary, during QBO-W, there is a marginal strengthening of the polar vortex due to sea-ice loss. The weakening under QBO-E is driven by a reinforcement of the zonal wave number 1 pattern and anomalous vertical wave activity in the vicinity of the Ural and Siberian Highs. The weaker polar vortex reinforces the Siberian High anomaly through stratospheric-troposphere coupling, which corresponds to increases in cold extremes over eastern Asia through cold air advection. Under QBO-W, the vertical wave activity is trapped in the lower troposphere (under 300 hPa) and only results in a negative NAM-like response at the surface. The role of the QBO is also demonstrated in an additional experiment with a much smaller sea-ice forcing. This study is the first to demonstrate the statistically significant effect of the QBO background state on the atmospheric response to sea-ice anomalies.

Finally, in Chapter 5, I consider a series of coordinated coupled and uncoupled experiments from PAMIP to assess the role of sea-ice forcing relative to AA. To isolate the effect of AA, three SC-WACCM4 experiments are conducted by nudging the high-latitude troposphere to the projected state of the Arctic in 2030, 2060 and 2090 using LENS. Therefore, it is possible to assess the degree of linearity in atmospheric responses to different levels of AA forcing. In response to the sea ice-only forcing in PAMIP, the warming is vertically confined to the surface and lower troposphere (up to $\approx$ 700 hPa). In contrast, warming extends upwards to $\approx$ 300 hPa in the AA experiments. This structure of vertical warming is shown to be important for revealing a zonal wave number 1 SLP response and a robust strengthening of the Siberian High. By considering additional simulations, an emergent relationship is found between the response of the 1000-500 hPa thickness layer and the strength of the Siberian High anomaly. The stronger Siberian High response is linked to a patch of cold temperature anomalies in eastern Asia through advection. In summary, this study finds that the warming

response to sea-ice anomalies is vertically confined and may not capture the full influence of AA on mid-latitude weather and climate.

6.2 Ongoing and future work

6.2.1 Detection of signal in the large-scale circulation response to Arctic sea-ice decline

Motived by understanding the small dynamical response to 2°C of future Arctic sea-ice loss found in the PAMIP experiments from Chapter 5, this preliminary work explores the variability in large ensemble experiments. Here, I use SC-WACCM4 (Smith et al., 2014) at a horizontal resolution of 1.9° latitude by 2.5° longitude with year 2000 radiative forcings. The recommended protocol for ensemble size in PAMIP tier 1 experiments is approximately 100 ensemble members for 14-month (April through May of the following year) simulations (Smith et al., 2019). To explore the effect of ensemble size on the mean atmospheric response, several experiments are extended to 300 members. These include the response to future SIC loss compared to present-day (Pd) and pre-industrial (Pi) SIC boundary conditions (ΔWACCM-SIC-Pd and ΔWACCM-SIC-Pi, respectively). In addition, 300 ensemble members are run to explore the robustness of SIT loss from future minus Pd conditions (ΔWACCM-SIT-Pd). Future and Pi sea ice fields are taken from the multi-model mean of 31 CMIP5 models. Pd fields of SST and SIC are selected using a repeating annual cycle from the 1979-2008 mean in HadISST1, and Pd fields of SIT are taken from PIOMAS. More details about the experiment protocol can be found in Smith et al. (2019) and in Chapter 5 of this dissertation.

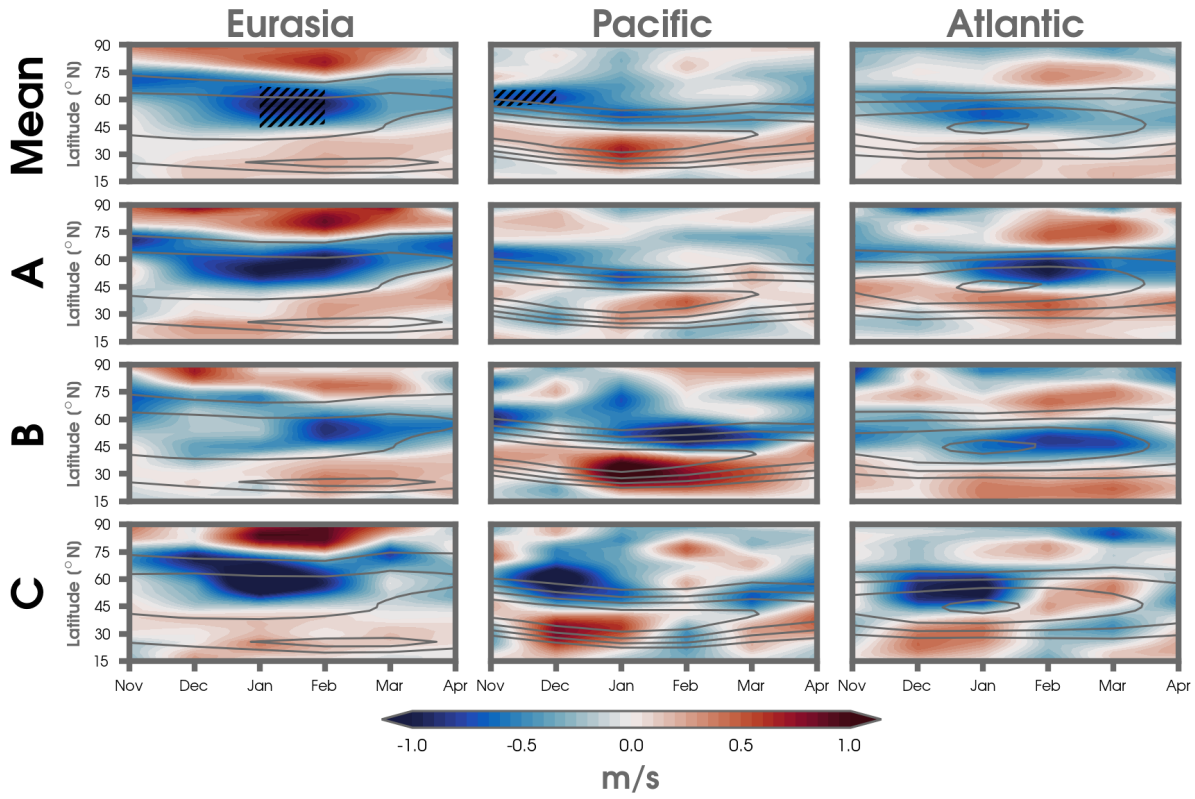

Figure 6.1: November to April anomalies of the 700-hPa zonal wind (U700) shown in shading (interval of 0.05 m/s) for the Eurasia (left column; 120°W–0°W), Pacific (middle column; 0°E–120°E), and Atlantic sectors (right column; 120°E–120°W). U700 anomalies are calculated from the ΔWACCM-SIC-Pi experiment when considering all 300 ensemble members (first row), the first 100 ensemble members (second row), the second 100 ensemble members (third row), and the third 100 ensemble members (fourth row). The gray contour lines illustrate the climatological zonal wind (3 m/s interval from 3 m/s) in each sector. Statistically significant anomalies are overlaid with black hatch marks after controlling for the FDR at the 95% confidence level.

Figure 6.1 shows the response of the eddy-driven jet seasonal cycle in ΔWACCM-SIC-Pi after compositing the 700-hPa zonal wind (U700) anomalies according to region and ensemble size. The total ensemble mean, using 300 ensemble members, is shown in the first row ("Mean") and then three unique 100-member subsets are compared in the "A," "B," and "C" rows. Overall, there is substantial variability between region and ensemble size. For example, by comparing the response in the Pacific using 100 ensembles in "B," it can be interpreted that there is an equator shift in the jet due to Arctic sea-ice loss. However, when looking at 100 members in "A," there are no robust responses of U700 from November to April. In this example, it is clear that the position and strength of the eddy-driven jet response can be interpreted differently depending on the ensemble member size of ΔWACCM-SIC-Pi.

Earlier studies (e.g., Screen et al., 2014) have suggested a minimum ensemble size of at least 50 members for detecting a signal from noise in dynamical fields. Following the methods in Screen et al. (2014), the minimum number of ensembles (N_{min}) needed to detect a statistically significant response in ΔWACCM-SIC-Pi is computed by:

$$N_{min} = 2t_c^2 \times \left(\frac{S_p}{\bar{x} - \bar{y}} \right)^2 \tag{6.1}$$

where, t_c is the Student's t-distribution for a two-tailed test at the 95% confidence interval, S_p is the pooled standard deviation, $\bar{x}$ is the ensemble mean from the future experiment, and $\bar{y}$ is the ensemble mean from the Pi experiment. Compared with Screen et al. (2014, see their Table 1), Figure 6.2 indicates that larger ensemble sizes are needed to detect signal in tropospheric ($N_{min} > 120$) and stratospheric ($N_{min} > 150$) dynamical fields on monthly time scales. It is also possible this could be due to using a different model, temporal interval, and boundary condition forcing. Unsurprisingly, much smaller ensemble sizes are needed to detect robust thermodynamic fields (e.g., 2-m temperature with $N_{min} > 60$). This is in closer agreement to the recent findings in Liang et al. (2020), which show that larger ensemble

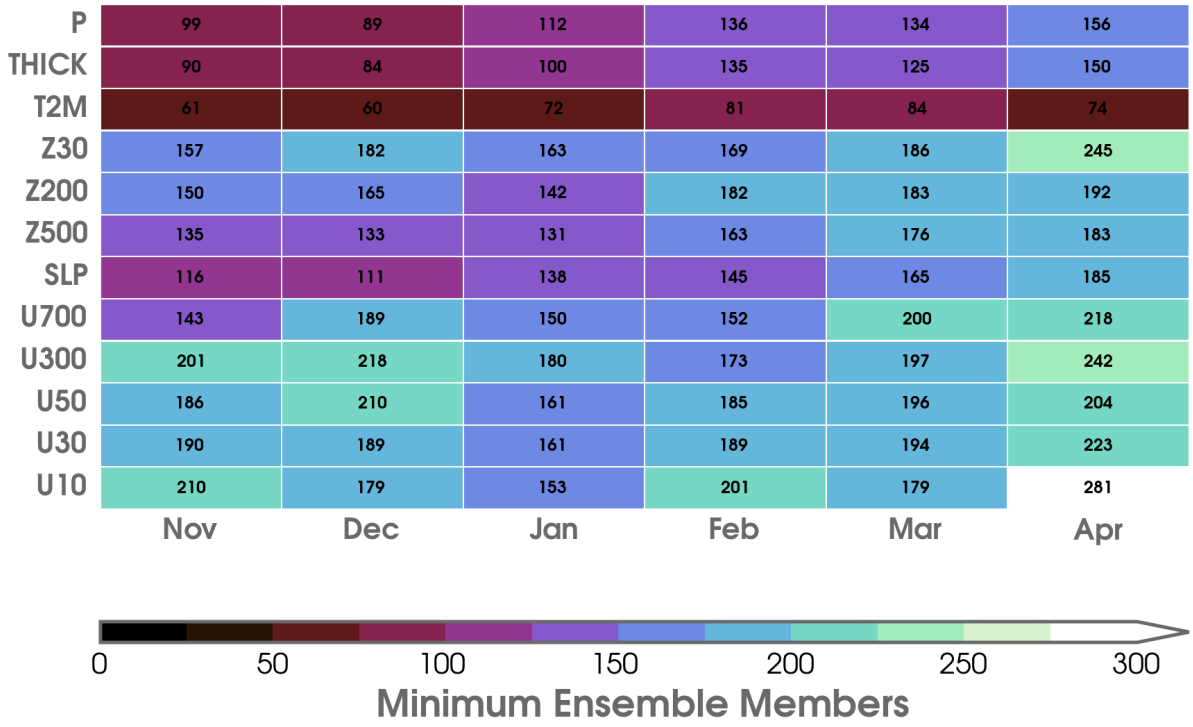

Figure 6.2: Minimum number of ensembles (N_{min}) for each month from November to April for responses of total precipitation (P), 1000-500 hPa thickness (THICK), 2-m air temperature (T2M), 30-hPa geopotential height (Z30), 200-hPa geopotential height (Z200), 500-hPa geopotential height (Z500), sea level pressure (SLP), 700-hPa zonal wind (U700), 300-hPa zonal wind (U300), 50-hPa zonal wind (U50), 30-hPa zonal wind (U30), and 10-hPa zonal wind (U10). Note that N_{min} is calculated over all grid cells with a statistically significant response at the 95% confidence interval (averaged north of 30°N) in the ΔWACCM-SIC-Pi experiment.

sizes may be needed to detect robust atmospheric responses to Arctic sea-ice loss over the 1979-2014 historical period.

To explore whether the relatively non-robust response exists using a coupled GCM, the ΔS-Coupled-Pd experiment, using SC-WACCM4, is extended to 300 ensemble members. This simulation uses the same sea-ice forcing as ΔWACCM-SIC-Pd, but with an interactive ocean. Figure 6.3 shows the geopotential height response at 500 hPa (Z500) for ΔS-Coupled-Pd by compositing over three separate 100-ensemble member periods (a, b, c). While the spatial pattern of anomaly is similar, featuring a negative NAM-like response with increases in Z500 over the Arctic Ocean, there are differences in the statistical significance of the response. Thus, the interpretation of the atmospheric response can be misleading due to substantial internal variability when only considering 100 ensemble members. Overall, this preliminary work shows that substantially larger ensemble sizes (> 150 members) may be needed to truly separate the signal from the noise in the large-scale atmospheric response to Arctic sea-ice loss under smaller forcing.

6.2.2 Potential predictability of surface forcings in historical AMIP experiments

The majority of this dissertation work has explored teleconnections in future Arctic climate change projections, especially by forcing models with large perturbations. However, there are still substantial uncertainties on the roles of Arctic sea ice and Eurasian snow cover for mid-latitude teleconnections over the historical period (Henderson et al., 2018; Cohen et al., 2019). Further, previous studies (e.g., Eade et al., 2014; Scaife and Smith, 2018) have shown the emergence of a signal-to-noise paradox in seasonal-to-decadal prediction. This is often

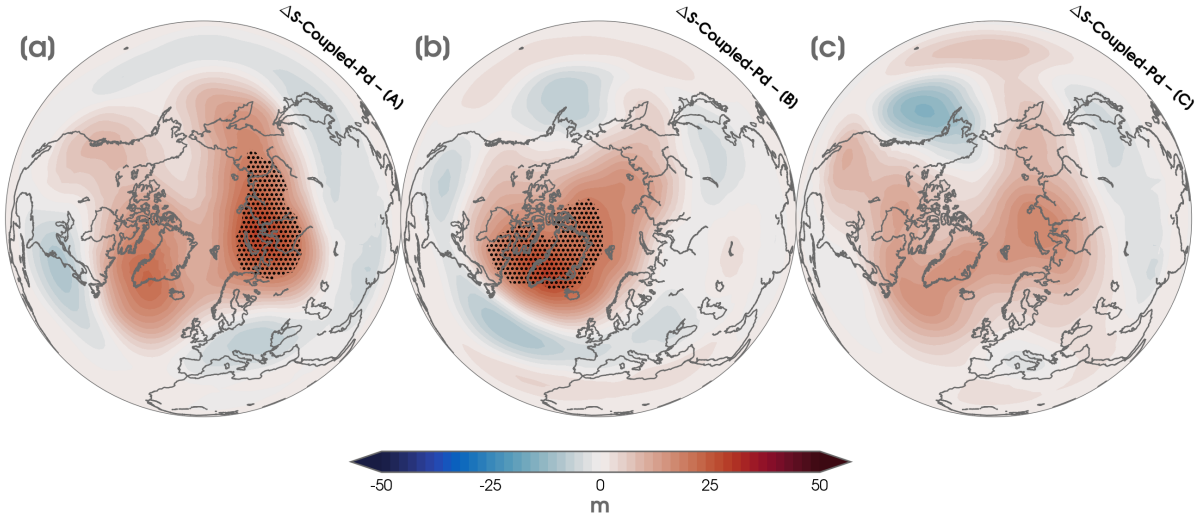

Figure 6.3: (a) Boreal winter (December-February) 500-hPa geopotential height anomalies (interval of 2 m) for the first 100 ensemble members in ΔS-Coupled-Pd. (b) Same as (a) but for the second 100 ensemble members. (c) Same as (a) but for the third 100 ensemble members. Statistically significant anomalies are overlaid with black stippling at the 95% confidence level after adjusting for FDR.

found in climate models that correlate with observed atmospheric variability better than would be expected from their low low signal-to-noise ratio, such as for teleconnections like the (N)AO (Stockdale et al., 2015; Dunstone et al., 2016; O'Reilly et al., 2019). Thus, a comprehensive analysis on the potential predictability of high-latitude surface forcing(s) is still needed using large ensemble simulations.

In the early stages of this work, I have conducted eight AMIP-like (Taylor et al., 2000) simulations using SC-WACCM4 (Smith et al., 2014). The horizontal resolution is 1.9° latitude by 2.5° longitude. The experiments have been carefully designed to address the role of different surface forcings (SST, SIC, snow cover) on Northern Hemisphere teleconnections and also to consider other possible climate influences (e.g., QBO, AA). First, a control run is launched from 1955 to 1978 with observed SST and SIC variability. The control is also prescribed with historical ozone, greenhouse gas, and aerosol concentrations. Starting in 1978, 10 ensemble members are branched from the control run using a small initial condition roundoff difference (e.g., Kay et al., 2015). Each ensemble member is run with historical greenhouse gas, aerosol, and ozone forcing to 2005 and then follow RCP4.5 from 2005 to 2016. The first year (1978) is discarded as spin-up, leaving us with transient atmosphere-only experiments over the 1979 to 2016 period. The simulations are compared to NCEP-NCAR R1 (Kalnay et al., 1996), ERA-Interim (Dee et al., 2011), and ERA5 (Hersbach et al., 2020) reanalyses.

The individual eight experiments are as follows: (1) constant SST and SIC variability (CSST), (2) constant SIC and SST variability (CSIC), (3) SST variability and SIC variability (AMIP), (4) SST variability and SIC variability, prescribed QBO (AMQ), (5) SST and SIC variability, prescribed October-November Eurasian snow (AMS), (6), SST and SIC variability, prescribed QBO and prescribed October-November Eurasian snow (AMQS), (7) SST variability and SIC variability with temperature nudging applied to the high-Arctic

(north of 70°N) troposphere (up to 600 hPa) (AMIP-AA), and (8) SST variability and SIC variability with temperature nudging applied to the entire Arctic Circle (north of 65°N) troposphere (up to 300 hPa) (AMIP-HL).

In AMQ and AMQS, the QBO is prescribed with a repeating ≈28-month cycle by relaxing equatorial (between 22°S and 22°N) stratospheric zonal winds from 86 to 4 hPa following radiosonde observations (see Hansen et al. (2013)). In AMS and AMQS, Eurasian (35°N–60°N, 40°E–180°E) snow cover is prescribed following the methods in Peings et al. (2017) with snow water equivalent observations taken from ERA-Interim/Land (Balsamo et al., 2015). In AMIP-AA and AMIP-HL, nudging is applied to 3-hourly fields of temperature, horizontal winds, and surface pressure from MERRA2 within each experiment's respective domain. Observations and mean climatologies of SIC and SST are taken from HadISST1. SIT is kept fixed to 2-m in each experiment.

Figure 6.4 shows the DJF trends of 2-m temperature over the historical period between six of the AMIP experiments compared to ERA-Interim. Warming trends are largest (> 2°C/decade) in areas of sea-ice loss, especially in the Barents-Kara Seas region. However, in agreement with earlier historical simulation studies (e.g., Perlwitz et al., 2015; Sun et al., 2016; Ogawa et al., 2018; Collow et al., 2019; Screen and Blackport, 2019b; Koenigk et al., 2019; Warner et al., 2020), there is no statistically significant forced response (e.g., "warm Arctic, cold continent" pattern) due to Arctic sea-ice variability in the AMIP-style experiments. While individual ensemble members are able to reproduce the same temperature trends as ERA-Interim, the ensemble mean response does not correlate to observed atmospheric variability over the mid-latitudes. This suggests the importance of internal variability and model mean-state in resolving the recent cooling trends over Eurasia (Sun et al., 2016). In general, simulated middle-to-upper tropospheric warming is smaller than ERA-Interim

within the Arctic. However, comparing CSIC and CSST to AMIP shows that sea-ice loss is primarily contributing to surface-based AA, while remote SST variability is found to increase warming at higher levels in the troposphere. In particular, we can see the role of sea ice in Figure 6.4 by comparing CSIC (climatological SIC) compared to the other experiments (SIC variability). Note that these results are in agreement with the findings in Chapter 5.

To further explore the forced response, signal-to-noise ratios as computed as follows:

$$SNR = \frac{|\mu|}{\sigma} \tag{6.2}$$

where, μ is defined as the ensemble mean trend (signal) and σ is the standard deviation of trends across the 10 ensemble members (noise). While there are high values of SNR (> 1) in the thermodynamic responses (e.g., 2-m temperature), there is no forced dynamical signal in the extratropical troposphere (e.g., SLP, U700, U200) or polar stratosphere (e.g., U10).

Preliminary results also suggest an improvement in the early winter pattern correlations of SLP and Z500 over the North Atlantic after including realistic snow anomalies in Siberia (as in AMS). Further, in agreement with Chapter 5, there is evidence of an improvement in the wintertime SLP and Z500 correlations over Siberia after nudging the high-latitude troposphere to observed temperatures (as in AMIP-AA and AMIP-HL). Given the unique number of combinations in this experiment protocol, these are just a few of the areas that deserve further investigation. It would also be interesting to explore case studies, such as the extreme European cold in the 2013-2014 winter (Peings and Magnusdottir, 2015) and the role of the tropospheric polar vortex split in early 2016 (Overland and Wang, 2016). This could be done by conducting additional ensemble members to target selected case study periods within each AMIP-style experiment.

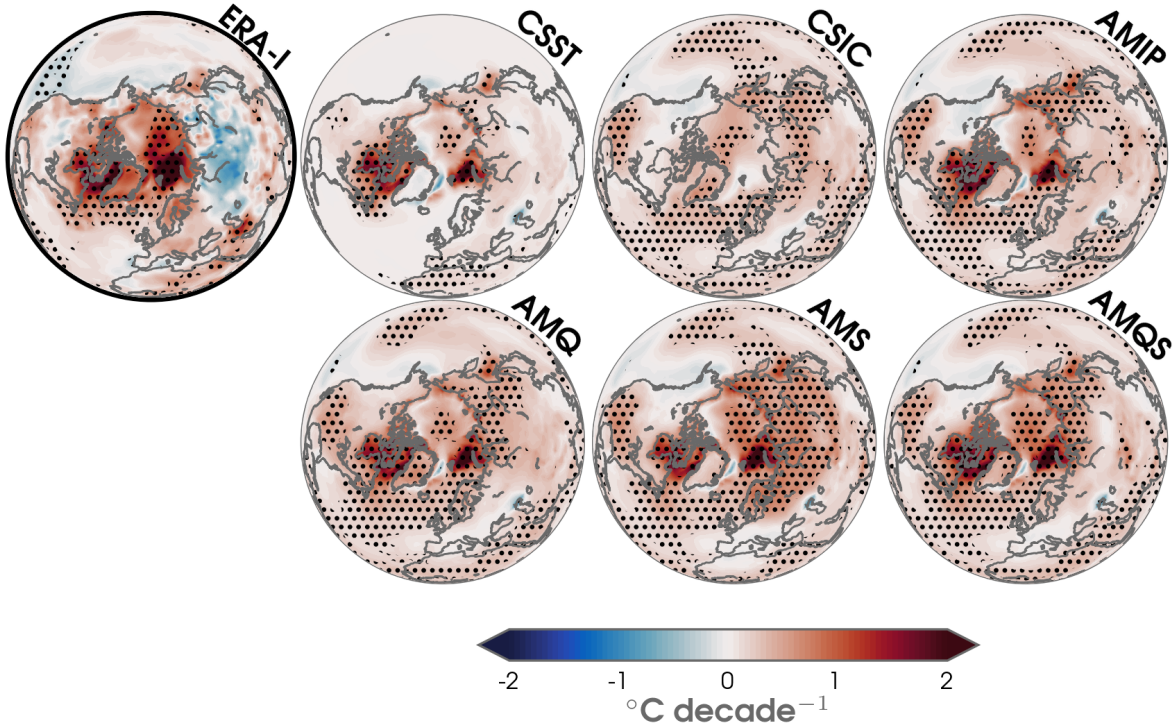

Figure 6.4: Boreal winter (December-February) linear (least squares) trends of 2-m temperature (°C/decade) over the 1979 to 2014 period for ERA-Interim (ERA-I) and six of the AMIP-like experiments (CSST, CSIC, AMIP, AMQ, AMS, AMQS). Statistically significant trends are overlaid with black stippling at the 95% confidence level following the Mann-Kendall (MK) test (Mann, 1945; Bevan and Kendall, 1971).

6.2.3 Multi-model assessment of stratospheric and tropospheric pathways of Arctic amplification teleconnections

While I have outlined new insights on teleconnections from Arctic climate change using SC-WACCM4 and LENS, which provide a realistic simulation of extratropical atmospheric dynamics (Marsh et al., 2013; Smith et al., 2014; Kay et al., 2015), a multi-model assessment is still needed in order to further explore the findings outlined in this dissertation. To date, only a few studies have compared the large-scale atmospheric responses to future Arctic sea-ice loss in coordinated multi-model assessments (e.g., Zappa et al., 2018; Screen and Blackport, 2019a). As GCM experiments continue to get submitted to CMIP6, the related Polar Amplification Model Intercomparison Project (PAMIP; Smith et al., 2019) provides an excellent opportunity to explore the effects of sea-ice loss and AA under 2°C of global warming (Rogelj et al., 2016). Moreover, there has been little work to compare the effects of AA in different large initial-condition ensembles. This can now be addressed using the new multi-model large ensemble archive and data repository, organized by US Climate Variability and Predictability (CLIVAR) (Deser et al., 2020).

Lastly, as a result of new improvements to the length of the SIT reanalysis record (Schweiger et al., 2019) and an increasing availability of satellite-derived observations (Sallila et al., 2019; Petty et al., 2020), a comparison with CMIP6 models will also be beneficial in expanding the results of Chapters 2 and 3 for the role of SIT variability on Arctic-midlatitude teleconnections. In addition, a total of 15 models now simulate a QBO in CMIP6 (compared to only 5 GCMs in CMIP5) (Richter et al., 2020). This provides the opportunity to comprehensively compare the effect of QBO phase in modulating the atmospheric response to Arctic sea-ice loss (as found in Chapter 4 in SC-WACCM4). There is already preliminary evidence that the influence of the QBO may exist in other models (e.g., using the HadGEM3 Met Office Model; Eade et al., 2019). Overall, this future work will bring a better understanding on the

(non)linear tropospheric and stratospheric pathways involved in winter Arctic-midlatitude linkages (Overland et al., 2016; Screen et al., 2018a; Cohen et al., 2019).

Bibliography

Alexander, M. A., U. S. Bhatt, J. E. Walsh, M. S. Timlin, J. S. Miller, and J. D. Scott, 2004: The atmospheric response to realistic Arctic sea ice anomalies in an AGCM during winter. *Journal of Climate.* doi:10.1175/1520-0442(2004)017⟨0890:TARTRA⟩2.0.CO;2.

Alexeev, V. A., I. Esau, I. V. Polyakov, S. J. Byam, and S. Sorokina, 2012: Vertical structure of recent arctic warming from observed data and reanalysis products. *Climatic Change*, **111** (2), 215–239. doi:10.1007/s10584-011-0192-8.

Alexeev, V. A., P. L. Langen, and J. R. Bates, 2005: Polar amplification of surface warming on an aquaplanet in "ghost forcing" experiments without sea ice feedbacks. *Climate Dynamics*, **24** (7-8), 655–666. doi:10.1007/s00382-005-0018-3.

Andrews, M. B., J. R. Knight, A. A. Scaife, Y. Lu, T. Wu, L. J. Gray, and V. Schenzinger, 2019: Observed and simulated teleconnections between the stratospheric Quasi-Biennial Oscillation and Northern Hemisphere winter atmospheric circulation. *Journal of Geophysical Research: Atmospheres.* doi:10.1029/2018JD029368.

Andrews, T., J. M. Gregory, M. J. Webb, and K. E. Taylor, 2012: Forcing, feedbacks and climate sensitivity in CMIP5 coupled atmosphere-ocean climate models. *Geophysical Research Letters*, **39** (9). doi:10.1029/2012GL051607.

Anstey, J. A. and T. G. Shepherd, 2014: High-latitude influence of the quasi-biennial oscillation. *Quarterly Journal of the Royal Meteorological Society*, **140** (678), 1–21. doi:10.1002/qj.2132.

Ayarzagüena, B. and J. A. Screen, 2016: Taking the chill off: Future Arctic sea-ice loss reduces severity of cold air outbreaks in midlatitudes. *Geophysical Research Letters*, n/a–n/a. doi:10.1002/2016GL068092.

Baldwin, M. P., and Coauthors, 2001: The quasi-biennial oscillation. *Reviews of Geophysics*, **39** (2), 179–229. doi:10.1029/1999RG000073.

Baldwin, M. P. and D. W. Thompson, 2009: A critical comparison of stratosphere-troposphere coupling indices. *Quarterly Journal of the Royal Meteorological Society*, **135** (644), 1661–1672. doi:10.1002/qj.479.

Baldwin, M. P. and T. J. Dunkerton, 2001: Stratospheric harbingers of anomalous weather regimes. *Science (New York, N.Y.)*, **294** (5542), 581–4. doi:10.1126/science.1063315.

Balsamo, G., and Coauthors, 2015: ERA-Interim/Land: a global land surface reanalysis data set. *Hydrology and Earth System Sciences*, **19** (1), 389–407. doi:10.5194/hess-19-389-2015.

Barnes, E. A., 2013: Revisiting the evidence linking Arctic amplification to extreme weather in midlatitudes. *Geophysical Research Letters*, **40** (17), 4734–4739. doi:10.1002/grl.50880.

Barnes, E. A. and J. A. Screen, 2015: The impact of Arctic warming on the midlatitude jet-stream: Can it? Has it? Will it? *Wiley Interdisciplinary Reviews: Climate Change*, **6** (3), 277–286. doi:10.1002/wcc.337.

Barnes, E. A. and L. M. Polvani, 2015: CMIP5 Projections of Arctic Amplification, of the North American/North Atlantic Circulation, and of Their Relationship. *Journal of Climate*.

——, J. W. Hurrell, I. Ebert-Uphoff, C. Anderson, and D. Anderson, 2019: Viewing Forced Climate Patterns Through an AI Lens. *Geophysical Research Letters*, **46** (22), 13389–13398. doi:10.1029/2019GL084944.

Barnhart, K. R., C. R. Miller, I. Overeem, and J. E. Kay, 2015: Mapping the future expansion of Arctic open water. *Nature Climate Change*, **6** (3), 280 pp. doi:10.1038/nclimate2848.

Bevan, J. M. and M. G. Kendall, 1971: Rank Correlation Methods. *The Statistician.* doi:10.2307/2986801.

Binder, H., M. Boettcher, C. M. Grams, H. Joos, S. Pfahl, and H. Wernli, 2017: Exceptional Air Mass Transport and Dynamical Drivers of an Extreme Wintertime Arctic Warm Event. *Geophysical Research Letters*, **44** (23), 12,028–12,036. doi:10.1002/2017GL075841.

Bintanja, R., E. C. van der Linden, and W. Hazeleger, 2012: Boundary layer stability and Arctic climate change: a feedback study using EC-Earth. *Climate Dynamics*, **39** (11), 2659–2673. doi:10.1007/s00382-011-1272-1.

Bitz, C. M. and G. H. Roe, 2004: A Mechanism for the High Rate of Sea Ice Thinning in the Arctic Ocean. *Journal of Climate*, **17** (18), 3623–3632. doi:10.1175/1520-0442(2004)017⟨3623:AMFTHR⟩2.0.CO;2.

Blackport, R. and J. A. Screen, 2019: Influence of Arctic Sea Ice Loss in Autumn Compared to That in Winter on the Atmospheric Circulation. *Geophysical Research Letters*, **46** (4), 2213–2221. doi:10.1029/2018GL081469.

—— and ——, 2020: Insignificant effect of Arctic amplification on the amplitude of mid-latitude atmospheric waves. *Science Advances*, **6** (8), eaay2880 pp. doi:10.1126/sciadv.aay2880.

—— and P. J. Kushner, 2017: Isolating the Atmospheric Circulation Response to Arctic Sea Ice Loss in the Coupled Climate System. *Journal of Climate*, **30** (6), 2163–2185. doi:10.1175/JCLI-D-16-0257.1.

—— and ——, 2018: The Role of Extratropical Ocean Warming in the Coupled Climate Response to Arctic Sea Ice Loss. *Journal of Climate*, **31** (22), 9193–9206. doi:10.1175/JCLI-D-18-0192.1.

——, J. A. Screen, K. van der Wiel, and R. Bintanja, 2019: Minimal influence of reduced Arctic sea ice on coincident cold winters in mid-latitudes. *Nature Climate Change 2019*, 1–8. doi:10.1038/s41558-019-0551-4.

Blanchard-Wrigglesworth, E. and C. M. Bitz, 2014: Characteristics of Arctic Sea-Ice Thickness Variability in GCMs. *Journal of Climate*, **27** (21), 8244–8258. doi:10.1175/JCLI-D-14-00345.1.

Blthgen, J., R. Gerdes, and M. Werner, 2012: Atmospheric response to the extreme Arctic sea ice conditions in 2007. *Geophysical Research Letters.* doi:10.1029/2011GL050486.

Boisvert, L. N., A. A. Petty, and J. C. Stroeve, 2016: The impact of the extreme winter 2015/16 arctic cyclone on the Barents-Kara Seas. *Monthly Weather Review*, **144** (11), 4279–4287. doi:10.1175/MWR-D-16-0234.1.

Brodzik, M. J., B. Billingsley, T. Haran, B. Raup, and M. H. Savoie, 2012: EASE-Grid 2.0: Incremental but Significant Improvements for Earth-Gridded Data Sets. *ISPRS International Journal of Geo-Information*, **1** (3), 32–45. doi:10.3390/ijgi1010032.

Bushuk, M., R. Msadek, M. Winton, G. A. Vecchi, R. Gudgel, A. Rosati, and X. Yang, 2016: Summer enhancement of Arctic sea-ice volume anomalies in the September-ice zone. *Journal of Climate*, JCLI–D–16–0470.1. doi:10.1175/JCLI-D-16-0470.1.

Cattiaux, J., Y. Peings, D. Saint-Martin, N. Trou-Kechout, and S. J. Vavrus, 2016: Sinuosity of mid-latitude atmospheric flow in a warming world. *Geophysical Research Letters.* doi:10.1002/2016GL070309.

Cavalieri, D. J. and C. L. Parkinson, 2012: Arctic sea ice variability and trends, 1979–2010. *The Cryosphere*, **6** (4), 881–889. doi:10.5194/tc-6-881-2012.

Cohen, J., and Coauthors, 2018: Arctic change and possible influence on mid-latitude climate and weather. *US CLIVAR Report 2018-1.* doi:10.5065/D6TH8KGW.CONTRIBUTORS.

——, and Coauthors, 2014: Recent Arctic amplification and extreme mid-latitude weather. *Nature Geoscience*, **7** (9), 627–637. doi:10.1038/ngeo2234.

——, D. Coumou, J. Hwang, L. Mackey, P. Orenstein, S. Totz, and E. Tziperman, 2019: S2S reboot: An argument for greater inclusion of machine learning in subseasonal to seasonal forecasts.

Collow, T. W., W. Wang, and A. Kumar, 2019: Reduction in Northern Midlatitude 2-m Temperature Variability due to Arctic Sea Ice Loss. *Journal of Climate*, **32** (16), 5021–5035. doi:10.1175/JCLI-D-18-0692.1.

Coumou, D., G. Di Capua, S. Vavrus, L. Wang, and S. Wang, 2018: The influence of Arctic amplification on mid-latitude summer circulation.

Dai, A., D. Luo, M. Song, and J. Liu, 2019: Arctic amplification is caused by sea-ice loss under increasing CO 2. *Nature Communications*, **10** (1), 1–13. doi:10.1038/s41467-018-07954-9.

Dawson, A., 2016: eofs: A Library for EOF Analysis of Meteorological, Oceanographic, and Climate Data. *Journal of Open Research Software*, **4** (1). doi:10.5334/jors.122.

Dee, D. P., and Coauthors, 2011: The ERA-Interim reanalysis: configuration and performance of the data assimilation system. *Quarterly Journal of the Royal Meteorological Society*, **137** (656), 553–597. doi:10.1002/qj.828.

Deser, C., A. Phillips, V. Bourdette, and H. Teng, 2012: Uncertainty in climate change projections: the role of internal variability. *Climate Dynamics*, **38** (3-4), 527–546. doi:10.1007/s00382-010-0977-x.

Deser, C., and Coauthors, 2020: Insights from Earth system model initial-condition large ensembles and future prospects. *Nature Climate Change*, 1–10. doi:10.1038/s41558-020-0731-2.

Deser, C., G. Magnusdottir, R. Saravanan, and A. Phillips, 2004: The Effects of North Atlantic SST and Sea Ice Anomalies on the Winter Circulation in CCM3. Part II: Direct and Indirect Components of the Response. *Journal of Climate*, **17** (5), 877–889. doi:10.1175/1520-0442(2004)017⟨0877:TEONAS⟩2.0.CO;2.

——, R. A. Tomas, and L. Sun, 2015: The Role of Ocean–Atmosphere Coupling in the Zonal-Mean Atmospheric Response to Arctic Sea Ice Loss. *Journal of Climate.*

——, R. Tomas, M. Alexander, and D. Lawrence, 2010: The Seasonal Atmospheric Response to Projected Arctic Sea Ice Loss in the Late Twenty-First Century. *Journal of Climate*, **23** (2), 333–351. doi:10.1175/2009JCLI3053.1.

Ding, Q., and Coauthors, 2019: Fingerprints of internal drivers of Arctic sea ice loss in observations and model simulations. *Nature Geoscience*, **12** (1), 28–33. doi:10.1038/s41561-018-0256-8.

——, and Coauthors, 2017: Influence of high-latitude atmospheric circulation changes on summertime Arctic sea ice. *Nature Climate Change.* doi:10.1038/NCLIMATE3241.

Döscher, R. and T. Koenigk, 2013: Arctic rapid sea ice loss events in regional coupled climate scenario experiments. *Ocean Science*, **9** (2), 217–248. doi:10.5194/os-9-217-2013.

Dunstone, N., D. Smith, A. Scaife, L. Hermanson, R. Eade, N. Robinson, M. Andrews, and J. Knight, 2016: Skilful predictions of the winter North Atlantic Oscillation one year ahead. *Nature Geoscience*, **9** (11), 809–814. doi:10.1038/ngeo2824.

Eade, R., D. Smith, A. Scaife, E. Wallace, N. Dunstone, L. Hermanson, and N. Robinson, 2014: Do seasonal-to-decadal climate predictions underestimate the predictability of the real world? *Geophysical Research Letters*, **41** (15), 5620–5628. doi:10.1002/2014GL061146.

Eade, R., D. Smith, L. Hermanson, and N. Dunstone, 2019: Impacts of regional sea ice loss - a global response. *Zenodo.* doi:10.5281/ZENODO.3565538.

England, M., A. Jahn, and L. Polvani, 2019: Nonuniform Contribution of Internal Variability to Recent Arctic Sea Ice Loss. *Journal of Climate*, **32** (13), 4039–4053. doi:10.1175/JCLI-D-18-0864.1.

——, L. Polvani, and L. Sun, 2018: Contrasting the Antarctic and Arctic Atmospheric Responses to Projected Sea Ice Loss in the Late Twenty-First Century. *Journal of Climate*, **31** (16), 6353–6370. doi:10.1175/JCLI-D-17-0666.1.

Fetterer, F., K. Knowles, W. Meier, M. Savoie, and A. Windnagel, 2017: Sea Ice Index, Version 3.0. *NSIDC: National Snow and Ice Data Center.* doi:https://doi.org/10.7265/N5K072F8.

Fletcher, C. G. and P. J. Kushner, 2011: The Role of Linear Interference in the Annular Mode Response to Tropical SST Forcing. *Journal of Climate*, **24** (3), 778–794. doi:10.1175/2010JCLI3735.1.

Francis, J. A., 2017: Why Are Arctic Linkages to Extreme Weather Still up in the Air? *Bulletin of the American Meteorological Society*, **98** (12), 2551–2557. doi:10.1175/BAMS-D-17-0006.1.

—— and E. Hunter, 2007: Changes in the fabric of the Arctic's greenhouse blanket. *Environmental Research Letters.* doi:10.1088/1748-9326/2/4/045011.

Francis, J. A. and S. J. Vavrus, 2015: Evidence for a wavier jet stream in response to rapid Arctic warming. *Environmental Research Letters*, **10** (1), 014005 pp. doi:10.1088/1748-9326/10/1/014005.

Francis, J. A. and S. J. Vavrus, 2012: Evidence linking Arctic amplification to extreme weather in mid-latitudes. *Geophysical Research Letters*, **39** (6), n/a–n/a. doi:10.1029/2012GL051000.

——, ——, and J. Cohen, 2017: Amplified Arctic warming and mid-latitude weather: new perspectives on emerging connections. *Wiley Interdisciplinary Reviews: Climate Change*, **8** (5), e474 pp. doi:10.1002/wcc.474.

Gelaro, R., and Coauthors, 2017: The modern-era retrospective analysis for research and applications, version 2 (MERRA-2). *Journal of Climate*, **30** (14), 5419–5454. doi:10.1175/JCLI-D-16-0758.1.

Gerdes, R., 2006: Atmospheric response to changes in Arctic sea ice thickness. *Geophysical Research Letters*, **33** (18), L18709 pp. doi:10.1029/2006GL027146.

Ghatak, D. and J. Miller, 2013: Implications for Arctic amplification of changes in the strength of the water vapor feedback. *Journal of Geophysical Research: Atmospheres*, **118** (14), 7569–7578. doi:10.1002/jgrd.50578.

GISTEMP Team, 2020: GISS Surface Temperature Analysis (GISTEMP). [Available online at www.data.giss.nasa.gov/gistemp/.]

Golaz, J. C., and Coauthors, 2019: The DOE E3SM Coupled Model Version 1: Overview and Evaluation at Standard Resolution. *Journal of Advances in Modeling Earth Systems*, **11** (7), 2089–2129. doi:10.1029/2018MS001603.

Goosse, H., and Coauthors, 2018: Quantifying climate feedbacks in polar regions.

Graham, R. M., and Coauthors, 2017: A comparison of the two Arctic atmospheric winter states observed during N-ICE2015 and SHEBA. *Journal of Geophysical Research: Atmospheres*, **122** (11), 5716–5737. doi:10.1002/2016JD025475.

Graversen, R. G. and M. Wang, 2009: Polar amplification in a coupled climate model with locked albedo. *Climate Dynamics*, **33** (5), 629–643. doi:10.1007/s00382-009-0535-6.

Graversen, R. G., T. Mauritsen, M. Tjernström, E. Källén, and G. Svensson, 2008: Vertical structure of recent Arctic warming. *Nature*, **451** (7174), 53–56. doi:10.1038/nature06502.

Hall, A., P. Cox, C. Huntingford, and S. Klein, 2019: Progressing emergent constraints on future climate change.

Hansen, F., K. Matthes, and L. J. Gray, 2013: Sensitivity of stratospheric dynamics and chemistry to QBO nudging width in the chemistry-climate model WACCM. *Journal of Geophysical Research: Atmospheres*, **118** (18), 10,464–10,474. doi:10.1002/jgrd.50812.

Harvey, B. J., L. C. Shaffrey, and T. J. Woollings, 2014: Equator-to-pole temperature differences and the extra-tropical storm track responses of the CMIP5 climate models. *Climate Dynamics*. doi:10.1007/s00382-013-1883-9.

Hawkins, E. and R. Sutton, 2012: Time of emergence of climate signals. *Geophysical Research Letters*. doi:10.1029/2011GL050087.

——, D. Frame, L. Harrington, M. Joshi, A. King, M. Rojas, and R. Sutton, 2020: Observed Emergence of the Climate Change Signal: From the Familiar to the Unknown. *Geophysical Research Letters*, **47** (6). doi:10.1029/2019GL086259.

Henderson, G. R., Y. Peings, J. C. Furtado, and P. J. Kushner, 2018: Snow–atmosphere coupling in the Northern Hemisphere. *Nature Climate Change*, 1 pp. doi:10.1038/s41558-018-0295-6.

Hersbach, H., and Coauthors, 2020: The ERA5 Global Reanalysis. *Quarterly Journal of the Royal Meteorological Society*. doi:10.1002/qj.3803.

—— and L. Dick, 2016: ERA5 reanalysis is in production. *ECMWF Newsletter*, **147** (147), 7 pp.

Higgins, M. E. and J. J. Cassano, 2009: Impacts of reduced sea ice on winter Arctic atmospheric circulation, precipitation, and temperature. *Journal of Geophysical Research*, **114** (D16), D16107 pp. doi:10.1029/2009JD011884.

Holland, M. M. and C. M. Bitz, 2003: Polar amplification of climate change in coupled models. *Climate Dynamics.* doi:10.1007/s00382-003-0332-6.

Holland, M. M. and J. Stroeve, 2011: Changing seasonal sea ice predictor relationships in a changing Arctic climate. *Geophysical Research Letters*, **38** (18), n/a–n/a. doi:10.1029/2011GL049303.

——, C. M. Bitz, and B. Tremblay, 2006: Future abrupt reductions in the summer Arctic sea ice. *Geophysical Research Letters*, **33** (23). doi:10.1029/2006GL028024.

Holton, J. R. and H.-C. Tan, 1980: The Influence of the Equatorial Quasi-Biennial Oscillation on the Global Circulation at 50 mb. *http://dx.doi.org/10.1175/1520-0469(1980)037<2200:TIOTEQ>2.0.CO;2.* doi:10.1175/1520-0469(1980)037⟨2200:TIOTEQ⟩2.0.CO;2.

Honda, M., J. Inoue, and S. Yamane, 2009: Influence of low Arctic sea-ice minima on anomalously cold Eurasian winters. *Geophysical Research Letters*, **36** (8), L08707 pp. doi:10.1029/2008GL037079.

Hu, Y. and K. K. Tung, 2002: Tropospheric and equatorial influences on planetary-wave amplitude in the stratosphere. *Geophysical Research Letters*, **29** (2), 1019 pp. doi:10.1029/2001GL013762.

Hunke, E. C. and M. M. Holland, 2007: Global atmospheric forcing data for Arctic ice-ocean modeling. *Journal of Geophysical Research*, **112** (C4), C04S14 pp. doi:10.1029/2006JC003640.

Jahn, A., 2018: Reduced probability of ice-free summers for 1.5C compared to 2C warming. *Nature Climate Change*, **8** (5), 409–413. doi:10.1038/s41558-018-0127-8.

——, J. E. Kay, M. M. Holland, and D. M. Hall, 2016: How predictable is the timing of a summer ice-free Arctic? *Geophysical Research Letters.* doi:10.1002/2016GL070067.

Johannessen, O., and Coauthors, 2004: Arctic climate change: observed and modelled temperature and sea-ice variability. *Tellus A: Dynamic Meteorology and Oceanography*, **56** (5), 559–560. doi:10.3402/tellusa.v56i5.14599.

Kalnay, E., and Coauthors, 1996: The NCEP/NCAR 40-Year Reanalysis Project. *Bulletin of the American Meteorological Society*, **77** (3), 437–471. doi:10.1175/1520-0477(1996)077⟨0437:TNYRP⟩2.0.CO;2.

Kay, J. E., and Coauthors, 2015: The Community Earth System Model (CESM) Large Ensemble Project: A Community Resource for Studying Climate Change in the Presence of Internal Climate Variability. *Bulletin of the American Meteorological Society*, **96** (8), 1333–1349. doi:10.1175/BAMS-D-13-00255.1.

Kay, J. E., M. M. Holland, and A. Jahn, 2011a: Inter-annual to multi-decadal Arctic sea ice extent trends in a warming world. *Geophysical Research Letters*, **38** (15). doi:10.1029/2011GL048008.

——, ——, and ——, 2011b: Inter-annual to multi-decadal Arctic sea ice extent trends in a warming world. *Geophysical Research Letters*, **38** (15), n/a–n/a. doi:10.1029/2011GL048008.

——, T. L'Ecuyer, H. Chepfer, N. Loeb, A. Morrison, and G. Cesana, 2016: Recent Advances in Arctic Cloud and Climate Research.

Kidston, J., A. A. Scaife, S. C. Hardiman, D. M. Mitchell, N. Butchart, M. P. Baldwin, and L. J. Gray, 2015: Stratospheric influence on tropospheric jet streams, storm tracks and surface weather. *Nature Geoscience*, **8** (6), 433–440. doi:10.1038/ngeo2424.

Kim, B. M., and Coauthors, 2017: Major cause of unprecedented Arctic warming in January 2016: Critical role of an Atlantic windstorm. *Scientific Reports*, **7.** doi:10.1038/srep40051.

Kim, B.-M., S.-W. Son, S.-K. Min, J.-H. Jeong, S.-J. Kim, X. Zhang, T. Shim, and J.-H. Yoon, 2014: Weakening of the stratospheric polar vortex by Arctic sea-ice loss. *Nature Communications*, **5**, 4646 pp. doi:10.1038/ncomms5646.

Kinnard, C., C. M. Zdanowicz, D. A. Fisher, E. Isaksson, A. De Vernal, and L. G. Thompson, 2011: Reconstructed changes in Arctic sea ice over the past 1,450 years. *Nature.* doi:10.1038/nature10581.

Knutson, T. R., F. Zeng, and A. T. Wittenberg, 2013: Multimodel Assessment of Regional Surface Temperature Trends: CMIP3 and CMIP5 Twentieth-Century Simulations. *Journal of Climate*, **26** (22), 8709–8743. doi:10.1175/JCLI-D-12-00567.1.

Koenigk, T., and Coauthors, 2019: Impact of Arctic sea ice variations on winter temperature anomalies in northern hemispheric land areas. *Climate Dynamics*, **52** (5-6), 3111–3137. doi:10.1007/s00382-018-4305-1.

Kretschmer, M., D. Coumou, L. Agel, M. Barlow, E. Tziperman, and J. Cohen, 2017: More-Persistent Weak Stratospheric Polar Vortex States Linked to Cold Extremes. *Bulletin of the American Meteorological Society*, BAMS–D–16–0259.1. doi:10.1175/BAMS-D-16-0259.1.

Krinner, G., A. Rinke, K. Dethloff, and I. V. Gorodetskaya, 2009: Impact of prescribed Arctic sea ice thickness in simulations of the present and future climate. *Climate Dynamics*, **35** (4), 619–633. doi:10.1007/s00382-009-0587-7.

Kumar, A., and Coauthors, 2010: Contribution of sea ice loss to Arctic amplification. *Geophysical Research Letters*, **37** (21), n/a–n/a. doi:10.1029/2010GL045022.

Kwok, R., 2018: Arctic sea ice thickness, volume, and multiyear ice coverage: losses and coupled variability (1958–2018). *Environmental Research Letters*, **13** (10), 105005 pp. doi:10.1088/1748-9326/aae3ec.

Kwok, R. and D. A. Rothrock, 2009: Decline in Arctic sea ice thickness from submarine and ICESat records: 1958-2008. *Geophysical Research Letters*, **36** (15), n/a–n/a. doi:10.1029/2009GL039035.

—— and G. F. Cunningham, 2010: Contribution of melt in the Beaufort Sea to the decline in Arctic multiyear sea ice coverage: 1993-2009. *Geophysical Research Letters.* doi:10.1029/2010GL044678.

—— and ——, 2008: ICESat over Arctic sea ice: Estimation of snow depth and ice thickness. *Journal of Geophysical Research*, **113** (C8), C08010 pp. doi:10.1029/2008JC004753.

Labe, Z., G. Magnusdottir, and H. Stern, 2018a: Variability of Arctic Sea Ice Thickness Using PIOMAS and the CESM Large Ensemble. *Journal of Climate*, **31** (8), 3233–3247. doi:10.1175/JCLI-D-17-0436.1.

——, Y. Peings, and G. Magnusdottir, 2018b: Contributions of ice thickness to the atmospheric response from projected Arctic sea ice loss. *Geophysical Research Letters*, **45** (11), 5635–5642. doi:10.1029/2018GL078158.

——, ——, and ——, 2019: The effect of QBO phase on the atmospheric response to projected Arctic sea ice loss in early winter. *Geophysical Research Letters*, **46** (13), 7663–7671. doi:10.1029/2019GL083095.

Lang, A., S. Yang, and E. Kaas, 2017: Sea ice thickness and recent Arctic warming. *Geophysical Research Letters.* doi:10.1002/2016GL071274.

Laxon, S. W., and Coauthors, 2013: CryoSat-2 estimates of Arctic sea ice thickness and volume. *Geophysical Research Letters*, **40** (4), 732–737. doi:10.1002/grl.50193.

Lee, S., T. Gong, S. B. Feldstein, J. A. Screen, and I. Simmonds, 2017: Revisiting the Cause of the 1989–2009 Arctic Surface Warming Using the Surface Energy Budget: Downward Infrared Radiation Dominates the Surface Fluxes. *Geophysical Research Letters*, **44** (20), 10,654–10,661. doi:10.1002/2017GL075375.

Lehner, F., C. Deser, N. Maher, J. Marotzke, E. Fischer, L. Brunner, R. Knutti, and E. Hawkins, 2020: Partitioning climate projection uncertainty with multiple Large Ensembles and CMIP5/6. *Earth System Dynamics Discussions*, 1–28. doi:10.5194/esd-2019-93.

Lenssen, N. J. L., G. A. Schmidt, J. E. Hansen, M. J. Menne, A. Persin, R. Ruedy, and D. Zyss, 2019: Improvements in the GISTEMP Uncertainty Model. *Journal of Geophysical Research: Atmospheres*, **124** (12), 6307–6326. doi:10.1029/2018JD029522.

Li, D., R. Zhang, T. R. Knutson, J. Zhang, and L. H. Smedsrud, 2017: On the discrepancy between observed and CMIP5 multi-model simulated Barents Sea winter sea ice decline. *Nature Communications*, **8**, 14991 pp. doi:10.1038/ncomms14991.

Liang, Y., and Coauthors, 2020: Quantification of the Arctic Sea Ice-Driven Atmospheric Circulation Variability in Coordinated Large Ensemble Simulations. *Geophysical Research Letters*, **47** (1). doi:10.1029/2019GL085397.

Lindsay, R., 2010: New Unified Sea Ice Thickness Climate Data Record. *Eos, Transactions American Geophysical Union*, **91** (44), 405 pp. doi:10.1029/2010EO440001.

Lindsay, R. and A. Schweiger, 2015: Arctic sea ice thickness loss determined using subsurface, aircraft, and satellite observations. *The Cryosphere*, **9** (1), 269–283. doi:10.5194/tc-9-269-2015.

——, M. Wensnahan, A. Schweiger, and J. Zhang, 2014: Evaluation of Seven Different Atmospheric Reanalysis Products in the Arctic*. *Journal of Climate*, **27** (7), 2588–2606. doi:10.1175/JCLI-D-13-00014.1.

Lindsay, R. W. and J. Zhang, 2006: Arctic Ocean Ice Thickness: Modes of Variability and the Best Locations from Which to Monitor Them*. *Journal of Physical Oceanography*, **36** (3), 496–506. doi:10.1175/JPO2861.1.

Liu, J., M. Song, R. M. Horton, and Y. Hu, 2013: Reducing spread in climate model projections of a September ice-free Arctic. *Proceedings of the National Academy of Sciences of the United States of America*, **110** (31), 12571–6. doi:10.1073/pnas.1219716110.

Magnusdottir, G., C. Deser, and R. Saravanan, 2004: The Effects of North Atlantic SST and Sea Ice Anomalies on the Winter Circulation in CCM3. Part I: Main Features and Storm Track Characteristics of the Response. *Journal of Climate*, **17** (5), 857–876. doi:10.1175/1520-0442(2004)017⟨0857:TEONAS⟩2.0.CO;2.

Mahlstein, I. and R. Knutti, 2012: September Arctic sea ice predicted to disappear near 2C global warming above present. *Journal of Geophysical Research Atmospheres.* doi:10.1029/2011JD016709.

——, G. Hegerl, and S. Solomon, 2012: Emerging local warming signals in observational data. *Geophysical Research Letters*, **39** (21), n/a–n/a. doi:10.1029/2012GL053952.

Manabe, S. and R. J. Stouffer, 1980: Sensitivity of a global climate model to an increase of CO2 concentration in the atmosphere. *Journal of Geophysical Research.* doi:10.1029/JC085iC10p05529.

Manda, A., N. Hirose, and T. Yanagi, 2005: Feasible Method for the Assimilation of Satellite-Derived SST with an Ocean Circulation Model. *Journal of Atmospheric and Oceanic Technology*, **22** (6), 746–756. doi:10.1175/JTECH1744.1.

Mann, H. B., 1945: Nonparametric Tests Against Trend. *Econometrica.* doi:10.2307/1907187.

Markus, T., J. C. Stroeve, and J. Miller, 2009: Recent changes in Arctic sea ice melt onset, freezeup, and melt season length. *Journal of Geophysical Research*, **114** (C12), C12024 pp. doi:10.1029/2009JC005436.

Marsh, D. R., M. J. Mills, D. E. Kinnison, J.-F. Lamarque, N. Calvo, and L. M. Polvani, 2013: Climate Change from 1850 to 2005 Simulated in CESM1(WACCM). *Journal of Climate*, **26** (19), 7372–7391. doi:10.1175/JCLI-D-12-00558.1.

Maslanik, J., J. Stroeve, C. Fowler, and W. Emery, 2011: Distribution and trends in Arctic sea ice age through spring 2011. *Geophysical Research Letters*, **38** (13), n/a–n/a. doi:10.1029/2011GL047735.

McCusker, K. E., J. C. Fyfe, and M. Sigmond, 2016: Twenty-five winters of unexpected Eurasian cooling unlikely due to Arctic sea-ice loss. *Nature Geoscience*, **9** (11), 838–842. doi:10.1038/ngeo2820.

McKenna, C. M., T. J. Bracegirdle, E. F. Shuckburgh, P. H. Haynes, and M. M. Joshi, 2017: Arctic sea-ice loss in different regions leads to contrasting Northern Hemisphere impacts. *Geophysical Research Letters.* doi:10.1002/2017GL076433.

Melia, N., K. Haines, and E. Hawkins, 2015: Improved Arctic sea ice thickness projections using bias-corrected CMIP5 simulations. *The Cryosphere*, **9** (6), 2237–2251. doi:10.5194/tc-9-2237-2015.

Messori, G., C. Woods, and R. Caballero, 2018: On the drivers of wintertime temperature extremes in the high arctic. *Journal of Climate*, **31** (4), 1597–1618. doi:10.1175/JCLI-D-17-0386.1.

Moore, G. W., 2016: The December 2015 North Pole Warming Event and the Increasing Occurrence of Such Events. *Scientific Reports*, **6.** doi:10.1038/srep39084.

——, A. Schweiger, J. Zhang, and M. Steele, 2018: What Caused the Remarkable February 2018 North Greenland Polynya? *Geophysical Research Letters*, **45** (24), 13,342–13,350. doi:10.1029/2018GL080902.

Mori, M., M. Watanabe, H. Shiogama, J. Inoue, and M. Kimoto, 2014: Robust Arctic sea-ice influence on the frequent Eurasian cold winters in past decades. *Nature Geoscience*, **7** (12), 869–873. doi:10.1038/ngeo2277.

——, Y. Kosaka, M. Watanabe, H. Nakamura, and M. Kimoto, 2019: A reconciled estimate of the influence of Arctic sea-ice loss on recent Eurasian cooling. *Nature Climate Change*, 1 pp. doi:10.1038/s41558-018-0379-3.

Nakamura, T., K. Yamazaki, K. Iwamoto, M. Honda, Y. Miyoshi, Y. Ogawa, and J. Ukita, 2015: A negative phase shift of the winter AO/NAO due to the recent Arctic sea-ice reduction in late autumn. *Journal of Geophysical Research: Atmospheres*, **120** (8), 3209–3227. doi:10.1002/2014JD022848.

——, ——, ——, ——, ——, ——, Y. Tomikawa, and J. Ukita, 2016a: The stratospheric pathway for Arctic impacts on midlatitude climate. *Geophysical Research Letters*, **43** (7), 3494–3501. doi:10.1002/2016GL068330.

——, ——, M. Honda, J. Ukita, R. Jaiser, D. Handorf, and K. Dethloff, 2016b: On the atmospheric response experiment to a Blue Arctic Ocean. *Geophysical Research Letters*, **43** (19), 10,394–10,402. doi:10.1002/2016GL070526.

Newson, R. L., 1973: Response of a General Circulation Model of the Atmosphere to Removal of the Arctic Ice-cap. *Nature*, **241** (5384), 39–40. doi:10.1038/241039b0.

Notz, D., and Coauthors, 2020: Arctic Sea Ice in CMIP6. *Geophysical Research Letters*, **47** (10). doi:10.1029/2019gl086749.

—— and J. Stroeve, 2016: Observed Arctic sea-ice loss directly follows anthropogenic CO2 emission. *Science*, **354** (6313), 747–750. doi:10.1126/science.aag2345.

Ogawa, F., and Coauthors, 2018: Evaluating impacts of recent Arctic sea-ice loss on the northern hemisphere winter climate change. *Geophysical Research Letters.* doi:10.1002/2017GL076502.

Onarheim, I. H. and M. Årthun, 2017: Toward an ice-free Barents Sea. *Geophysical Research Letters.* doi:10.1002/2017GL074304.

——, T. Eldevik, L. H. Smedsrud, and J. C. Stroeve, 2018: Seasonal and regional manifestation of Arctic sea ice loss. *Journal of Climate*, JCLI–D–17–0427.1. doi:10.1175/JCLI-D-17-0427.1.

O'Reilly, C. H., A. Weisheimer, T. Woollings, L. J. Gray, and D. MacLeod, 2019: The importance of stratospheric initial conditions for winter North Atlantic Oscillation predictability and implications for the signal-to-noise paradox. *Quarterly Journal of the Royal Meteorological Society*, **145** (718), 131–146. doi:10.1002/qj.3413.

Osborne, J. M., J. A. Screen, and M. Collins, 2017: Ocean–Atmosphere State Dependence of the Atmospheric Response to Arctic Sea Ice Loss. *Journal of Climate*, **30** (5), 1537–1552. doi:10.1175/JCLI-D-16-0531.1.

Overland, J. E., and Coauthors, 2016: Nonlinear response of mid-latitude weather to the changing Arctic. *Nature Climate Change*, **6** (11), 992–999. doi:10.1038/nclimate3121.

—— and M. Wang, 2007: Future regional Arctic sea ice declines. *Geophysical Research Letters*, **34** (17), L17705 pp. doi:10.1029/2007GL030808.

—— and ——, 2016: Recent extreme arctic temperatures are due to a split polar vortex. *Journal of Climate*, **29** (15), 5609–5616. doi:10.1175/JCLI-D-16-0320.1.

—— and ——, 2013: When will the summer Arctic be nearly sea ice free? *Geophysical Research Letters*, **40** (10), 2097–2101. doi:10.1002/grl.50316.

——, K. R. Wood, and M. Wang, 2011: Warm Arctic-cold continents: climate impacts of the newly open Arctic Sea. *Polar Research*, **30** (1), 15787 pp. doi:10.3402/polar.v30i0.15787.

Panagiotopoulos, F., M. Shahgedanova, A. Hannachi, and D. B. Stephenson, 2005: Observed Trends and Teleconnections of the Siberian High: A Recently Declining Center of Action. *Journal of Climate*, **18** (9), 1411–1422. doi:10.1175/JCLI3352.1.

Park, K., S. M. Kang, D. Kim, M. F. Stuecker, and F.-F. Jin, 2018: Contrasting Local and Remote Impacts of Surface Heating on Polar Warming and Amplification. *Journal of Climate*, **31** (8), 3155–3166. doi:10.1175/JCLI-D-17-0600.1.

Parkinson, C. L., 2019: A 40-y record reveals gradual Antarctic sea ice increases followed by decreases at rates far exceeding the rates seen in the Arctic. *Proceedings of the National Academy of Sciences of the United States of America*, **116** (29), 14414–14423. doi:10.1073/pnas.1906556116.

—— and N. E. DiGirolamo, 2016: New visualizations highlight new information on the contrasting Arctic and Antarctic sea-ice trends since the late 1970s. *Remote Sensing of Environment*, **183**, 198–204. doi:10.1016/j.rse.2016.05.020.

—— and W. M. Washington, 1979: A large-scale numerical model of sea ice. *Journal of Geophysical Research*, **84** (C1), 311 pp. doi:10.1029/JC084iC01p00311.

——, D. J. Cavalieri, P. Gloersen, H. J. Zwally, and J. C. Comiso, 1999: Arctic sea ice extents, areas, and trends, 1978-1996. *Journal of Geophysical Research: Oceans*, **104** (C9), 20837–20856. doi:10.1029/1999JC900082.

Peings, Y., 2019: Ural Blocking as a Driver of Early-Winter Stratospheric Warmings. *Geophysical Research Letters*, **46** (10), 5460–5468. doi:10.1029/2019GL082097.

Peings, Y. and G. Magnusdottir, 2014: Response of the Wintertime Northern Hemisphere Atmospheric Circulation to Current and Projected Arctic Sea Ice Decline: A Numerical Study with CAM5. *Journal of Climate*, **27** (1), 244–264. doi:10.1175/JCLI-D-13-00272.1.

—— and ——, 2015: Role of sea surface temperature, Arctic sea ice and Siberian snow in forcing the atmospheric circulation in winter of 2012–2013. *Climate Dynamics*, **45** (5-6), 1181–1206. doi:10.1007/s00382-014-2368-1.

Peings, Y., H. Douville, J. Colin, D. S. Martin, and G. Magnusdottir, 2017: Snow-(N)AO Teleconnection and Its Modulation by the Quasi-Biennial Oscillation. *Journal of Climate*, **30** (24), 10211–10235. doi:10.1175/JCLI-D-17-0041.1.

Peings, Y., J. Cattiaux, and G. Magnusdottir, 2019: The Polar Stratosphere as an Arbiter of the Projected Tropical Versus Polar Tug of War. *Geophysical Research Letters*, 2019GL082463 pp. doi:10.1029/2019GL082463.

——, ——, S. J. Vavrus, and G. Magnusdottir, 2018: Projected squeezing of the wintertime North-Atlantic jet. *Environmental Research Letters*, **13** (7), 074016 pp. doi:10.1088/1748-9326/aacc79.

Perlwitz, J., M. Hoerling, and R. Dole, 2015: Arctic Tropospheric Warming: Causes and Linkages to Lower Latitudes. *Journal of Climate*, **28** (6), 2154–2167. doi:10.1175/JCLI-D-14-00095.1.

Petoukhov, V. and V. A. Semenov, 2010: A link between reduced Barents-Kara sea ice and cold winter extremes over northern continents. *Journal of Geophysical Research*, **115** (D21), D21111 pp. doi:10.1029/2009JD013568.

Petty, A. A., J. C. Stroeve, P. R. Holland, L. N. Boisvert, A. C. Bliss, N. Kimura, and W. N. Meier, 2018: The Arctic sea ice cover of 2016: A year of record-low highs and higher-Than-expected lows. *Cryosphere*, **12** (2), 433–452. doi:10.5194/tc-12-433-2018.

——, N. T. Kurtz, R. Kwok, T. Markus, and T. Neumann, 2020: Winter Arctic sea ice thickness from ICESat-2 freeboards. *Journal of Geophysical Research: Oceans*, e2019JC015764 pp. doi:10.1029/2019JC015764.

Pithan, F. and T. Mauritsen, 2014: Arctic amplification dominated by temperature feedbacks in contemporary climate models. *Nat. Geosci.*, **7**, 181–184. doi:10.1038/NGEO2071.

Plumb, R. A., 1985: On the Three-Dimensional Propagation of Stationary Waves. *Journal of the Atmospheric Sciences*, **42** (3), 217–229. doi:10.1175/1520-0469(1985)042⟨0217:OTTDPO⟩2.0.CO;2.

Porter, D. F., J. J. Cassano, and M. C. Serreze, 2012: Local and large-scale atmospheric responses to reduced Arctic sea ice and ocean warming in the WRF model. *Journal of Geophysical Research Atmospheres*. doi:10.1029/2011JD016969.

Rasch, P. J., and Coauthors, 2019: An Overview of the Atmospheric Component of the Energy Exascale Earth System Model. *Journal of Advances in Modeling Earth Systems*, **11** (8), 2377–2411. doi:10.1029/2019MS001629.

Rayner, N. A., D. E. Parker, E. B. Horton, C. K. Folland, L. V. Alexander, D. P. Rowell, E. C. Kent, and A. Kaplan, 2003: Global analyses of sea surface temperature, sea ice, and night marine air temperature since the late nineteenth century. *Journal of Geophysical Research*, **108** (D14), 4407 pp. doi:10.1029/2002JD002670.

Richter, J. H., C. Chen, Q. Tang, S. Xie, and P. J. Rasch, 2019: Improved Simulation of the QBO in E3SMv1. *Journal of Advances in Modeling Earth Systems*, **11** (11), 3403–3418. doi:10.1029/2019MS001763.

——, F. Sassi, and R. R. Garcia, 2010: Toward a Physically Based Gravity Wave Source Parameterization in a General Circulation Model. *Journal of the Atmospheric Sciences*, **67** (1), 136–156. doi:10.1175/2009JAS3112.1.

——, J. A. Anstey, N. Butchart, Y. Kawatani, G. A. Meehl, S. Osprey, and I. R. Simpson, 2020: Progress in Simulating the Quasi-Biennial Oscillation in CMIP Models. *Journal of Geophysical Research: Atmospheres*, **125** (8). doi:10.1029/2019JD032362.

Rigor, I. G., J. M. Wallace, and R. L. Colony, 2002: Response of Sea Ice to the Arctic Oscillation. *Journal of Climate*, **15** (18), 2648–2663. doi:10.1175/1520-0442(2002)015⟨2648:ROSITT⟩2.0.CO;2.

Rinke, A., W. Maslowski, K. Dethloff, and J. Clement, 2006: Influence of sea ice on the atmosphere: A study with an Arctic atmospheric regional climate model. *Journal of Geophysical Research*, **111** (D16), D16103 pp. doi:10.1029/2005JD006957.

Roach, L. A., and Coauthors, 2020: Antarctic Sea Ice Area in CMIP6. *Geophysical Research Letters*. doi:10.1029/2019GL086729.

Rogelj, J., and Coauthors, 2016: Paris Agreement climate proposals need a boost to keep warming well below 2 °c.

Rosenblum, E. and I. Eisenman, 2017: Sea ice trends in climate models only accurate in runs with biased global warming. *Journal of Climate*, JCLI–D–16–0455.1. doi:10.1175/JCLI-D-16-0455.1.

Rothrock, D. A. and J. Zhang, 2005: Arctic Ocean sea ice volume: What explains its recent depletion? *Journal of Geophysical Research*, **110** (C1), C01002 pp. doi:10.1029/2004JC002282.

——, D. B. Percival, and M. Wensnahan, 2008: The decline in arctic sea-ice thickness: Separating the spatial, annual, and interannual variability in a quarter century of submarine data. *Journal of Geophysical Research*, **113** (C5), C05003 pp. doi:10.1029/2007JC004252.

——, Y. Yu, and G. A. Maykut, 1999: Thinning of the Arctic sea-ice cover. *Geophysical Research Letters*, **26** (23), 3469–3472. doi:10.1029/1999GL010863.

Ruzmaikin, A., J. Feynman, X. Jiang, and Y. L. Yung, 2005: Extratropical signature of the quasi-biennial oscillation. *Journal of Geophysical Research*, **110** (D11), D11111 pp. doi:10.1029/2004JD005382.

Sallila, H., S. L. Farrell, J. McCurry, and E. Rinne, 2019: Assessment of contemporary satellite sea ice thickness products for Arctic sea ice. *The Cryosphere*, **13** (4), 1187–1213. doi:10.5194/tc-13-1187-2019.

Scaife, A. A., and Coauthors, 2014: Predictability of the quasi-biennial oscillation and its northern winter teleconnection on seasonal to decadal timescales. *Geophysical Research Letters*, **41** (5), 1752–1758. doi:10.1002/2013GL059160.

—— and D. Smith, 2018: A signal-to-noise paradox in climate science. *npj Climate and Atmospheric Science*, **1** (1), 28 pp. doi:10.1038/s41612-018-0038-4.

Schenzinger, V., S. Osprey, L. Gray, and N. Butchart, 2017: Defining metrics of the Quasi-Biennial Oscillation in global climate models. *Geoscientific Model Development*, **10** (6), 2157–2168. doi:10.5194/gmd-10-2157-2017.

Schweiger, A. J., K. R. Wood, and J. Zhang, 2019: Arctic Sea Ice Volume Variability over 1901–2010: A Model-Based Reconstruction. *Journal of Climate*, **32** (15), 4731–4752. doi:10.1175/JCLI-D-19-0008.1.

Schweiger, A., R. Lindsay, J. Zhang, M. Steele, H. Stern, and R. Kwok, 2011: Uncertainty in modeled Arctic sea ice volume. *Journal of Geophysical Research*, **116** (C8), C00D06 pp. doi:10.1029/2011JC007084.

Screen, J. A., 2018: Arctic sea ice at 1.5 and 2C.

Screen, J. A., 2017a: Climate science: Far-flung effects of Arctic warming. *Nature Publishing Group*, **10.** doi:10.1038/ngeo2924.

Screen, J. A., 2017b: Simulated Atmospheric Response to Regional and Pan-Arctic Sea Ice Loss. *http://dx.doi.org/10.1175/JCLI-D-16-0197.1.* doi:10.1175/JCLI-D-16-0197.1.

——, and Coauthors, 2018a: Consistency and discrepancy in the atmospheric response to Arctic sea-ice loss across climate models. *Nature Geoscience*, 1 pp. doi:10.1038/s41561-018-0059-y.

—— and I. Simmonds, 2011: Erroneous Arctic Temperature Trends in the ERA-40 Reanalysis: A Closer Look. *Journal of Climate*, **24** (10), 2620–2627. doi:10.1175/2010JCLI4054.1.

—— and ——, 2010a: Increasing fall-winter energy loss from the Arctic Ocean and its role in Arctic temperature amplification. *Geophysical Research Letters*, **37** (16), n/a–n/a. doi:10.1029/2010GL044136.

Screen, J. A. and I. Simmonds, 2010b: The central role of diminishing sea ice in recent Arctic temperature amplification. *Nature*, **464** (7293), 1334–7. doi:10.1038/nature09051.

Screen, J. A. and R. Blackport, 2019a: How Robust is the Atmospheric Response to Projected Arctic Sea Ice Loss Across Climate Models? *Geophysical Research Letters*, **46** (20), 11406–11415. doi:10.1029/2019GL084936.

Screen, J. A. and R. Blackport, 2019b: Is sea-ice-driven Eurasian cooling too weak in models? *Nature Climate Change*, **9** (12), 934–936. doi:10.1038/s41558-019-0635-1.

Screen, J. A., C. Deser, and I. Simmonds, 2012: Local and remote controls on observed Arctic warming. *Geophysical Research Letters*, **39** (10), n/a–n/a. doi:10.1029/2012GL051598.

Screen, J. A., C. Deser, and L. Sun, 2015: Reduced Risk of North American Cold Extremes due to Continued Arctic Sea Ice Loss. *Bulletin of the American Meteorological Society*, **96** (9), 1489–1503. doi:10.1175/BAMS-D-14-00185.1.

——, ——, I. Simmonds, and R. Tomas, 2014: Atmospheric impacts of Arctic sea-ice loss, 1979-2009: Separating forced change from atmospheric internal variability. *Climate Dynamics*, **43** (1-2), 333–344. doi:10.1007/s00382-013-1830-9.

——, I. Simmonds, C. Deser, and R. Tomas, 2013: The Atmospheric Response to Three Decades of Observed Arctic Sea Ice Loss. *Journal of Climate*, **26** (4), 1230–1248. doi:10.1175/JCLI-D-12-00063.1.

Screen, J. A., T. J. Bracegirdle, and I. Simmonds, 2018b: Polar Climate Change as Manifest in Atmospheric Circulation. *Current Climate Change Reports*, **4** (4), 383–395. doi:10.1007/s40641-018-0111-4.

Sedlar, J., and Coauthors, 2011: A transitioning Arctic surface energy budget: the impacts of solar zenith angle, surface albedo and cloud radiative forcing. *Climate Dynamics*, **37** (7-8), 1643–1660. doi:10.1007/s00382-010-0937-5.

Sellevold, R., S. Sobolowski, and C. Li, 2016: Investigating Possible Arctic–Midlatitude Teleconnections in a Linear Framework. *Journal of Climate*, **29** (20), 7329–7343. doi:10.1175/JCLI-D-15-0902.1.

Semmler, T., L. Stulic, T. Jung, N. Tilinina, C. Campos, S. Gulev, and D. Koracin, 2016a: Seasonal Atmospheric Responses to Reduced Arctic Sea Ice in an Ensemble of Coupled Model Simulations. *Journal of Climate*, **29** (16), 5893–5913. doi:10.1175/JCLI-D-15-0586.1.

——, T. Jung, and S. Serrar, 2016b: Fast atmospheric response to a sudden thinning of Arctic sea ice. *Climate Dynamics*, **46** (3-4), 1015–1025. doi:10.1007/s00382-015-2629-7.

Serreze, M. C., A. P. Barrett, A. G. Slater, M. Steele, J. Zhang, and K. E. Trenberth, 2007: The large-scale energy budget of the Arctic. *Journal of Geophysical Research*, **112** (D11), D11122 pp. doi:10.1029/2006JD008230.

Serreze, M. C., A. P. Barrett, J. C. Stroeve, D. N. Kindig, and M. M. Holland, 2009: The emergence of surface-based Arctic amplification. *The Cryosphere*, **3** (1), 11–19. doi:10.5194/tc-3-11-2009.

Serreze, M. C. and J. A. Francis, 2006: The Arctic Amplification Debate. *Climatic Change*, **76** (3-4), 241–264. doi:10.1007/s10584-005-9017-y.

—— and J. Stroeve, 2015: Arctic sea ice trends, variability and implications for seasonal ice forecasting. *Philosophical Transactions of the Royal Society of London A: Mathematical, Physical and Engineering Sciences*, **373** (2045).

—— and R. G. Barry, 2011: Processes and impacts of Arctic amplification: A research synthesis. *Global and Planetary Change*, **77** (1-2), 85–96. doi:10.1016/j.gloplacha.2011.03.004.

—— and W. N. Meier, 2019: The Arctic's sea ice cover: trends, variability, predictability, and comparisons to the Antarctic.

——, J. Stroeve, A. P. Barrett, and L. N. Boisvert, 2016: Summer atmospheric circulation anomalies over the Arctic Ocean and their influences on September sea ice extent: A cautionary tale. *Journal of Geophysical Research: Atmospheres.* doi:10.1002/2016JD025161.

Shaw, T. A., and Coauthors, 2016: Storm track processes and the opposing influences of climate change.

Shepherd, T. G., 2014: Atmospheric circulation as a source of uncertainty in climate change projections.

Sigmond, M., J. C. Fyfe, and N. C. Swart, 2018: Ice-free Arctic projections under the Paris Agreement. *Nature Climate Change.* doi:10.1038/s41558-018-0124-y.

Smith, A. and A. Jahn, 2019: Definition differences and internal variability affect the simulated Arctic sea ice melt season. *Cryosphere.* doi:10.5194/tc-13-1-2019.

Smith, D. M., and Coauthors, 2019: The Polar Amplification Model Intercomparison Project (PAMIP) contribution to CMIP6: investigating the causes and consequences of polar amplification. *Geoscientific Model Development*, **12** (3), 1139–1164. doi:10.5194/gmd-12-1139-2019.

——, N. J. Dunstone, A. A. Scaife, E. K. Fiedler, D. Copsey, and S. C. Hardiman, 2017: Atmospheric Response to Arctic and Antarctic Sea Ice: The Importance of Ocean–Atmosphere Coupling and the Background State. *Journal of Climate*, **30** (12), 4547–4565. doi:10.1175/JCLI-D-16-0564.1.

Smith, K. L., P. J. Kushner, and J. Cohen, 2011: The role of linear interference in northern annular mode variability associated with Eurasian snow cover extent. *Journal of Climate.* doi:10.1175/JCLI-D-11-00055.1.

Smith, K. L., R. R. Neely, D. R. Marsh, and L. M. Polvani, 2014: The Specified Chemistry Whole Atmosphere Community Climate Model (SC-WACCM). *Journal of Advances in Modeling Earth Systems*, **6** (3), 883–901. doi:10.1002/2014MS000346.

Smith, R. D., J. K. Dukowicz, and R. C. Malone, 1992: Parallel ocean general circulation modeling. *Physica D*, **60**, 38–61.

Stockdale, T. N., F. Molteni, and L. Ferranti, 2015: Atmospheric initial conditions and the predictability of the Arctic Oscillation. *Geophysical Research Letters*, **42** (4), 1173–1179. doi:10.1002/2014GL062681.

Stroeve, J., A. Barrett, M. Serreze, and A. Schweiger, 2014a: Using records from submarine, aircraft and satellites to evaluate climate model simulations of Arctic sea ice thickness. *The Cryosphere*, **8** (5), 1839–1854. doi:10.5194/tc-8-1839-2014.

Stroeve, J. and D. Notz, 2018: Changing state of Arctic sea ice across all seasons. *Environmental Research Letters*, **13** (10), 103001 pp. doi:10.1088/1748-9326/aade56.

Stroeve, J. C., M. C. Serreze, M. M. Holland, J. E. Kay, J. Malanik, and A. P. Barrett, 2011: The Arctic's rapidly shrinking sea ice cover: a research synthesis. *Climatic Change*, **110** (3-4), 1005–1027. doi:10.1007/s10584-011-0101-1.

Stroeve, J. C., T. Markus, L. Boisvert, J. Miller, and A. Barrett, 2014b: Changes in Arctic melt season and implications for sea ice loss. *Geophysical Research Letters*, **41** (4), 1216–1225. doi:10.1002/2013GL058951.

Stroeve, J. C., V. Kattsov, A. Barrett, M. Serreze, T. Pavlova, M. Holland, and W. N. Meier, 2012: Trends in Arctic sea ice extent from CMIP5, CMIP3 and observations. *Geophysical Research Letters*, **39** (16), n/a–n/a. doi:10.1029/2012GL052676.

Stroeve, J., M. M. Holland, W. Meier, T. Scambos, and M. Serreze, 2007: Arctic sea ice decline: Faster than forecast. *Geophysical Research Letters*, **34** (9). doi:10.1029/2007GL029703@10.1002/(ISSN)1944-8007.GRL40.

Stuecker, M. F., and Coauthors, 2018: Polar amplification dominated by local forcing and feedbacks. *Nature Climate Change*, **8** (12), 1076–1081. doi:10.1038/s41558-018-0339-y.

Sun, L., C. Deser, and R. A. Tomas, 2015: Mechanisms of Stratospheric and Tropospheric Circulation Response to Projected Arctic Sea Ice Loss*. *Journal of Climate.*

——, D. Allured, M. Hoerling, L. Smith, J. Perlwitz, D. Murray, and J. Eischeid, 2017: Drivers of 2016 record Arctic warmth assessed using climate simulations subjected to Factual and Counterfactual forcing. *Weather and Climate Extremes.* doi:10.1016/J.WACE.2017.11.001.

——, J. Perlwitz, and M. Hoerling, 2016: What Caused the Recent "Warm Arctic, Cold Continents" Trend Pattern in Winter Temperatures? *Geophysical Research Letters.* doi:10.1002/2016GL069024.

Swart, N., 2017: Climate variability: Natural causes of Arctic sea-ice loss. *Nature Publishing Group*, **7.** doi:10.1038/nclimate3254.

Swart, N. C., J. C. Fyfe, E. Hawkins, J. E. Kay, and A. Jahn, 2015: Influence of internal variability on Arctic sea-ice trends. *Nature Climate Change*, **5** (2), 86–89. doi:10.1038/nclimate2483.

Taylor, K. E., D. L. Williamson, and F. W. Zwiers, 2000: The Sea Surface Temperature and Sea-Ice Concentration Boundary Conditions for AMIP II Simulations. *PCMDI Report Series*, (60), 28 pp.

Thoman, R. L., and Coauthors, 2020: The Record Low Bering Sea Ice Extent in 2018: Context, Impacts, and an Assessment of the Role of Anthropogenic Climate Change. *Bulletin of the American Meteorological Society*, **101** (1), S53–S58. doi:10.1175/BAMS-D-19-0175.1.

Thompson, D. W. J. and J. M. Wallace, 1998: The Arctic oscillation signature in the wintertime geopotential height and temperature fields. *Geophysical Research Letters*, **25** (9), 1297–1300. doi:10.1029/98GL00950.

——, E. A. Barnes, C. Deser, W. E. Foust, and A. S. Phillips, 2015: Quantifying the Role of Internal Climate Variability in Future Climate Trends. *Journal of Climate*, **28** (16), 6443–6456. doi:10.1175/JCLI-D-14-00830.1.

——, M. P. Baldwin, and J. M. Wallace, 2002: Stratospheric Connection to Northern Hemisphere Wintertime Weather: Implications for Prediction. *Journal of Climate*, **15** (12), 1421–1428. doi:10.1175/1520-0442(2002)015⟨1421:SCTNHW⟩2.0.CO;2.

Thyng, K., C. Greene, R. Hetland, H. Zimmerle, and S. DiMarco, 2016: True Colors of Oceanography: Guidelines for Effective and Accurate Colormap Selection. *Oceanography*, **29** (3), 9–13. doi:10.5670/oceanog.2016.66.

Tilling, R. L., A. Ridout, A. Shepherd, and D. J. Wingham, 2015: Increased Arctic sea ice volume after anomalously low melting in 2013. *Nature Geoscience*, **8** (8), 643–646. doi:10.1038/ngeo2489.

Timmermans, M. L., J. Toole, and R. Krishfield, 2018: Warming of the interior Arctic Ocean linked to sea ice losses at the basin margins. *Science Advances*, **4** (8), eaat6773 pp. doi:10.1126/sciadv.aat6773.

Tokinaga, H., S. P. Xie, and H. Mukougawa, 2017: Early 20th-century Arctic warming intensified by Pacific and Atlantic multidecadal variability. *Proceedings of the National Academy of Sciences of the United States of America*, **114** (24), 6227–6232. doi:10.1073/pnas.1615880114.

Tomas, R. A., C. Deser, and L. Sun, 2016: The Role of Ocean Heat Transport in the Global Climate Response to Projected Arctic Sea Ice Loss. *Journal of Climate*, **29** (19), 6841–6859. doi:10.1175/JCLI-D-15-0651.1.

Turner, J., T. J. Bracegirdle, T. Phillips, G. J. Marshall, and J. S. Hosking, 2013: An Initial Assessment of Antarctic Sea Ice Extent in the CMIP5 Models. *Journal of Climate*, **26** (5), 1473–1484. doi:10.1175/JCLI-D-12-00068.1.

Tyrrell, N. L., A. Y. Karpechko, and P. Räisänen, 2018: The Influence of Eurasian Snow Extent on the Northern Extratropical Stratosphere in a QBO Resolving Model. *Journal of Geophysical Research: Atmospheres*, **123** (1), 315–328. doi:10.1002/2017JD027378.

Vavrus, S. J., 2018: The Influence of Arctic Amplification on Mid-latitude Weather and Climate.

Vihma, T., 2014: Effects of Arctic Sea Ice Decline on Weather and Climate: A Review. *Surveys in Geophysics*, **35** (5), 1175–1214. doi:10.1007/s10712-014-9284-0.

Walsh, J. E., F. Fetterer, J. Scott Stewart, and W. L. Chapman, 2016: A database for depicting Arctic sea ice variations back to 1850. *Geographical Review*. doi:10.1111/j.1931-0846.2016.12195.x.

Wang, M. and J. E. Overland, 2012: A sea ice free summer Arctic within 30 years: An update from CMIP5 models. *Geophysical Research Letters*, **39** (18), n/a–n/a. doi:10.1029/2012GL052868.

Wang, X., J. Key, R. Kwok, and J. Zhang, 2016: Comparison of Arctic Sea Ice Thickness from Satellites, Aircraft, and PIOMAS Data. *Remote Sensing*, **8** (9), 713 pp. doi:10.3390/rs8090713.

Warner, J. L., J. A. Screen, and A. A. Scaife, 2020: Links Between Barents-Kara Sea Ice and the Extratropical Atmospheric Circulation Explained by Internal Variability and Tropical Forcing. *Geophysical Research Letters*, **47** (1). doi:10.1029/2019GL085679.

Warren, S. G., I. G. Rigor, N. Untersteiner, V. F. Radionov, N. N. Bryazgin, Y. I. Aleksandrov, and R. Colony, 1999: Snow Depth on Arctic Sea Ice. *Journal of Climate*, **12** (6), 1814–1829. doi:10.1175/1520-0442(1999)012⟨1814:SDOASI⟩2.0.CO;2.

Warshaw, M. and R. R. Rapp, 1972: An Experiment on the Sensitivity of A Global Circulation Model: Studies in Climate Dynamics for Environmental Security. *J Appl Meteorol.*

Watson, P. A. G. and L. J. Gray, 2014: How Does the Quasi-Biennial Oscillation Affect the Stratospheric Polar Vortex? *Journal of the Atmospheric Sciences*, **71** (1), 391–409. doi:10.1175/JAS-D-13-096.1.

Wilks, D. S., 2016: "The Stippling Shows Statistically Significant Grid Points": How Research Results are Routinely Overstated and Overinterpreted, and What to Do about It. *Bulletin of the American Meteorological Society*, **97** (12), 2263–2273. doi:10.1175/BAMS-D-15-00267.1.

Winton, M., 2006: Amplified Arctic climate change: What does surface albedo feedback have to do with it? *Geophysical Research Letters*, **33** (3), L03701 pp. doi:10.1029/2005GL025244.

Woods, C. and R. Caballero, 2016: The role of moist intrusions in winter arctic warming and sea ice decline. *Journal of Climate*, **29** (12), 4473–4485. doi:10.1175/JCLI-D-15-0773.1.

——, ——, G. Svensson, C. Woods, R. Caballero, and G. Svensson, 2017: Representation of Arctic moist intrusions in CMIP5 models and implications for winter climate biases. *Journal of Climate*, JCLI–D–16–0710.1. doi:10.1175/JCLI-D-16-0710.1.

Xie, J., F. Counillon, L. Bertino, X. Tian-Kunze, and L. Kaleschke, 2016: Benefits of assimilating thin sea ice thickness from SMOS into the TOPAZ system. *The Cryosphere*, **10** (6), 2745–2761. doi:10.5194/tc-10-2745-2016.

Xu, X., S. He, Y. Gao, T. Furevik, H. Wang, F. Li, and F. Ogawa, 2019: Strengthened linkage between midlatitudes and Arctic in boreal winter. *Climate Dynamics*, **53** (7-8), 3971–3983. doi:10.1007/s00382-019-04764-7.

Yang, W. and G. Magnusdottir, 2017: Springtime extreme moisture transport into the Arctic and its impact on sea ice concentration. *Journal of Geophysical Research: Atmospheres*, **122** (10), 5316–5329. doi:10.1002/2016JD026324.

—— and ——, 2018: Year-to-year Variability in Arctic Minimum Sea Ice Extent and its Preconditions in Observations and the CESM Large Ensemble Simulations. *Scientific Reports*, **8** (1), 9070 pp. doi:10.1038/s41598-018-27149-y.

Yu, P., F. Siew, C. Li, S. P. Sobolowski, and M. P. King, 2020: Intermittency of Arctic-midlatitude teleconnections: stratospheric pathway between autumn sea ice and the winter NAO. *Weather and Climate Dynamics.* doi:10.5194/wcd-2019-11.

Zappa, G., F. Pithan, and T. G. Shepherd, 2018: Multi-model evidence for an atmospheric circulation response to Arctic sea ice loss in the CMIP5 future projections. *Geophysical Research Letters.* doi:10.1002/2017GL076096.

Zhang, J. and D. A. Rothrock, 2003: Modeling Global Sea Ice with a Thickness and Enthalpy Distribution Model in Generalized Curvilinear Coordinates. *Monthly Weather Review*, **131** (5), 845–861. doi:10.1175/1520-0493(2003)131⟨0845:MGSIWA⟩2.0.CO;2.

——, D. Rothrock, and M. Steele, 2000: Recent Changes in Arctic Sea Ice: The Interplay between Ice Dynamics and Thermodynamics. *Journal of Climate*, **13** (17), 3099–3114. doi:10.1175/1520-0442(2000)013⟨3099:RCIASI⟩2.0.CO;2.

Zhang, P., Y. Wu, I. R. Simpson, K. L. Smith, X. Zhang, B. De, and P. Callaghan, 2018a: A stratospheric pathway linking a colder Siberia to Barents-Kara Sea sea ice loss. *Science Advances*, **4** (7), eaat6025 pp. doi:10.1126/sciadv.aat6025.

Zhang, Q., C. Xiao, M. Ding, and T. Dou, 2018b: Reconstruction of autumn sea ice extent changes since AD1289 in the Barents-Kara Sea, Arctic. *Science China Earth Sciences.* doi:10.1007/s11430-017-9196-4.

Zhang, R., 2015: Mechanisms for low-frequency variability of summer Arctic sea ice extent. *Proceedings of the National Academy of Sciences of the United States of America*, **112** (15), 4570–5. doi:10.1073/pnas.1422296112.

Zhang, X., A. Sorteberg, J. Zhang, R. Gerdes, and J. C. Comiso, 2008: Recent radical shifts of atmospheric circulations and rapid changes in Arctic climate system. *Geophysical Research Letters*, **35** (22), L22701 pp. doi:10.1029/2008GL035607.

Zwally, H., and Coauthors, 2002: ICESat's laser measurements of polar ice, atmosphere, ocean, and land. *Journal of Geodynamics*, **34** (3-4), 405–445. doi:10.1016/S0264-3707(02)00042-X.

Zygmuntowska, M., P. Rampal, N. Ivanova, and L. H. Smedsrud, 2014: Uncertainties in Arctic sea ice thickness and volume: new estimates and implications for trends. *The Cryosphere*, **8** (2), 705–720. doi:10.5194/tc-8-705-2014.

Appendix A

Appendix

A.1 Chapter 2: Future projections of sea-ice volume

Predicting the timing of the first ice-free summer is of significant interest for scientists and numerous stakeholders. The most common definition of "ice-free" is a threshold of sea-ice extent (SIE) falling below 1.0 million km^2 (e.g., Wang and Overland, 2012; Overland and Wang, 2013; Jahn et al., 2016). Here we define an arbitrary threshold for the timing of the first September sea-ice volume (SIV) dropping below 1000 km^3 to determine the spread in the RCP8.5 LENS simulations (strong emission scenario; 2006-2080). Between all future ensemble members we find a spread larger than one decade, which suggests the timing is subject to large uncertainties from internal variability (Figure A.4). Averaging out all of the ensemble members (and hence the noise), the ensemble mean suggests the SIV threshold is first crossed in the mid-2040s. This timing is fairly consistent with a recent study using LENS by Jahn et al. (2016), which estimated the SIE "ice-free" predictability and found a spread of approximately two decades in a single emission scenario. However, it should also be noted that there is little to no predictability for using SIV with the timing of the first

SIE “ice-free” summer (<1 million km^2) (Jahn et al., 2016).

Table A.1: Description of WACCM4 simulations. All simulations are run for 100 ensemble members branched from a 200-year control (assessed from October to March).

Name	Sea Ice Thickness Forcing	Sea Ice Concentration Forcing
HIC	2-m	Historical: 1976-2005 LENS mean
HIT	Historical: 1976-2005 LENS mean	Historical: 1976-2005 LENS mean
FIT	Future: 2051-2080 LENS mean*	Historical: 1976-2005 LENS mean
FIC	2-m	Future: 2051-2080 LENS mean
FICT	Future: 2051-2080 LENS mean	Future: 2051-2080 LENS mean
FPOL	Future: >66.6°N; 2-m elsewhere	Future: >66.6°N; Historical elsewhere
FSUB	Future: <66.6°N; 2-m elsewhere	Future: <66.6°N; Historical elsewhere

*To preserve historical SIC, future SIT is prescribed to 0.15 m where grid cells are ice-free. Therefore, there is no change in total SIE.

Table A.2: List of climate model experiments used in this study. The overbar indicates a time mean for the forcing level. The ensemble mean December-January-February (DJF) 1000-500 hPa air temperature response ($\Delta\overline{T}_{1000-500}$; °C) can be found in the fourth column for each experiment. The $\Delta\overline{T}_{1000-500}$ anomalies are area/pressure-weighted averages calculated over the polar cap (north of 65°N latitude). The experiments are sorted in ascending order by their $\Delta\overline{T}_{1000-500}$ response.

Experiment	**Forcing**	**Forcing Level**	$\mathbf{\Delta\overline{T}_{1000-500}}$
ΔAMIP	SIC/SST variability	Transient; 1979-2016	+ 0.72
ΔE3SM-SIC-Pd	SIC boundary conditions	AGCM; Present-day	+ 0.76
ΔSIC-Pd	SIC boundary conditions	AGCM; Present-day	+ 0.80
ΔAA-2030	AA nudging	AGCM; $\overline{2020-2039}$	+ 0.86
ΔS-Coupled-Pd	SIC boundary conditions	Coupled; Present-day	+ 0.93
ΔSIT-Pd	SIC/SIT boundary conditions	AGCM; Present-day	+ 0.99
ΔAMIP-HL	SIC/SST variability and AA	Transient; 1979-2016	+ 1.10
ΔE3SM-SIC-Pi	SIC boundary conditions	AGCM; Pre-Industrial	+ 1.22
ΔSIC-Pi	SIC boundary conditions	AGCM; Pre-Industrial	+ 1.40
ΔS-Coupled-Pi	SIC boundary conditions	Coupled; Pre-Industrial	+ 1.59
ΔNET	SIC/SIT boundary conditions	AGCM; $\overline{2051-2080}$	+ 1.86
ΔAA-2060	AA nudging	AGCM; $\overline{2050-2069}$	+ 2.94
ΔAA-2090	AA nudging	AGCM; $\overline{2080-2099}$	+ 4.84

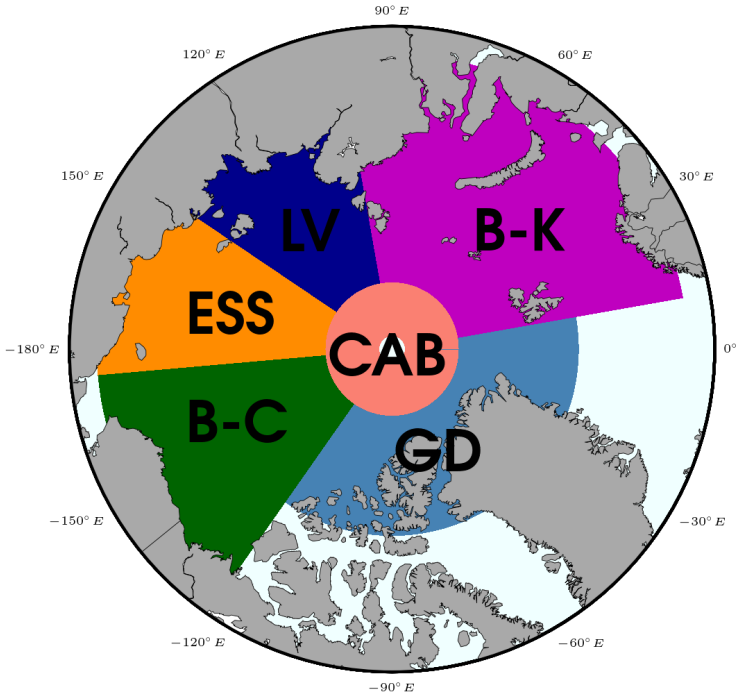

Figure A.1: Masks for regional sea ice analysis are as follows: Central Arctic Basin (CAB), northern Canadian Arctic Archipelago and Greenland coast (GD), Beaufort and Chukchi Seas (B-C), East Siberian Sea (ESS), Laptev Sea (LV), Barents and Kara Seas (B-K)

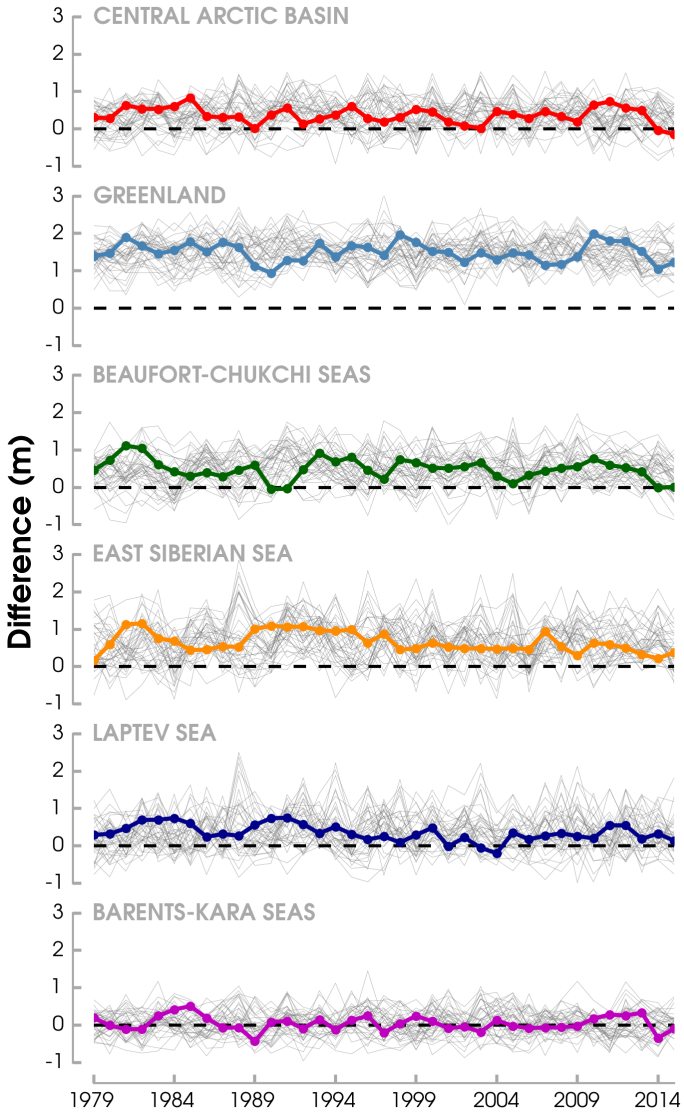

Figure A.2: September sea-ice thickness differences between the LENS mean and PIOMAS over the 1979 to 2015 period. Individual ensembles are shown by each gray line. Regions are an area weighted average for mean grid cell thicknesses of at least 0.15 m.

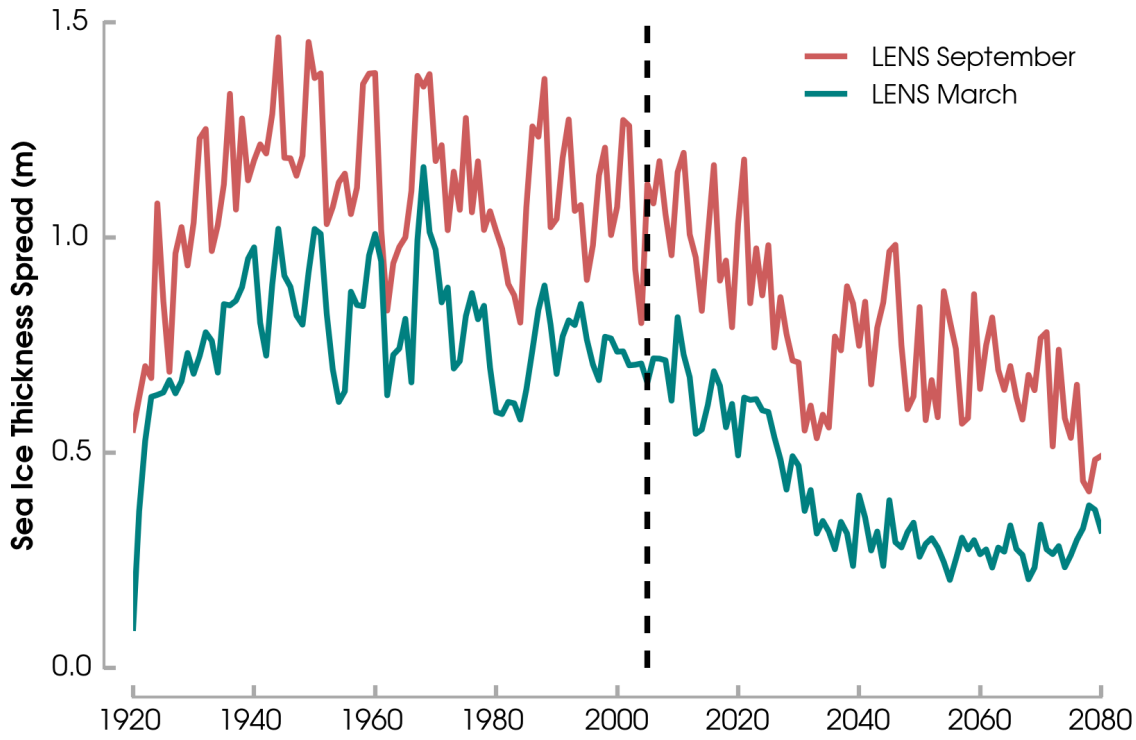

Figure A.3: Difference between the maximum and minimum mean sea-ice thickness from LENS during September (red line) and March (blue line). Sea-ice thickness is an area weighted average north of 65°N. The dashed vertical line separates the historical simulation from the future LENS projection.

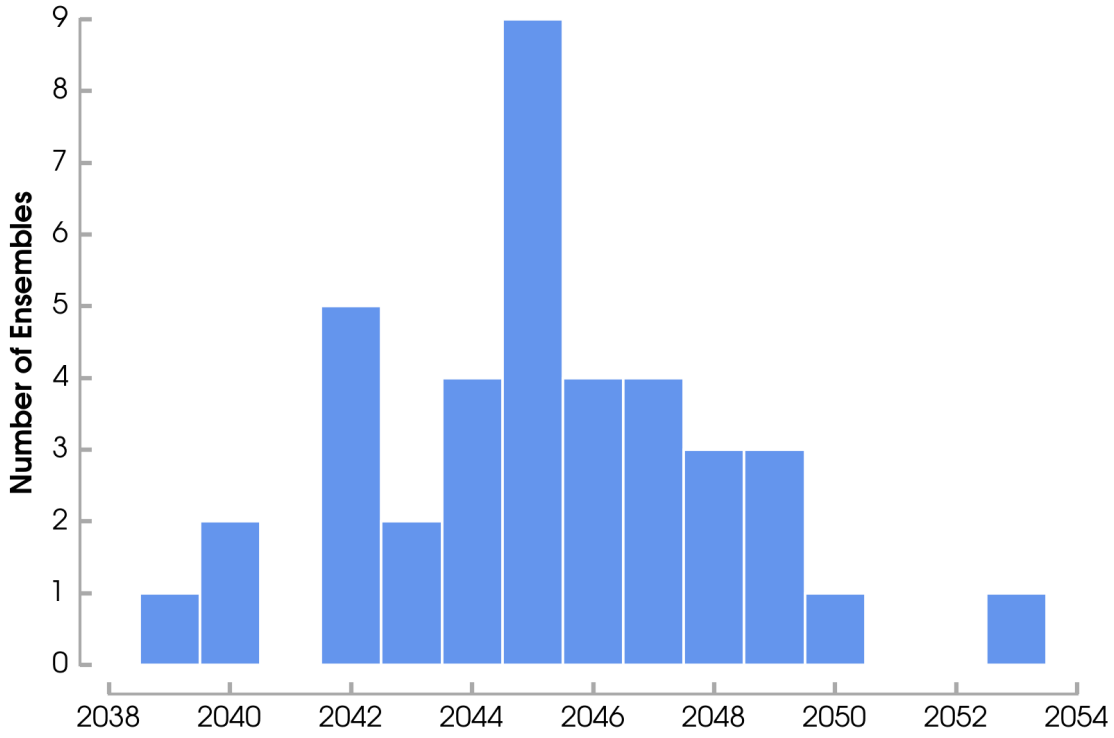

Figure A.4: Frequency (histogram) of the timing for the first September with sea-ice volume less than 1000 km^3 as evaluated per each LENS ensemble member.

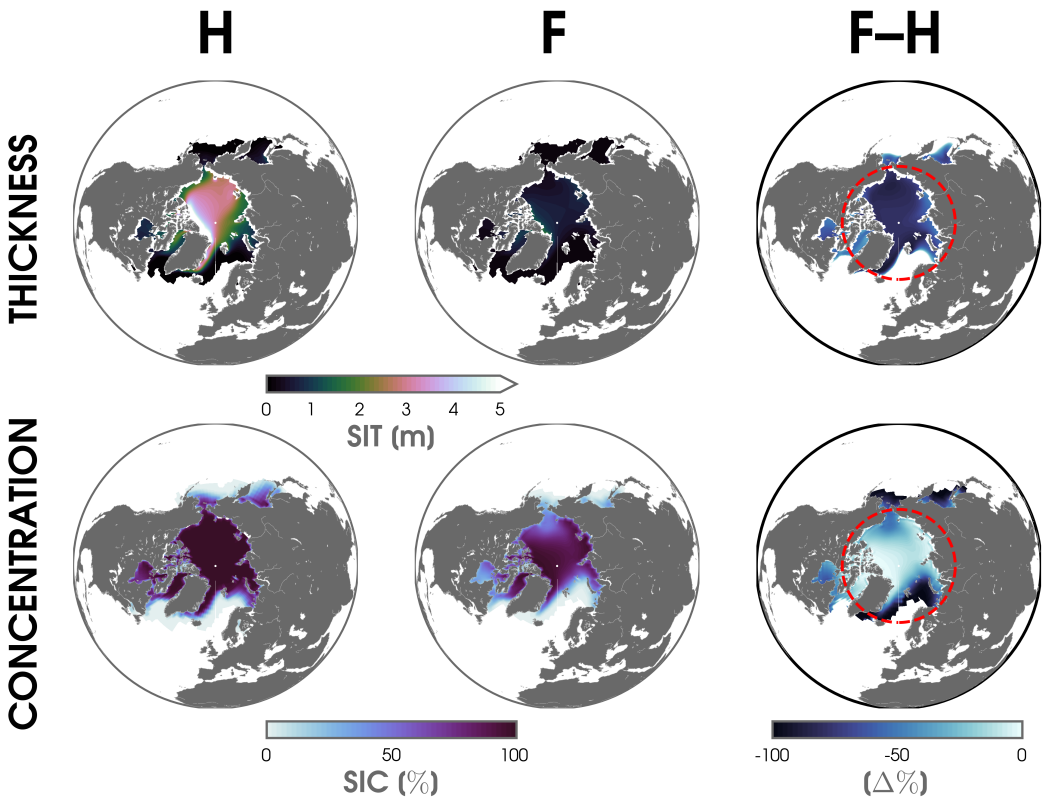

Figure A.5: Winter (DJF) sea ice thickness (SIT) and sea ice concentration (SIC) fields prescribed in the historical (H; left column) and future (F; middle column) experiments. Sea ice fields are taken from the mean of 40 ensemble members in LENS averaged over the 1976-2005 (H) and 2051-2080 (F) periods. The percentage differences (F–H) of SIT and SIC are shown in the right-hand column. The dashed red circle (66.6°N) marks the boundary between the regional sea ice anomaly experiments (FPOL and FSUB).

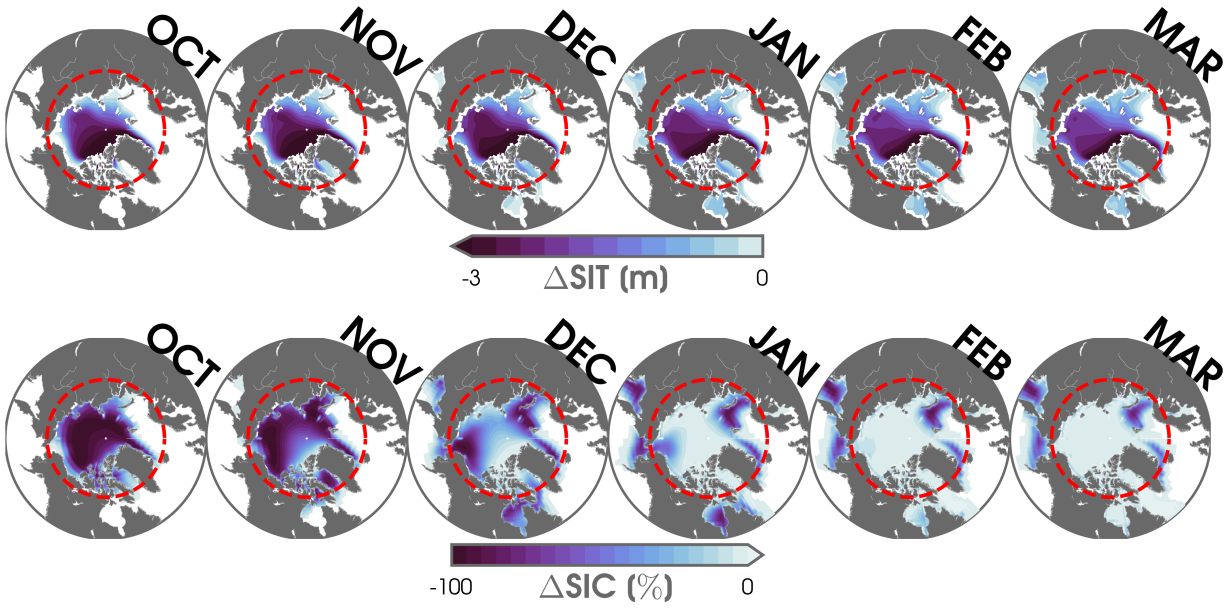

Figure A.6: The difference from future (F; 2051-2080) minus historical (H; 1976-2006) periods of sea ice thickness (SIT) and sea ice concentration (SIC) prescribed in the WACCM4 experiments. Sea ice fields are originally taken from the mean of 40 ensemble members in LENS. The dashed red circle (66.6°N) marks the boundary between the regional sea ice anomaly experiments (FPOL and FSUB).

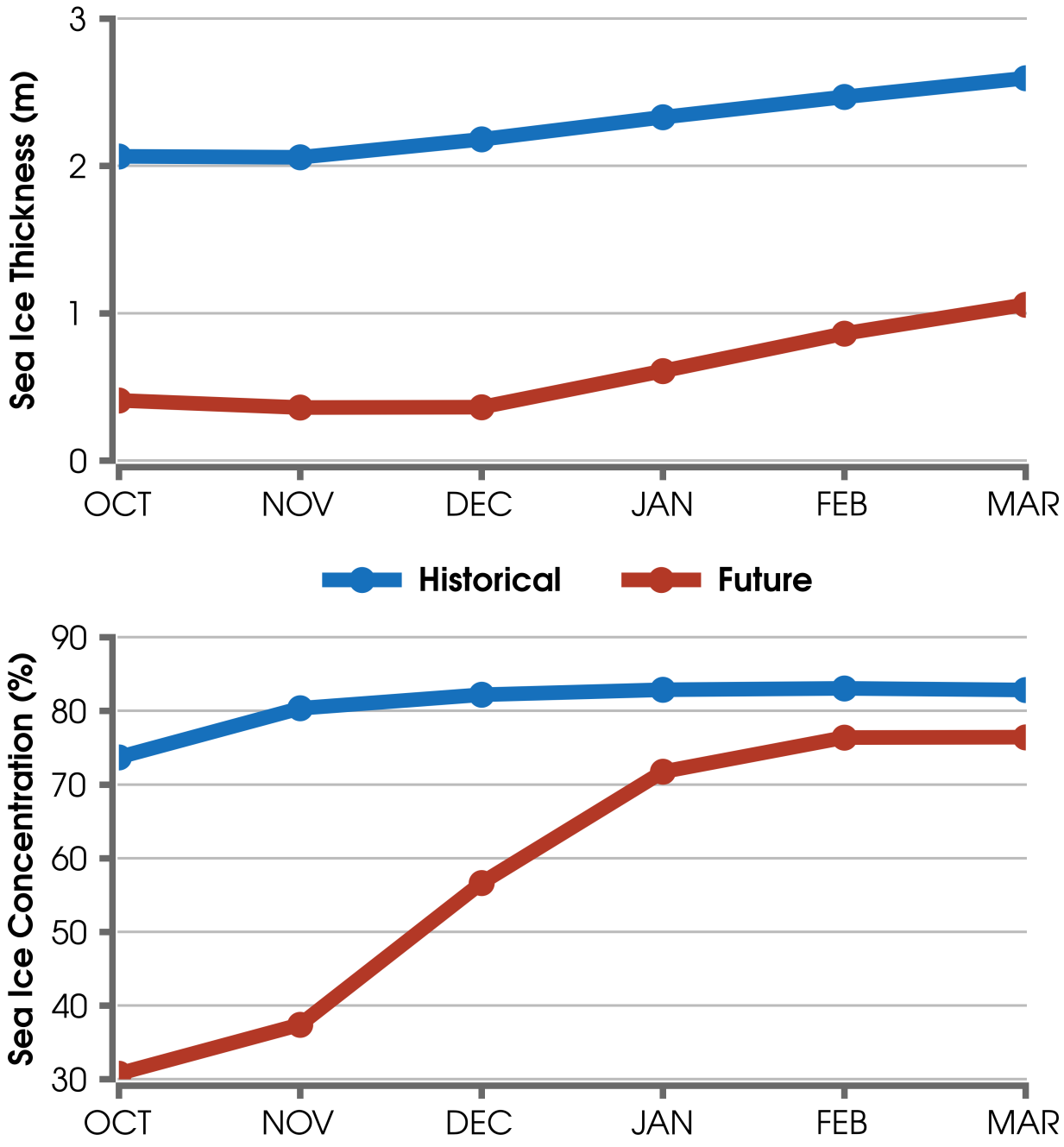

Figure A.7: Seasonal cycles of sea ice thickness (SIT; top) and sea ice concentration (SIC; bottom) over the historical (1976-2005; blue lines) and future (2051-2080; red lines) periods. Monthly sea ice values are an area-weighted average over the Arctic Ocean (north of 65°N) for grid cells with SIT greater than 0.15 m and SIC greater than 15%.

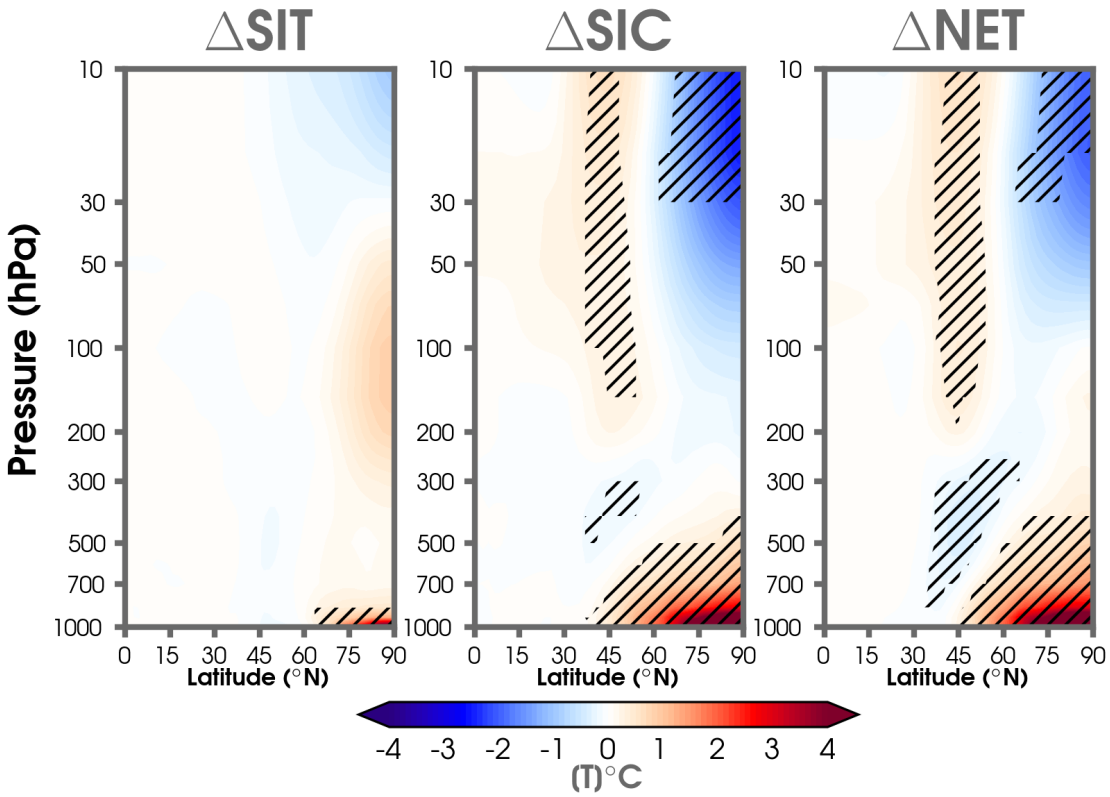

Figure A.8: DJF zonal-mean air temperature (T; °C) responses from future sea ice thickness loss (ΔSIT; FIT minus HIT), future sea ice concentration loss (ΔSIC; FIC minus HIC), and the net future sea ice effect (ΔNET; FICT minus HIT). Statistically significant responses at the 95% confidence level are shown by the black hatching.

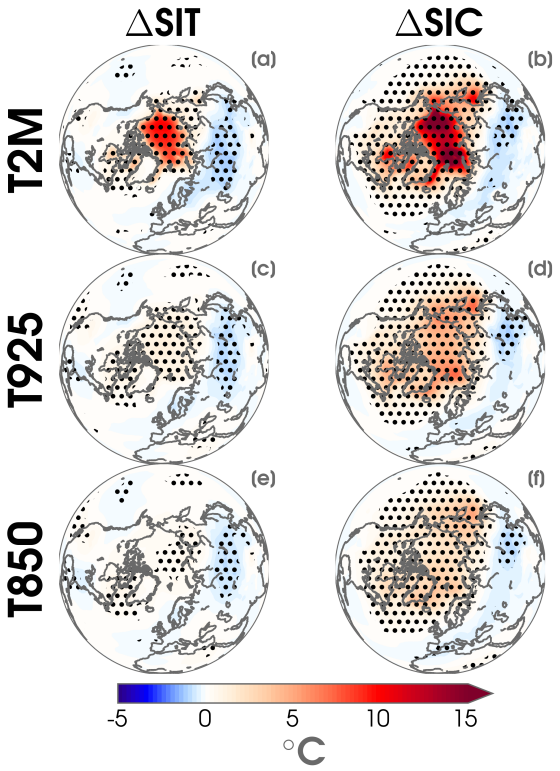

Figure A.9: Mean winter (DJF) air temperature responses (°C) are shown at 2-m (a,b; T2M), 925-hPa (c,d; T925) and 850-hPa (e,f; T850) from future sea ice thickness (ΔSIT) and future sea ice concentration (ΔSIC). Statistical significance at the 95% confidence level is identified by the black stippling. Note the difference in color scaling between positive and negative values.

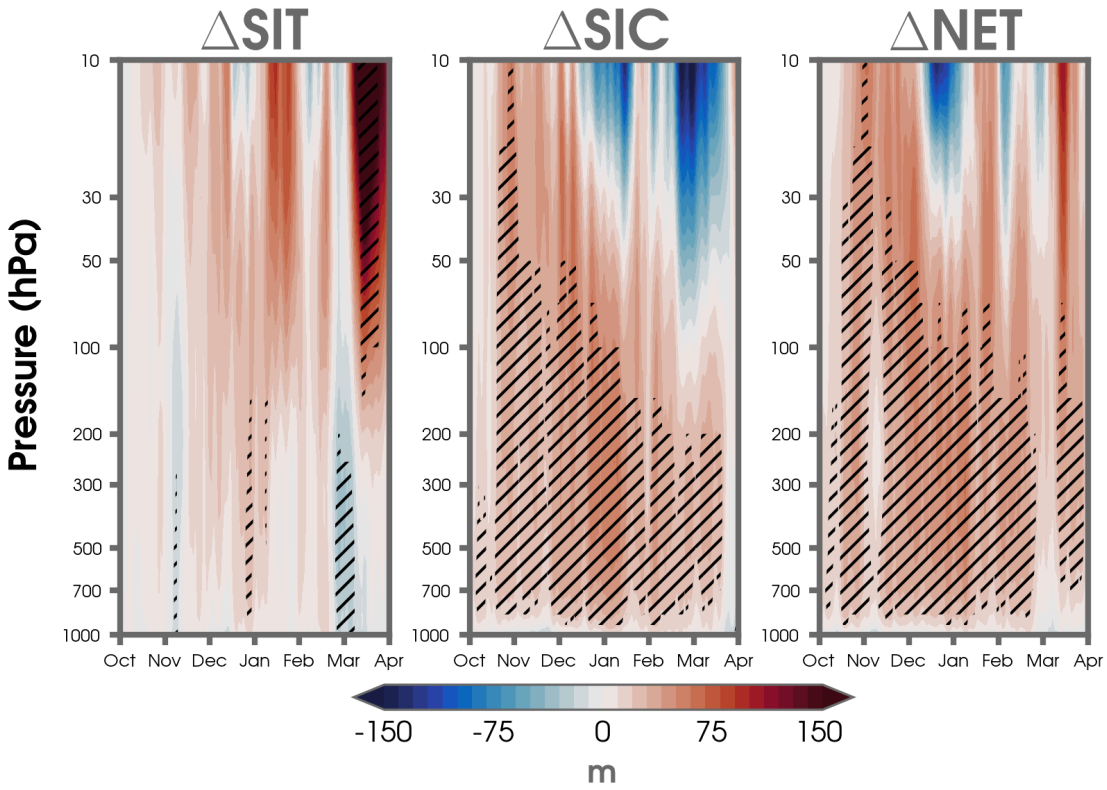

Figure A.10: Daily polar cap (>65°N) geopotential height responses as a function of height (pressure) from future sea ice thickness loss (ΔSIT; FIT minus HIT), future sea ice concentration loss (ΔSIC; FIC minus HIC), and the net future sea ice effect (ΔNET; FICT minus HIT). Anomalies are shown from October 1 through March 31. Statistically significant responses at the 95% confidence level are shown by the black hatching.

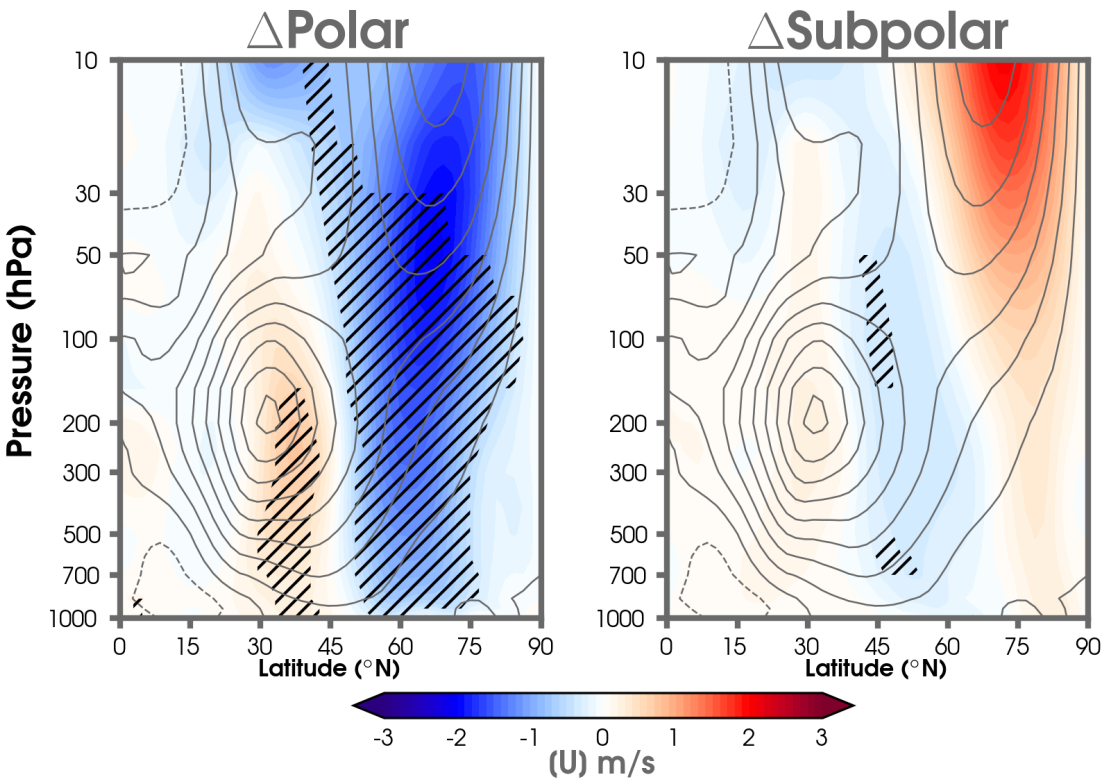

Figure A.11: DJF zonal-mean zonal wind (U; m s^{-1}) responses comparing the effect of polar (>66.6°N) sea ice anomalies (ΔPolar; FPOL minus HIC; colored shading) and the effect of subpolar (<66.6°N) sea ice anomalies (ΔSubpolar; FSUB minus HIC; colored shading). Climatological zonal-mean zonal wind from HIC is overlaid by the grey contours (interval of 5 m s^{-1}). Statistically significant responses at the 95% confidence level are shown by the black hatching.

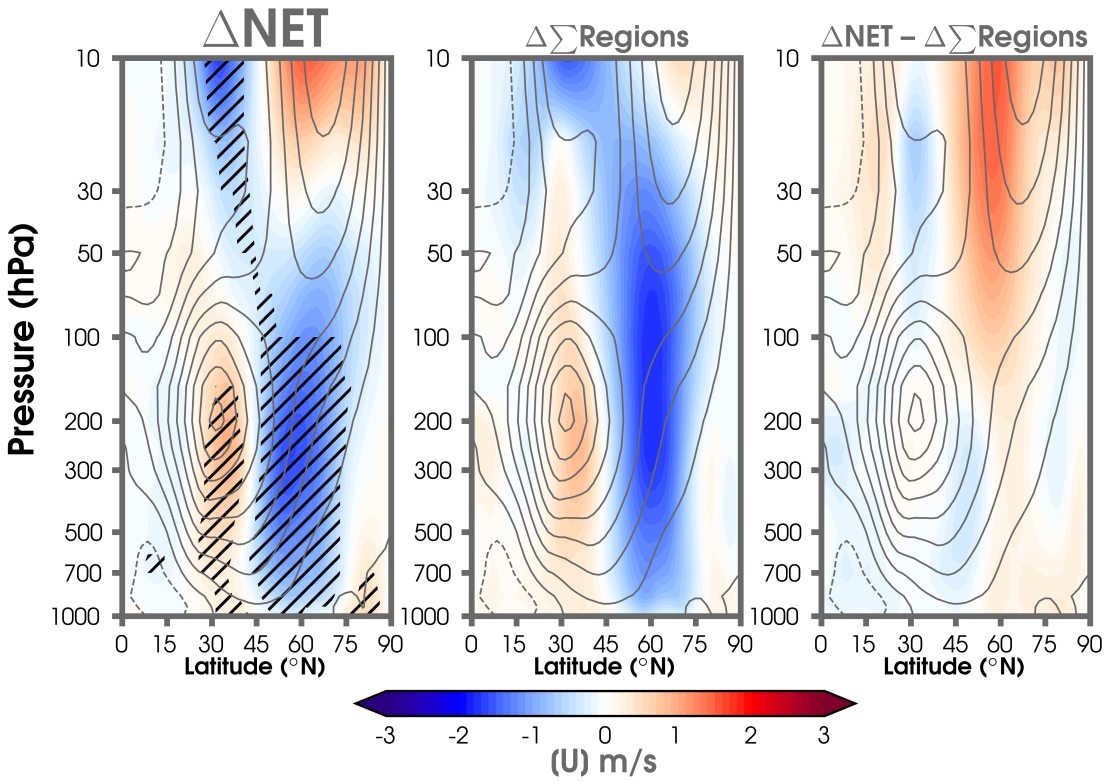

Figure A.12: DJF zonal-mean zonal wind (U; m s^{-1}) responses are shown for the net future sea ice effect (ΔNET; FICT minus HIT; left), sum of the regional responses (Δ ∑Regions; ΔPolar plus ΔSubpolar; middle), and ΔNET minus the sum of the regional responses (ΔNET minus Δ ∑Regions; right). Climatological zonal-mean zonal wind from HIC is overlaid by the grey contours (interval of 5 m s^{-1}). Statistically significant responses at the 95% confidence level are shown by the black hatching for ΔNET.

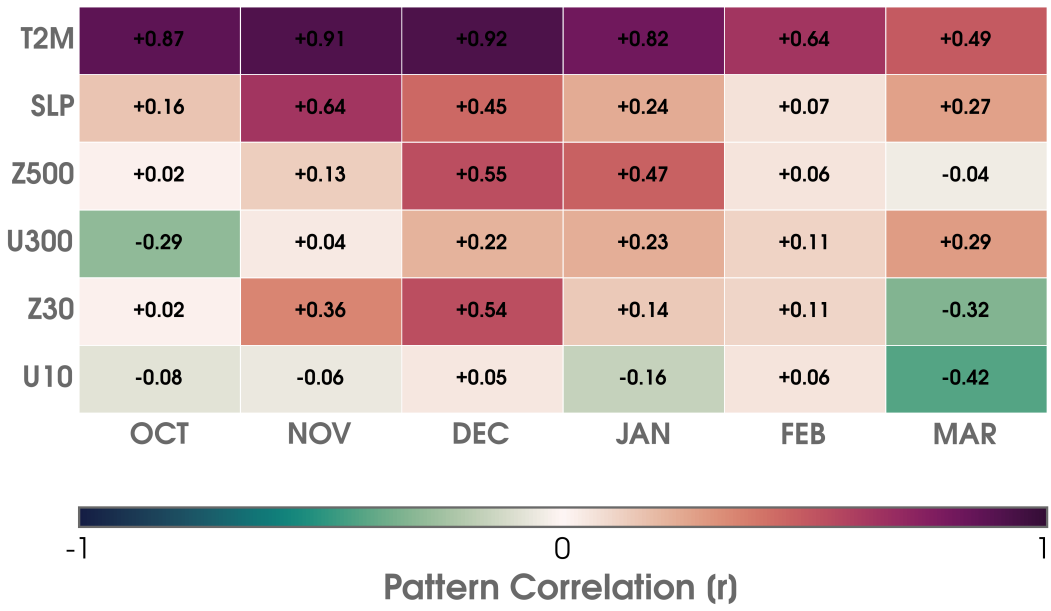

Figure A.13: Monthly pattern (Pearson's r) correlations compare the response of ΔSIT with ΔSIC (averaged north of 40°N, for areas of at least 95% significance level only).

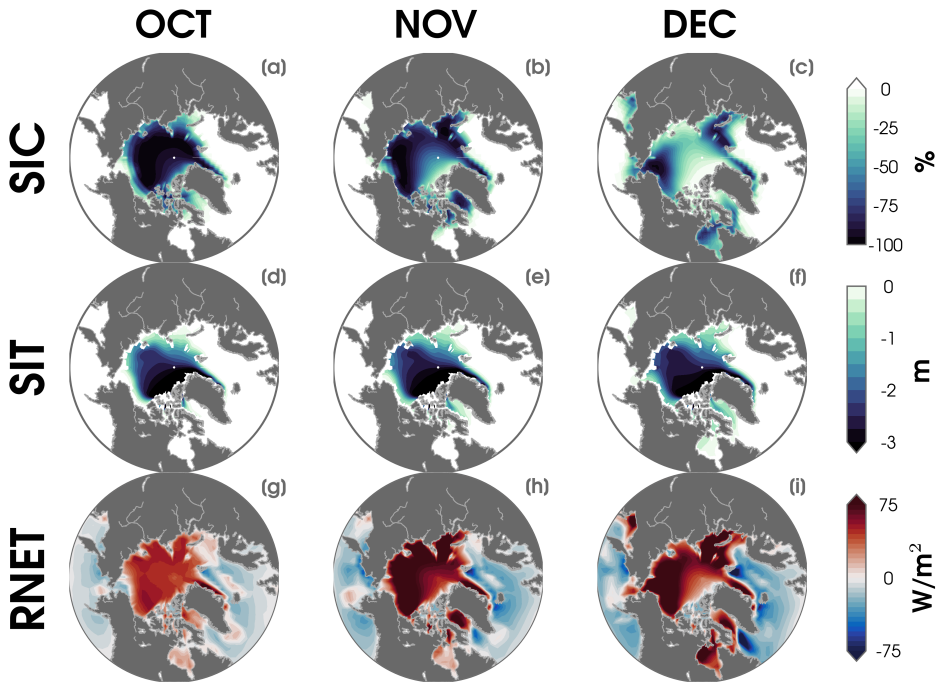

Figure A.14: Monthly sea-ice concentration (SIC; a-c) and sea-ice thickness (SIT; d-f) anomalies prescribed in the future simulation during early winter. The anomalies (a-f) are calculated from the difference of the 2051-2080 (future) minus 1976-2005 (historical) sea-ice conditions using the mean of 40 ensembles from LENS. The response of the net surface energy flux (RNET; turbulent plus net longwave) is also shown in October (g), November (h) and December (i). Upward fluxes are defined positive (W m^{-2}).

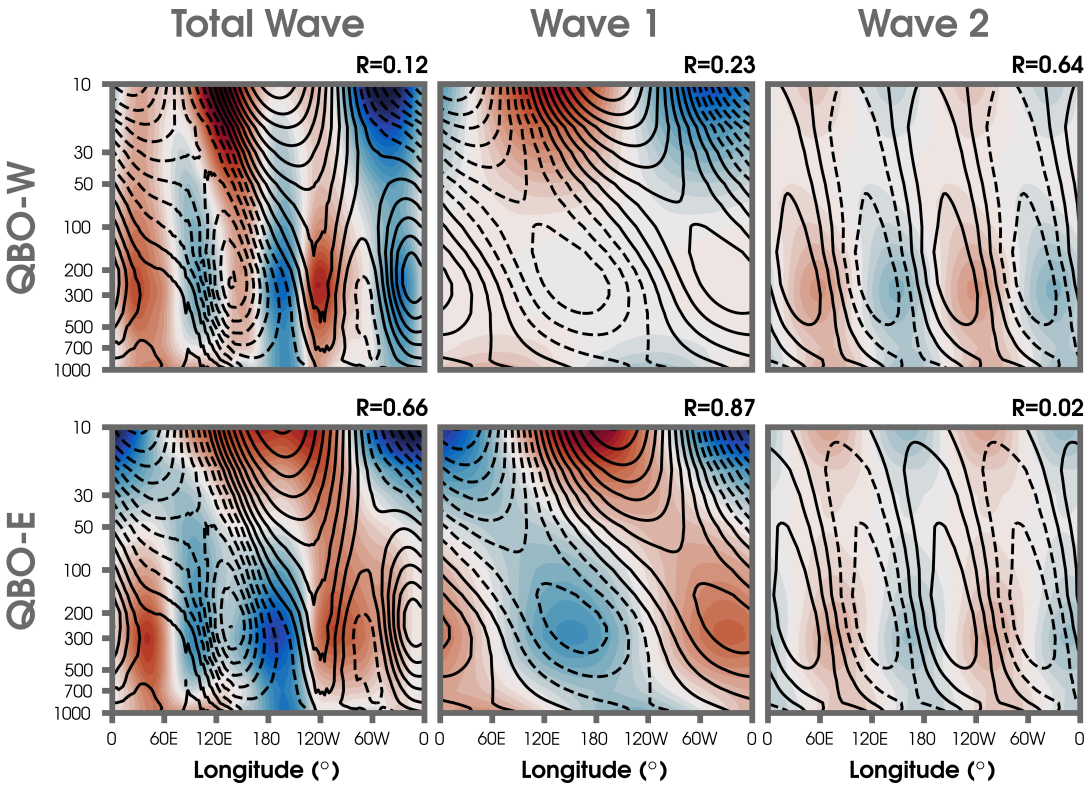

Figure A.15: Vertical profiles (longitude-pressure) of the climatological (contours) and forced (shading) stationary waves at 50°N in November to December and then composited by QBO phase (Top; Future-QBO-W minus Historical-QBO-W, and Bottom; Future-QBO-E minus Historical-QBO-E). The stationary waves are decomposed into the total wave (left), zonal wave number 1 (middle), zonal wave number 2 (right) components. The response (shading) is displayed at an interval of 2 m. The climatological waves (contours) are calculated from the historical experiment and shown at intervals of 25 m for the total wave and zonal wave number 1 and intervals of 5 m for zonal wave number 2. The pressure-weighted spatial correlations (R) between the climatological and forced waves are displayed in the upper right-hand corner of each subplot.

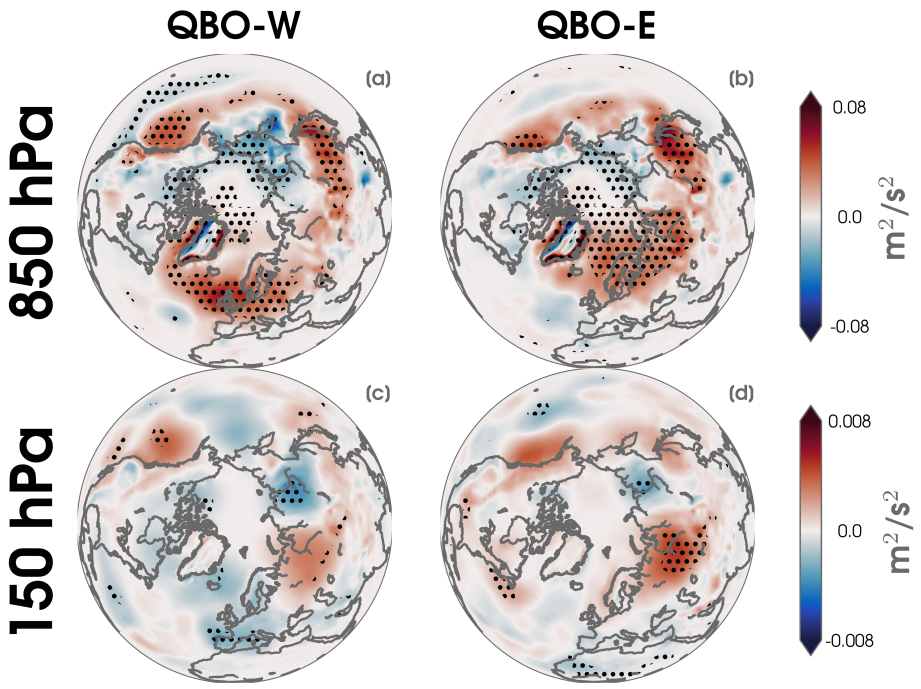

Figure A.16: Average November to December WAFz anomalies for QBO-W (left) and QBO-E (right) at 850 hPa (a-b) and 150 hPa (c-d). Black stippling indicates statistically significant responses at the 95% confidence level.

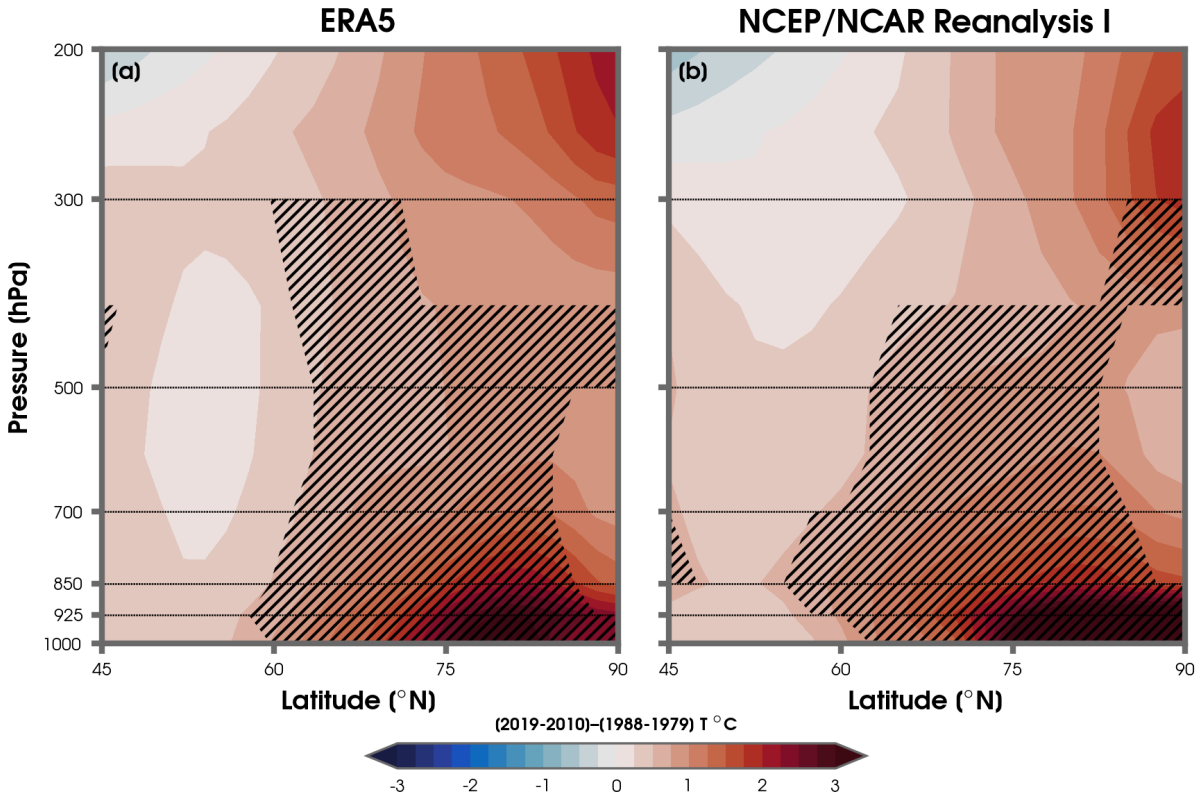

Figure A.17: Vertical cross section of the difference in average December-February zonal-mean air temperature (T) as a function of height (pressure) in (a) ERA5 and (b) NCEP/NCAR RI. Differences are calculated from 2019-2010 minus 1988-1979 (contour interval of 0.25°C). Black hatch marks indicate statistical significance at the 95% confidence level after controlling for the FDR.

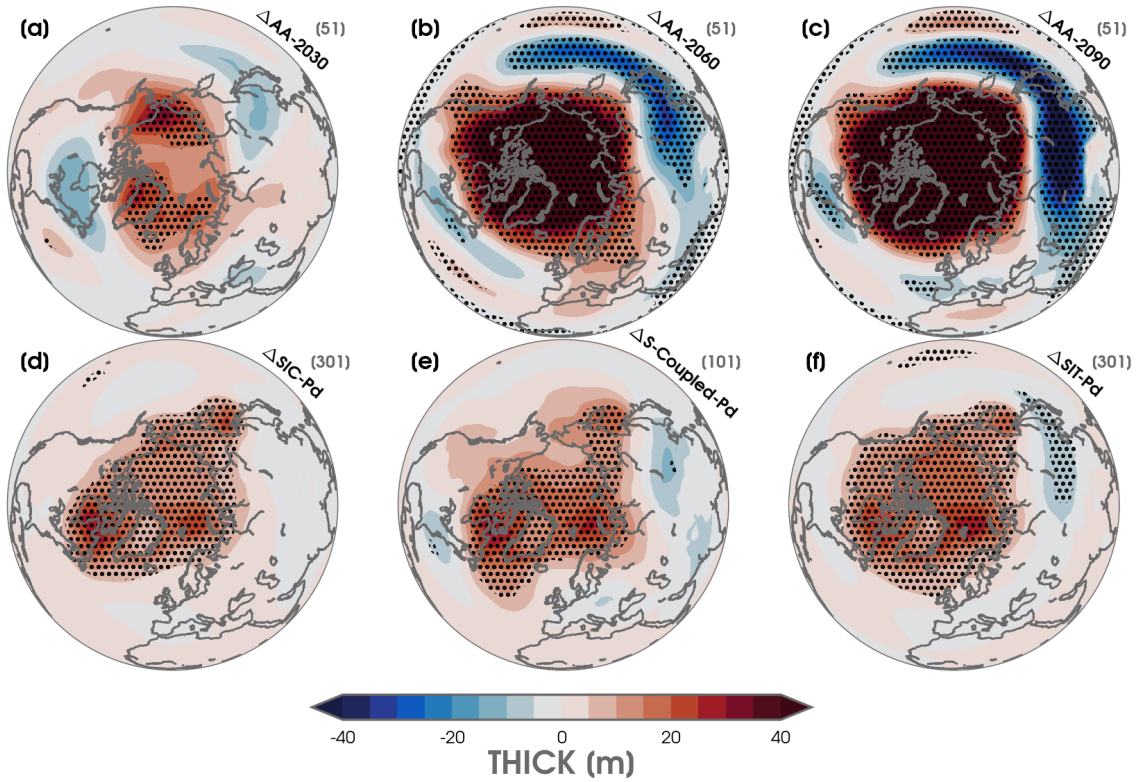

Figure A.18: (a) Average December-February 1000-500 hPa thickness layer response (THICK; interval of 5 m) for ΔAA-2030. (b) Same as (a) but for ΔAA-2060. (c) Same as (a) but for ΔAA-2090. (d) Same as (a) but for ΔSIC-Pd. (e) Same as (a) but for ΔS-Coupled-Pd. (f) Same as (a) but for ΔSIT-Pd. Areas of statistically significant anomalies are shown by black stippling after considering the FDR at the 95% confidence level. The number of ensemble members for each experiment is listed in the upper right-hand corner in gray.

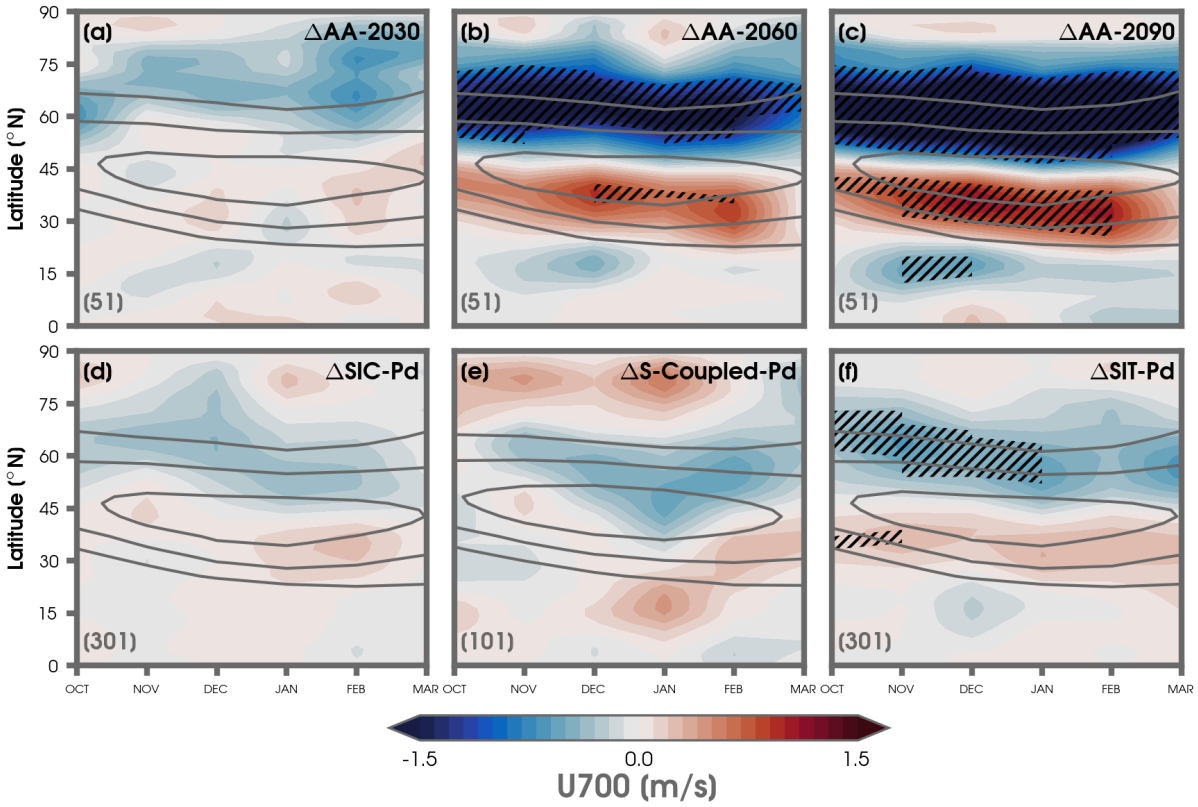

Figure A.19: (a) October to March anomalies of the 700-hPa zonal wind (U700) shown in shading (interval of 0.1 m/s) for ΔAA-2030. The gray contour lines illustrate the climatological zonal wind (3 m/s interval from 3 m/s). (b) Same as (a) but for ΔAA-2060. (c) Same as (a) but for ΔAA-2090. (d) Same as (a) but for ΔSIC-Pd. (e) Same as (a) but for ΔS-Coupled-Pd. (f) Same as (a) but for ΔSIT-Pd. Statistically significant anomalies are indicated with black hatch marks based on a FDR at the 95% confidence level. The number of ensemble members for each experiment is listed in the bottom left-hand corner.

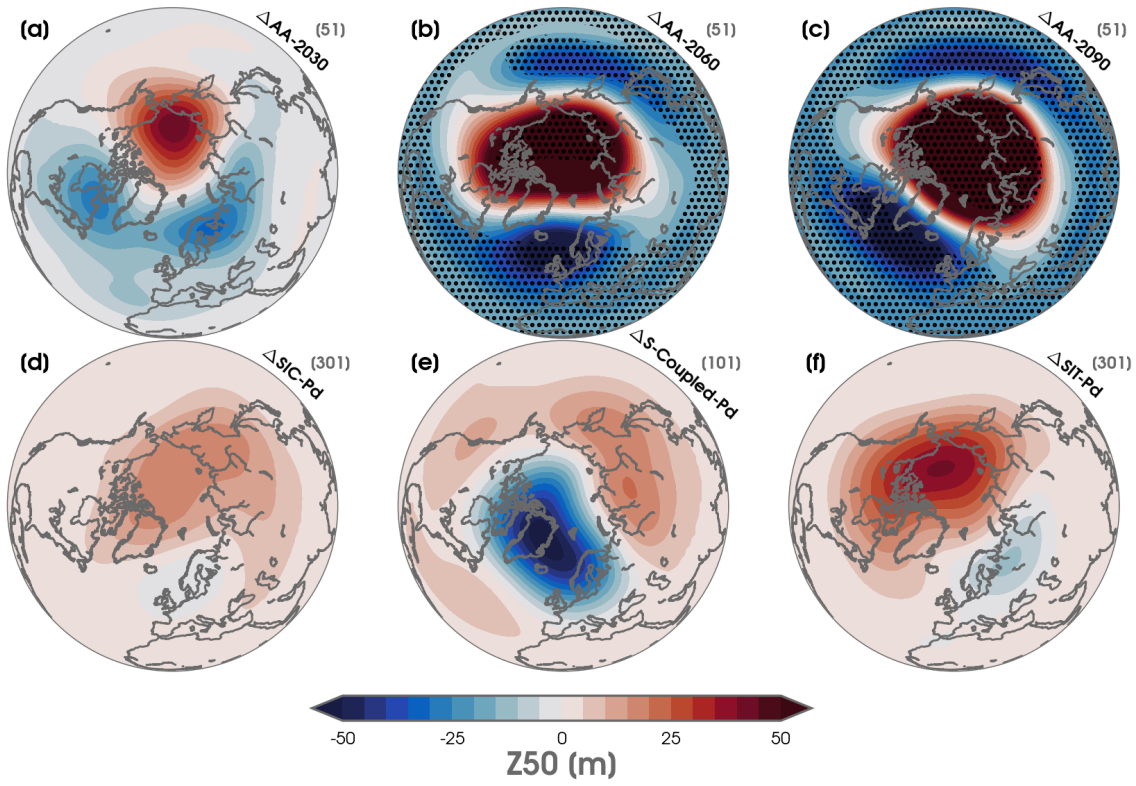

Figure A.20: Same as Figure A18, but for the geopotential height response at 50-hPa (Z50; interval of 5 m) in each experiment.